FACULDADE DE ENGENHARIA DA UNIVERSIDADE DO PORTO

Finite Element Analysis of Hybrid Composite Shields

Inês Couto Moura



Master in Mechanical Engineering

Supervisor: Prof. Marco Parente

Co-Supervisor: Prof. Volnei Tita

September, 2026

© Inês Moura, 2026

Finite Element Analysis of Hybrid Composite Shields

Inês Couto Moura

Master in Mechanical Engineering

September, 2026

"Innovation begins with curiosity."

Nikola Tesla

Acknowledgements

I would like to express my profound gratitude to Professor Marco Parente for his invaluable assistance in the simulation process. The development of this thesis was significantly facilitated by the availability of the researcher, his technical expertise, and the computational resources he provided. I would also like to express my profound gratitude to Professor Dr. Volnei Tita for his unwavering guidance, insightful feedback, and steadfast support throughout the course of my research.

To my family, I am immensely grateful. I would like to express my sincere gratitude to my parents and my brother for their boundless love, unwavering patience, and constant encouragement. Your consistent support throughout this endeavour has served as the cornerstone that has enabled me to persevere, and this achievement is as much attributable to you as it is to me.

In addition, I would like to express my gratitude to my friends. It is important to express gratitude for the camaraderie, stimulating discussions and encouragement received during the present journey. It is submitted that these factors have not only rendered the journey enjoyable, but have also assisted in overcoming difficult moments.

This thesis is the result of the contributions and assistance of the aforementioned individuals, for which I am truly grateful. Their participation in this chapter of my life has been instrumental.

Abstract

The utilisation of composite materials in the domains of civil and military aviation is predominantly attributable to their elevated specific stiffness and strength. In military applications, the necessity to protect aircraft without compromising operational performance is the driving force behind the investigation of alternatives to conventional metallic armour. Additionally, protection via light body armours also constitutes a recent relevant research topic. Hybrid laminates combining metallic layers and polymer composites offer a means of exploiting complementary material properties, although their design requires an understanding of the damage and failure mechanisms that develop under high-velocity loading.

The present dissertation develops and evaluates a three-dimensional finite element modelling approach in Abaqus/Explicit to investigate normal ballistic impact on hybrid laminates. The reference configuration consists of two 2024-T3 aluminium face sheets and a carbon-fibre-reinforced polymer laminate, which is subjected to impact by rigid projectiles with flat, hemispherical and sharp nose geometries. The behaviour of aluminium is described using the Johnson-Cook plasticity and damage models. The composite intralaminar failure model is represented by a three- dimensional Hashin formulation implemented in a Vectorized User Material subroutine (VUMAT), incorporating progressive stiffness degradation, strain-rate effects and element deletion. The concept of interlaminar damage is delineated through the utilisation of cohesive interface formulations.

The methodology encompasses the independent calibration of metallic and composite material models, utilising experimental results to ensure accuracy and precision. The hybrid model is then subjected to a rigorous evaluation, whereby it is assessed against a range of published experimental data. This evaluation involves the analysis of initial-residual velocity relationships, ballistic-limit estimates and post-impact morphologies. As a constituent element of the modelling procedure, mesh refinement, boundary conditions and contact definitions are subjected to rigorous scrutiny. In order to investigate the failure mechanisms associated with the different projectile geometries, damage-related state variables are also considered.

A parametric study examines the influence of aluminium alloy, composite material, geometric aspects and ply orientation on the ballistic response. Projectile residual velocity is the principal comparison metric, with structural mass and damage development also being considered. The overall aim of this research is to establish a numerical methodology to support the selection of materials and the design of hybrid laminates for use in the protection of military aircraft and personal armour.

Keywords: Hybrid laminates, Ballistic impact, Aluminium, CFRP, UHMWPE, Hashin failure, Cohesive zone model, J-C

Resumo

A utilização de materiais compósitos nos domínios da aviação civil e militar deve-se, principalmente, à sua elevada rigidez e resistência específicas. Nas aplicações militares, a necessidade de proteger as aeronaves sem comprometer o desempenho operacional é a força motriz por trás da investigação de alternativas à blindagem metálica convencional. Além disso, a proteção por meio de coletes leves à prova de bala constitui também um tema de investigação relevante e recente. Os laminados híbridos que combinam camadas metálicas e compósitos poliméricos oferecem uma forma de tirar partido das propriedades complementares dos materiais, embora a sua conceção exija uma compreensão dos mecanismos de dano e de rotura que se desenvolvem sob cargas de alta velocidade.

A presente dissertação desenvolve e avalia uma abordagem de modelação tridimensional por elementos finitos no Abaqus/Explicit para investigar o impacto balístico normal em laminados híbridos. A configuração de referência consiste em duas chapas de alumínio 2024-T3 e um laminado de polímero reforçado com fibra de carbono, que é submetido ao impacto de projéteis rígidos com geometrias de extremidade plana, hemisférica e cónica. O comportamento do alumínio é descrito utilizando os modelos de plasticidade e danos de Johnson-Cook. O modelo de falha intralaminar do compósito é representado por uma formulação tridimensional de Hashin implementada numa subrotina VUMAT, incorporando a degradação progressiva da rigidez, efeitos da taxa de deformação e eliminação de elementos. O dano interlaminar é simulado através da utilização de uma formulação baseada no conceito de interface coesiva.

A metodologia inclui a calibração independente dos modelos do material metálico e do compósito, recorrendo a resultados experimentais. O modelo híbrido é então submetido a uma avaliação rigorosa, na qual é comparado com um conjunto de dados experimentais publicados na literatura. Esta avaliação envolve a análise das relações entre velocidade inicial e residual, estimativas do limite balístico e morfologias pós-impacto. Como elemento constitutivo do procedimento de modelação, o refinamento da malha, as condições de fronteira e as definições de contacto são submetidos a um escrutínio rigoroso. A fim de investigar os mecanismos de rotura associados às diferentes geometrias dos projéteis simulados, são também consideradas variáveis de estado relacionadas com os diversos tipos de dano.

Posteriormente, foi realizado um estudo paramétrico para examinar a influência de diversoso parâmetros, tais como, o tipo de liga de alumínio, o tipo de material compósito, a geometria da placa híbrida e dos projetéis e a orientação das camadas na resposta balística. A velocidade residual do projétil é o principal parâmetro de comparação, sendo também consideradas a massa estrutural e a evolução dos danos. O objetivo geral desta investigação é estabelecer uma metodologia numérica para suportar a seleção de materiais e a conceção de laminados híbridos destinados à proteção de aeronaves militares e de equipamento de proteção individual.

Palavras-chave: Laminados híbridos, Impacto balístico, Alumínio, Compósito de fibra de carbono e epóxido, Polietileno de alto peso molecular, Critério de falha de Hashin, Modelo de zona coesiva, J-C

The UN Sustainable Development Goals

The present dissertation is aligned with several United Nations Sustainable Development Goals (SDGs), with innovations in sustainable materials, efficient structural design, and enhanced protection technologies. The selected goals have been derived directly from the official UN SDG descriptions in order to ensure fidelity to their original framing [1]. The following list details the Sustainable Development Goals that have been identified as being most pertinent to this research:

- **SDG 9** - Industry, Innovation and Infrastructure: Build resilient infrastructure, promote inclusive and sustainable industrialization and foster innovation.
- **SDG 12** - Responsible Consumption and Production: Ensure sustainable consumption and production patterns.
- **SDG 13** - Climate Action: Take urgent action to combat climate change and its impacts.
- **SDG 16** - Peace, Justice and Strong Institutions: Promote peaceful and inclusive societies for sustainable development, provide access to justice for all and build effective, accountable and inclusive institutions at all levels.

Table 1: Relevant UN Sustainable Development Goals for this dissertation [1].

SDG	Goal	Relevance to this dissertation
9	Industry, innovation and infrastructure	This research contributes to the advancement of resilient and sustainable infrastructure through the development of innovative composite structures that integrate lightweight material design innovations to support efficient aerospace and defence systems.
12	Responsible consumption and production	The employment of advanced composites in an efficient manner, coupled with the optimisation of material usage, serves to promote environmentally responsible production, curtail waste, and foster circularity in advanced structural design.
13	Climate action	Creating lightweight, durable structural elements can help reduce system energy demands, decarbonise transportation and defence and mitigate climate impact.
16	Peace, justice and strong institutions	The integration of advanced ballistic and protective technologies supports security and peacekeeping efforts, thereby indirectly contributing to the promotion of societal stability and the creation of safe environments.

Contents

1 Introduction **1**
1.1 Contextualization and Objectives . . . 1
1.2 Methodology . . . 2
1.3 Dissertation Structure . . . 3

2 Literature Review **5**
2.1 Composite Materials . . . 5
2.1.1 Matrices . . . 6
2.1.1.1 Polymeric Matrices . . . 6
2.1.1.2 Ceramic Matrices . . . 7
2.1.1.3 Metal Matrices . . . 8
2.1.2 Reinforcements . . . 9
2.1.2.1 Carbon Fibres . . . 9
2.1.2.2 Glass Fibres . . . 10
2.1.2.3 Organic Fibres . . . 11
2.1.3 Hybrid Composite Laminates . . . 12
2.1.4 Composites in Aeronautical Engineering . . . 13
2.2 Military Aircraft Certification . . . 15
2.2.1 European Military Certification Network . . . 16
2.2.2 United States Military Certification Network . . . 18
2.2.3 Ballistic Testing Standards used by the US Military: The Case of MIL-STD-662F . . . 21
2.3 Ballistic Protections . . . 22
2.3.1 Hybrid Laminates for Ballistic Applications . . . 23
2.3.2 Ballistic Protection Development and Pratical Examples . . . 24
2.4 Impact Velocity Regime . . . 25
2.5 Dynamic Explicit Finite Element Modelling . . . 27
2.5.1 Element Size Requirements for Resolving Stress Waves . . . 30

3 Failure Models Theoretical Description **33**
3.1 Hashin Failure Criterion . . . 33
3.1.1 Hashin Criterion - Damage Evolution Law . . . 35
3.2 Strain Rate Effect on Polymer Matrix Composites . . . 40
3.3 Johnson-Cook Model . . . 41
3.4 Interlaminar Failure Model . . . 43
3.4.1 Interlaminar Failure Model - Damage Evolution Law . . . 44
3.5 Numerical Implementation of Failure Criteria . . . 46
3.6 Previous Work Developed at FEUP . . . 47

4 Case Study on High-Velocity Ballistic Impacts **49**
4.1 Experimental Setup . . . 50
4.2 Model Construction and Setup . . . 51
4.2.1 Part Definition and Model Geometry . . . 51
4.2.1.1 Target Plate . . . 51
4.2.1.2 In-Plane Partitioning . . . 52
4.2.1.3 Projectiles . . . 53
4.2.2 Material Definition and Section Assignment . . . 53
4.2.2.1 Aluminium Layers . . . 54
4.2.2.2 Composite Region . . . 54
4.2.2.3 Projectiles . . . 57
4.2.3 Assembly . . . 57
4.2.4 Step Definition . . . 58
4.2.5 Cohesive Zone Analysis and Contact Interaction . . . 60
4.2.6 Boundary and Initial Conditions . . . 62
4.2.7 Mesh Definition . . . 63
4.2.7.1 Mesh Size Selection for Stress Wave Resolution . . . 64
4.3 Boundary Condition Sensitivity . . . 65
4.4 Aluminium and Composite Models Calibration . . . 66
4.5 Results and Discussion . . . 68
4.5.1 Influence of Projectile Geometry on Composite Damage . . . 72
4.5.1.1 Fibre Tensile and Compressive Damage . . . 77
4.5.1.2 Matrix Tensile and Compressive Damage . . . 79
4.5.1.3 Strain-Rate Amplification Factors . . . 80
4.5.2 Influence of Projectile Geometry on Aluminium Damage . . . 81
4.5.3 Energy Balance . . . 83
4.5.3.1 Global Energy Contributions and Balance . . . 83
4.5.3.2 Kinetic Energy Evolution . . . 87
4.5.3.3 Internal Energy Evolution . . . 87

5 Parametric Study **89**
5.1 Influence of Material Selection . . . 89
5.1.1 Aluminium Alloy . . . 89
5.1.2 Composite Material . . . 91
5.2 Influence of Geometrical Parameters . . . 94
5.2.1 Target Plate Diameter . . . 94
5.2.2 Projectile Diameter . . . 95
5.2.3 Aluminium and Composite Layers Thickness . . . 96
5.3 Influence of Ply Orientation . . . 98
5.4 Proposed Hybrid Configuration . . . 100

6 Conclusions **103**
6.1 Future Work . . . 104

References **107**

Appendix A VUMAT Subroutine **117**

List of Figures

2.1 Schematic representation of the matrix, reinforcement and interphase of a composite material [15]. . . . 6
2.2 Examples of laminates configurations: (a) Unidirectional, (b) Cross-ply, (c) Angle-ply and (d) Quasi-isotropic [39]. . . . 12
2.3 Evolution of composites in the aeronautical industry [4]. . . . 14
2.4 Schematic representation of the projectile impact outcomes: (A) Partial penetration and (B) Complete penetration [9]. . . . 22
2.5 Ballistic protection for aircraft and helicopters [68]. . . . 24
2.6 (a) A-10C Thunderbolt II ("Warthog"), (b) Titanium "Bathtub" [6]. . . . 25
2.7 Example function $f(t)$. . . . 28

3.1 Damage parameter d evolution as a function of the equivalent displacement $\delta_{i,\text{eq}}$. 36
3.2 Linear elastic and linear softening regime (Adapted from [83]). . . . 38
3.3 Fracture crack separation modes [89]. . . . 43
3.4 The bilinear traction-separation law in cohesive zone model for the coesive elements (Adapted from [83]). . . . 44

4.1 Ballistic impact experimental setup [99]. . . . 50
4.2 Aluminium and composite parts. . . . 52
4.3 Geometric parameters of (a) flat, (b) hemispherical and (c) sharp projectiles [100]. Specimens dimensions are in mm. . . . 53
4.4 Projectiles analytical rigid parts. . . . 53
4.5 Mechanical constants input in Abaqus/Computer-Aided Engineering (CAE). . . . 55
4.6 Complete assembly of the target and the hemispherical projectile. . . . 58
4.7 Mass scaling definitions in Abaqus/CAE. . . . 59
4.8 Contact property assignments for the projectile, aluminium and CFRP interfaces. 60
4.9 Definition of the *comp-comp* contact property in Abaqus/CAE. . . . 61
4.10 Boundary conditions applied to the target and projectile in Abaqus/CAE. . . . 62
4.11 Local mesh refinement along the impact axis. . . . 63
4.12 Final mesh configuration of the full model. . . . 65
4.13 Velocity-time history for aluminium and composite calibration models. . . . 67
4.14 Comparison of numerical and experimental [99] initial-residual velocity curves for different projectile geometries. . . . 69
4.15 Comparison between the experimental post-impact morphologies (left) and the corresponding numerical predictions (right) (Adapted from [99]). . . . 71
4.16 SDVs of the composite for the flat projectile impact. . . . 73
4.17 SDVs of the composite for the hemispherical projectile impact. . . . 74
4.18 SDVs of the composite for the sharp projectile impact. . . . 75

4.19 Comparison of fibre and matrix damage indexes for the different projectile geometries. . . . 77
4.20 PEEQ of the aluminium for different projectiles geometries. . . . 81
4.21 Energy contributions for the flat projectile. . . . 84
4.22 Energy contributions for the hemispherical projectile. . . . 84
4.23 Energy contributions for the sharp projectile. . . . 85
4.24 Global kinetic energy for the three projectile geometries at an initial velocity of 100 m/s. . . . 86
4.25 Internal energy excluding artificial strain energy for the three projectile geometries at an initial velocity of 100 m/s. . . . 86

5.1 Initial-residual velocity curve for 7075-T6/UHMWPE configuration. . . . 102

List of Tables

1 Relevant UN Sustainable Development Goals for this dissertation [1]. ix

2.1 MIL-STD-662F description [59] 21

3.1 Calibrated maximum strain rate scaling factors (Adapted from [84]). 41
3.2 Access to material models 47

4.1 Properties of 2024-T3 aluminium alloy [100, 101]. 54
4.2 Composite material properties (CFRP) [99, 100]. 55
4.3 Material parameters of the cohesive elements for CFRP interfaces [99, 102]. . . . 56
4.4 Material parameters of the cohesive elements for the aluminium-CFRP bonded joint [100]. 57
4.5 Residual velocity obtained using the different boundary condition definitions. . . 66
4.6 Aluminium and composite calibration results. 67
4.7 Experimental and numerical results for the ballistic limits of CARALL2/1. 70

5.1 Material properties and J-C parameters of the different aluminium alloys [107–110]. 90
5.2 Residual velocity response of the different aluminium alloys. 90
5.3 Material properties of the UD composite systems [111–116]. 92
5.4 Material properties of the woven composite systems [114, 117, 118]. 92
5.5 Interlaminar properties of the cohesive interfaces [64, 112, 115, 117, 119–122]. . 93
5.6 Residual velocity response of the composite systems. 93
5.7 Residual velocity response for the different target plate diameters. 95
5.8 Residual velocity response for the different projectile diameters. 96
5.9 Layer-thickness configurations and corresponding residual-velocity response. . . 97
5.10 Residual velocity response for the different composite stacking sequences. 99
5.11 AWD of the investigated hybrid configurations. 101

List of Acronyms

2D	two-dimensional
3D	three-dimensional
AFLCMC	Air Force Life Cycle Management Center
ARALL	Aramid-Reinforced Aluminium Laminate
ARMS	Aviation Resource Management Survey
AWD	Areal Weight Density
CAE	Computer-Aided Engineering
CARALL	Carbon Reinforced Aluminium Laminate
CFRP	Carbon Fiber Reinforced Polymers
DOA	Design Organisation
DoD	Department of Defense
EASA	European Union Aviation Safety Agency
EDA	European Defence Agency
EMADs	European Military Airworthiness Documents
EMARs	European Military Airworthiness Requirements
EMDOA	European Military Design Organisation Approval
EU	European Union
FAA	Federal Aviation Administration
FEM	Finite Element Method
FRP	Fibre-Reinforced Polymer
GLARE	Glass Reinforced Aluminium Laminate
GUI	Graphical User Interface
J-C	Johnson-Cook
MAA	Military Aviation Authority
MAWA	Military Airworthiness Authorities
MFTP	Military Flight Test Permit
MTC	Military Type Certificate
NAMP	Naval Aviation Maintenance Program
NAVAIR	Naval Air Systems Command
PAN	Polyacrylonitrile

PEEK	polyether ether ketone
PEKK	polyether ketone ketone
PEEQ	Equivalent Plastic Strain
PPS	polyphenylene sulfide
RTS	Release to Service
SDVs	State-Dependent Variables
TAA	Technical Airworthiness Authority
UD	unidirectional
UHMWPE	Ultra-High Molecular Weight Polyethylene
US	United States
USAF	United States Air Force
VUMAT	Vectorized User Material subroutine

List of Symbols

Symbol	Description	Units
α	Power-law fracture energy exponent; shear weighting factor in Hashin's criterion	–
β	Cohesive mode mixity ratio; strain rate amplification factor	–
$\beta_{\max}$	Maximum strain rate amplification factor	–
a	Lambert-Jonas fitting coefficient	–
A	Johnson-Cook initial yield stress	MPa
B	Johnson-Cook strain strengthening coefficient	MPa
$\mathbf{C}$	Damping matrix	N·s/m
C	Johnson-Cook strain rate sensitivity	–
$\mathbf{C}_0$	Undamaged stiffness tensor	MPa
$\mathbf{C}_\mathrm{d}$	Damaged stiffness tensor	MPa
$C_{11}, \ldots, C_{66}$	Stiffness matrix components	MPa
c_d	Dilatational wave speed	m/s
d	Scalar damage variable	–
d_i	Damage variable for failure mode i	–
$d_\mathrm{ft}, d_\mathrm{fc}$	Fibre tensile and compressive damage	–
$d_\mathrm{mt}, d_\mathrm{mc}$	Matrix tensile and compressive damage	–
$d_\mathrm{f}, d_\mathrm{m}$	Fibre and matrix stiffness retention factors	–
d_s	Shear damage variable	–
D	Stiffness normalisation factor; accumulated Johnson-Cook damage	–
$D_1, \ldots, D_5$	Johnson-Cook failure parameters	–
δ_0	Displacement at the onset of softening	mm
δ_1', δ_2'	First and second shear separation components	mm
δ_3	Normal separation component	mm
δ_eff	Effective interface displacement	mm
δ_eff^0	Effective displacement at damage onset	mm
$\delta_\mathrm{eff}^\mathrm{f}$	Effective displacement at complete failure	mm

Symbol	Description	Units
$\delta_{\text{eff}}^{\max}$	Maximum effective displacement over the loading history	mm
δ_{f}	Final displacement in the softening law	mm
δ_{eq}	Equivalent intralaminar displacement	mm
$\delta_{i,\text{eq}}$	Equivalent displacement for failure mode i	mm
$\delta_{i,\text{eq}}^{0}$	Equivalent displacement at damage onset for mode i	mm
$\delta_{i,\text{eq}}^{\text{f}}$	Equivalent displacement at complete failure for mode i	mm
$\delta_{\text{n}}, \delta_{\text{s}}, \delta_{\text{t}}$	Normal and tangential interface separations	mm
δ_{shear}	Combined shear separation	mm
$\delta_{\text{shear}}^{\text{f}}$	Shear separation at complete failure	mm
$\delta_{\text{m}}^{0}, \delta_{\text{m}}^{\text{f}}$	Mixed-mode separations at damage onset and complete failure	mm
$\delta_{1}^{\text{f}}, \delta_{2}^{\text{f}}, \delta_{3}^{\text{f}}$	Separation components at complete failure	mm
Δd	Projectile displacement between camera frames	m
Δt	Time increment	s
Δt_{stable}	Maximum stable time increment	s
Δv_{r}	Relative change in residual velocity	%
E	Young's modulus	GPa
E_1	Young's modulus in the fibre direction	GPa
E_2	Young's modulus in the transverse direction	GPa
$\boldsymbol{\varepsilon}$	Strain tensor	–
$\varepsilon_{11}, \varepsilon_{22}, \varepsilon_{33}$	Normal strain components	–
$\varepsilon_{12}, \varepsilon_{13}, \varepsilon_{23}$	Shear strain components	–
ε_{xy}	Generic strain component	–
$\bar{\varepsilon}^{\text{p}}$	Equivalent plastic strain	–
$\Delta\bar{\varepsilon}^{\text{p}}$	Equivalent plastic strain increment	–
ε_{f}	Plastic failure strain	–
$\dot{\varepsilon}$	Strain rate	s^{-1}
$\dot{\bar{\varepsilon}}^{\text{p}}$	Equivalent plastic strain rate	s^{-1}
$\dot{\varepsilon}_0, \dot{\bar{\varepsilon}}_0$	Reference strain rate	s^{-1}
η	Benzeggagh–Kenane interaction exponent	–
f	External force vector	N
$f_i^{\text{ext}}, f_i^{\text{int}}$	External and internal forces	N
$f_{\max}$	Maximum frequency of interest	Hz
F_i	Hashin failure index for mode i	–
$F_{\text{ft}}, F_{\text{fc}}$	Fibre tensile and compressive failure indices	–
$F_{\text{mt}}, F_{\text{mc}}$	Matrix tensile and compressive failure indices	–
G_{12}	Shear modulus in the 1-2 plane	GPa

Symbol	Description	Units
G_{23}	Shear modulus in the 2-3 plane	GPa
G_{c}	Critical fracture energy	N/mm
G_{ic}	Fracture energy for failure mode i	N/mm
$G_{\mathrm{ft}}, G_{\mathrm{fc}}$	Tensile and compressive fracture energies in the fibre direction	N/mm
$G_{\mathrm{mt}}, G_{\mathrm{mc}}$	Tensile and compressive fracture energies normal to the fibre direction	N/mm
$G_{\mathrm{I}}, G_{\mathrm{II}}, G_{\mathrm{III}}$	Energy release rates for Modes I, II and III	N/mm
$G_{\mathrm{I}}^{\mathrm{c}}, G_{\mathrm{II}}^{\mathrm{c}}, G_{\mathrm{III}}^{\mathrm{c}}$	Critical fracture energies for Modes I, II and III	N/mm
G_{T}	Total energy release rate	N/mm
G_{shear}	Combined shear energy release rate	N/mm
$\mathbf{K}$	Global stiffness matrix	N/m
K	Effective cohesive penalty stiffness	MPa/mm
$K_{\mathrm{n}}, K_{\mathrm{s}}, K_{\mathrm{t}}$	Normal and tangential cohesive stiffnesses	MPa/mm
L, L_{e}	Characteristic element length	mm
l_{c}	Characteristic length for damage regularisation	mm
$\hat{\lambda}, \hat{\mu}$	Lamé elastic parameters	Pa
λ_{min}	Minimum wavelength	mm
$\mathbf{M}$	Mass matrix	kg
m	Johnson-Cook temperature softening coefficient	–
μ	Friction coefficient	–
n	Johnson-Cook strain strengthening index; elements per wavelength	–
ν	Poisson's ratio	–
ν_{12}	Poisson's ratio in the 1-2 plane	–
ν_{23}	Poisson's ratio in the 2-3 plane	–
p	Lambert-Jonas fitting exponent	–
ρ	Material density	kg/m^3
ρ_{Al}	Aluminium density	kg/m^3
ρ_{comp}	Composite density	kg/m^3
ρ_{eff}	Effective hybrid target density	kg/m^3
S_{12}	Shear strength in the 1-2 plane	MPa
S_{13}	Shear strength in the 1-3 plane	MPa
S_{23}	Shear strength in the 2-3 plane	MPa
$S_{\mathrm{mt}}, S_{\mathrm{mc}}$	Matrix stiffness-degradation coefficients	–
σ	Stress tensor	MPa
$\sigma_{11}, \sigma_{22}, \sigma_{33}$	Normal stress components	MPa
$\sigma_{12}, \sigma_{13}, \sigma_{23}$	Shear stress components	MPa
σ_{eq}	Equivalent stress	MPa

Symbol	Description	Units
$\sigma_{i,\mathrm{eq}}$	Equivalent stress for failure mode i	MPa
$\sigma^0_{i,\mathrm{eq}}$	Stress at damage onset for mode i	MPa
σ_y	Johnson-Cook flow stress	MPa
σ_D	Stress after damage degradation	MPa
σ^*	Stress triaxiality	–
t	Time	s
t_Al	Total aluminium thickness	mm
t_comp	Total composite thickness	mm
t_total	Total target thickness	mm
$t_\mathrm{n}, t_\mathrm{s}, t_\mathrm{t}$	Normal and tangential cohesive tractions	MPa
$t_\mathrm{n}^\mathrm{max}, t_\mathrm{s}^\mathrm{max}, t_\mathrm{t}^\mathrm{max}$	Cohesive strengths at damage initiation	MPa
T	Temperature	K
T_r	Room temperature	K
T_m	Melting temperature	K
T^*	Homologous temperature	–
T^0_eff	Effective cohesive traction at damage onset	MPa
u	Displacement vector	m
$\dot{u}$	Velocity vector	m/s
$\ddot{u}$	Acceleration vector	m/s^2
v	Projectile velocity	m/s
v_i	Initial projectile velocity	m/s
v_r	Residual projectile velocity	m/s
v_bl	Ballistic-limit velocity	m/s
$v_\mathrm{bl,exp}$	Experimental ballistic-limit velocity	m/s
$X_\mathrm{T}, X_\mathrm{C}$	Longitudinal tensile and compressive strengths	MPa
ξ	Damping parameter	–
$Y_\mathrm{T}, Y_\mathrm{C}$	Transverse tensile and compressive strengths	MPa
ω_max	Maximum natural angular frequency	rad/s

Chapter 1

Introduction

1.1 Contextualization and Objectives

Composite materials are renowned for their elevated strength and specific stiffness. In the field of aeronautical industry, the substitution of metals with these materials has been instrumental in the development of lighter aircraft [2]. The introduction of this type of material has been gradual, primarily due to the actions of the certifying bodies. Given the fact that composite structures exhibit a distinct behavioural profile in comparison to conventional materials such as aluminium or steel, certifying agencies have expressed concerns. Consequently, these agencies are allocating greater resources to ensure that composite structures maintain equivalent levels of safety. Nevertheless, it is evident that components such as wings, empennage, fuselage and fan blades are now frequently manufactured using composite materials. Consequently, there have been a number of notable developments, including a reduction in fuel consumption, an increase in load capacity, and a marked improvement in aerodynamic performance. At present, a significant proportion of the structural weight of wide-body aircraft from the two primary civil aircraft manufacturers, Boeing and Airbus, such as the B787 and A350, is composed of composite materials. This proportion is estimated to be approximately 50 per cent [2–4].

The utilisation of composite materials in military aviation was initiated at an earlier date, a development that coincided with the implementation of more lenient certification procedures. Whilst the safety demonstrated by the aircraft is important, its performance constitutes the primary objective, with emphasis placed on aspects such as weapon load capacity, maximum speed, manoeuvrability and operational flexibility [5]. In the domain of aviation, composite materials have emerged as a viable solution for the ballistic protection of aircraft. The utilisation of materials such as steel or titanium for ballistic protection in aircraft has been employed in aircraft such as the A-10C Thunderbolt II. However, the high density of these metals only permits localised protection, thereby avoiding a substantial increase in the aircraft's weight and a concomitant reduction in performance [6].

The advent of composite materials and the subsequent research conducted on their performance in ballistic impacts has rendered the implementation of ballistic protection in military

aircraft a viable prospect, with minimal impact on operational capabilities. Nevertheless, it is imperative to acknowledge the suboptimal performance characteristics inherent in these materials. In pursuit of this objective, a range of studies have been conducted with a view to the creation of hybrid structures/plates, for instance by combining ceramic, metallic and composite materials. The objective of the present study is to overcome the individual deficiencies of each constituent [7, 8].

In addition to experimental studies and testing, the development of this type of laminate is also performed by computational numerical methods, such as the finite element method. The employment of material models that accurately describe the behaviour of the different components has enabled the exploration of various combinations of hybrid laminates, thus obviating the high costs typically associated with physical experiments [9]. In this sense, the primary motivation underpinning this dissertation is the investigation of material models for the development of a hybrid laminate plate for the protection of military aircraft. The design of a structure of this type can be divided into three distinct phases. Firstly, there is the conceptual design phase. Secondly, there is the preliminary design phase. Thirdly, there is the detailed design phase. As this dissertation constitutes the inaugural investigation of the problem, it is situated within the conceptual phase.

The principal aim of this study is to evaluate material models and approaches that have the capacity to simulate hybrid laminates when subjected to ballistic or high-velocity impacts. In order to achieve this objective, it is necessary to employ dynamic explicit analyses in conjunction with three-dimensional (3D) models that take into account the strain rate effect.

1.2 Methodology

The research is founded upon a simulation-driven strategy that is entirely predicated on 3D explicit dynamics. The reference configuration consists of a hybrid target composed of two aluminium top and bottom faces and a composite in the middle. The aluminium layers are described using a high strain rate ductile constitutive model appropriate for impact loading, namely the Johnson-Cook (J-C) formulation as implemented in Abaqus/Explicit. The composite is defined through a ply-by-ply approach, whereby orthotropic elasticity is combined with mode-specific failure criteria. These criteria are implemented in a user-defined material subroutine called VUMAT, which is based on the 3D Hashin formulation. The strain rate dependence is incorporated into the composite response to facilitate the capture of the strength enhancement that has been observed under ballistic loading conditions. It is imperative to note that all components, including the projectile, the aluminium plates and the laminate plies, are modelled with three-dimensional solid elements. Furthermore, interactions are governed by general contact.

The ballistic limit velocity is determined by the application of impacts at various velocities. The comparison is focused on projectile residual velocity, the time history of absorbed energy, and the spatial distribution of damage in the backing. In order to ensure a fair assessment, all other modelling choices, including element formulation, mesh, contact settings, time step control and requested outputs, are kept identical across cases.

1.3 Dissertation Structure

The structure of the document is presented below. The chapters are arranged in accordance with the sequence of development of the project, thereby underscoring a progressive approach to the problem.

The first chapter provides a comprehensive overview of the context and motivation for the utilisation of composite materials in the field of military aviation ballistic protection. It delineates the objectives of the study, while also offering a concise summary of the modelling methodology employed and the document's structure.

Chapter 2 comprises a literature review, which establishes the theoretical foundation for the dissertation. The text commences with a comprehensive overview of composite materials and laminated structures in the context of aerospace applications. This is followed by a detailed exposition of the certification framework for military aircraft and the stringent requirements for ballistic protection systems. This chapter also provides a review of the development of hybrid armour concepts. It concludes with an introduction to numerical modelling approaches, focusing on explicit dynamic simulations for impact problems.

Chapter 3 provides a comprehensive overview of the constitutive models and failure criteria that were employed in the numerical simulations. The text provides a comprehensive explanation of the 3D Hashin formulation employed in the analysis of intralaminar failure within composite plies. It also elucidates the implementation of this formulation in a user-defined VUMAT subroutine, along with the associated property degradation laws. The interlaminar modelling and the J-C model for metals are also addressed. These considerations provide the theoretical framework required for the subsequent case studies.

Chapter 4 provides a comprehensive overview of the finite element model setup in Abaqus/Explicit. It also presents the experimental and numerical results of high-velocity impact tests conducted on the aluminium/CFRP target. These results include projectile kinematics, absorbed energy histories, and damage fields.

In Chapter 5, a parametric study is conducted for the purpose of evaluating the influence of various parameters on the performance of the hybrid laminate. The corresponding ballistic simulations are presented, and the outcomes are compared with the hybrid composite baseline. This is done in order to assess potential advantages and optimised solutions.

Chapter 6 provides a synopsis of the primary findings in relation to the specified objectives, while concurrently delineating recommendations for subsequent development. These recommendations encompass the refinement of models and the validation of experimental results.

Chapter 2

Literature Review

2.1 Composite Materials

Composite materials are constituted by combining two or more distinct constituents that remain identifiable within the resulting material system. In contrast to alloys or solid solutions, composites are characterised by the retention of discrete phases and clearly defined interfaces. The collective behaviour of these systems at the macroscopic level is contingent on the inherent properties, geometric configuration, relative orientation, and spatial distribution of constituent elements, in addition to the interplay between these elements. This combination facilitates the development of materials characterised by elevated specific strength and stiffness, augmented fatigue and corrosion resistance, and mechanical or thermal properties customised to specific applications [10–12].

Despite the recent advancements in the systematic development of advanced composites, the underlying concept can be traced back to both natural structures and early engineered materials. For instance, the bone is the combination of a collagen-rich organic phase with mineral constituents results in a balanced state of rigidity, strength, and resistance to fracture [13]. In a similar manner, the utilisation of discontinuous reinforcing phases, such as straw-reinforced clay, has been demonstrated to enhance the mechanical performance of a brittle matrix. This approach is a historical construction material technique [14].

At the constituent level, a composite comprises a continuous matrix, a reinforcing phase and the interphase between them. The reinforcement, which may take the form of fibres, particles, whiskers or flakes, generally provides the principal contribution to stiffness and strength. The interphase is pivotal in regulating the transfer of load between the matrix and the reinforcement, thereby significantly impacting the initiation of damage and the integrity of the structure [12, 15]. These components are represented schematically in Figure 2.1.

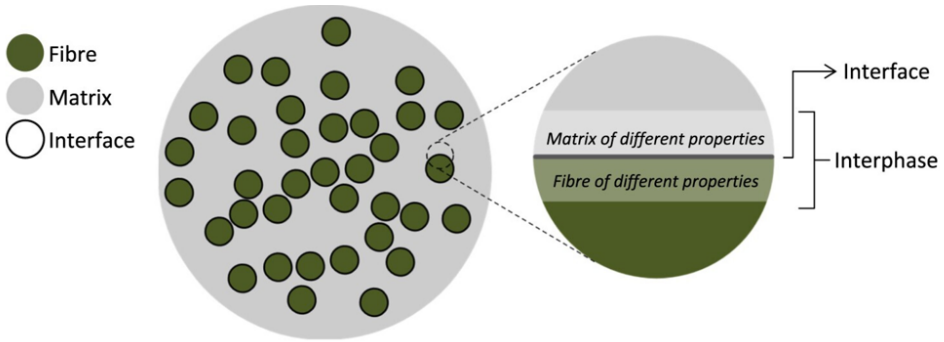


Figure 2.1: Schematic representation of the matrix, reinforcement and interphase of a composite material [15].

The utilisation of composite materials has seen a marked increase in sectors where structural efficiency and weight reduction are of critical importance, most notably in the aerospace, automotive, marine and defence industries. The performance of these structures can be adapted through the selection of constituent materials, reinforcement architecture and manufacturing process. The following subsections examine the principal matrix systems and reinforcement fibres, providing the basis required to understand the mechanical behaviour and failure mechanisms of the composite structures considered in this work.

2.1.1 Matrices

The matrix phase functions as the continuous monolithic medium into which the high-strength reinforcement phase is securely embedded. The fundamental structural integrity, environmental resilience, maximum operating temperature, and interlaminar shear strength of the final composite material are entirely contingent upon the precise chemical and physical nature of the chosen matrix. The matrix must effectively bond the discrete reinforcing elements together, rigidly maintaining their designated geometric orientation, while simultaneously distributing and transferring external mechanical stresses uniformly across the dispersed phase. Furthermore, the matrix acts as a critical protective barrier, shielding the highly sensitive reinforcing fibres from catastrophic environmental damage, including rapid high-temperature oxidation, corrosive chemical attack, and physical abrasion during operational service. Evidently, matrices can be categorised into four primary classes in accordance with their fundamental atomic bonding and molecular architecture. The constituent materials under consideration are polymeric, ceramic, metal and carbon [10, 16, 17].

2.1.1.1 Polymeric Matrices

Polymer Matrix Composites (PMCs) represent the most widely used class of structural composites. They combine low density with high specific mechanical properties, exhibit corrosion resistance and provide considerable manufacturing flexibility. The widespread application of the technology is further supported by two factors. Firstly, comparatively low processing temperatures are

utilised. Secondly, manufacturing methods suitable for components with complex geometries are available [10, 16, 18].

Polymeric matrices are commonly classified as thermosetting or thermoplastic. Thermosetting resins undergo an irreversible cross-linking reaction during the curing process, forming a rigid 3D molecular network that is not capable of subsequent remelting or reshaping. The materials in question have been shown to offer enhanced fibre adhesion, dimensional stability, and chemical resistance, in addition to relatively high stiffness. However, their limited strain to failure and irreversible curing process can impose constraints on their damage tolerance and recyclability. Epoxy resins represent the most prevalent thermosetting matrices in high-performance composites. Other examples include polyesters, vinyl esters, phenolics, bismaleimides, cyanate esters and polyimides [19].

Thermoplastic matrices are constituted primarily of linear or branched polymer chains and soften when heated, allowing them to be repeatedly formed and consolidated. This reversible behaviour enables shorter processing cycles, post-forming operations, repair and improved recyclability. In addition, thermoplastics generally exhibit higher strain to failure, greater impact resistance, good thermal stability and lower moisture sensitivity in comparison to thermosetting polymers. However, the comparatively high processing temperatures and melt viscosities of these materials may impede fibre impregnation and increase manufacturing requirements. A number of high-performance thermoplastic matrices are considered to be commonplace, including polyether ether ketone (PEEK), polyphenylene sulfide (PPS) and polyether ketone ketone (PEKK) [16, 20].

Despite their advantages, PMCs remain limited by the temperature-dependent behaviour of the polymer matrix and by their susceptibility to long-term environmental effects. Elevated temperatures can reduce matrix stiffness and load-transfer efficiency, while moisture absorption may plasticise the polymer and lower its glass-transition temperature. Matrix selection must therefore consider not only mechanical performance and manufacturability, but also the thermal and environmental conditions expected throughout the service life of the composite structure [17].

2.1.1.2 Ceramic Matrices

Ceramic matrices are distinguished by their strong ionic and covalent bonds, which confer several advantageous properties, including high stiffness, hardness, chemical resistance and thermal stability. These properties render them suitable for operation in corrosive environments and at temperatures beyond the practical range of polymeric matrices. However, monolithic ceramics exhibit limited plastic deformation and low fracture toughness, rendering them susceptible to rapid crack propagation and sudden brittle failure under tensile loading or thermal shock [21].

The development of Ceramic Matrix Composites (CMCs) is primarily driven by the necessity to enhance the damage tolerance of monolithic ceramics, while maintaining their inherent thermal and chemical resistance. Continuous fibres, whiskers or particles are incorporated into the ceramic matrix to introduce energy-dissipation mechanisms such as crack deflection, crack bridging and reinforcement pull-out. It has been demonstrated that these mechanisms serve to reduce stress

concentration at the crack tip, thereby promoting progressive damage and, in turn, increasing fracture toughness and resistance to thermal and mechanical shock [22].

Ceramic matrices are typically categorised into two distinct systems: oxide and non-oxide. Common oxide matrices include aluminium oxide (Al_2O_3), zirconium oxide (ZrO_2) and mullite (Al_2O_3–SiO_2), which provide high resistance to oxidation and chemical degradation. Non-oxide matrices include silicon carbide (SiC), silicon nitride (Si_3N_4), and aluminium nitride (AlN). These materials characteristically exhibit elevated levels of stiffness and advantageous thermal-transport properties. Nevertheless, environmental protection may be necessary when exposed to oxidising atmospheres at elevated temperatures [16, 21].

The selection of a ceramic matrix is contingent upon the requisite operating temperature, the magnitude of mechanical loading, thermal conductivity, and environmental resistance. It is imperative to pay particular attention to the compatibility between the matrix and the reinforcement, with particular emphasis on their coefficients of thermal expansion. Significant mismatch has been shown to generate residual stresses and matrix microcracking during processing or thermal cycling, thereby reducing the strength and durability of the composite [17].

2.1.1.3 Metal Matrices

Metal Matrix Composites (MMCs) are a class of material that combine a continuous metallic phase with fibres, whiskers or particles. The purpose of this combination is to improve the performance of conventional metal alloys. In comparison with polymeric matrices, metals offer superior service temperatures, transverse strength, thermal and electrical conductivity, and resistance to compressive loading. The incorporation of a reinforcing phase has been demonstrated to engender a marked enhancement in specific stiffness, strength, wear resistance and creep resistance, whilst concomitantly effecting a reduction in thermal expansion [21, 23].

Aluminium, magnesium and titanium alloys are among the most frequently used matrices because they offer favourable combinations of density and mechanical performance. Furthermore, nickel- and cobalt-based superalloys may be utilised in instances where resistance to elevated temperatures is imperative. The most common reinforcements include silicon carbide (SiC), aluminium oxide (Al_2O_3), boron carbide (B_4C) and carbon fibres. The resulting composites find application in a variety of settings, including aerospace, automotive and tribological contexts, where the requirements for high stiffness, dimensional stability and wear resistance are particularly stringent [16, 23].

The manufacture of MMCs is more complex than that of polymer-matrix systems because metals generally require higher processing temperatures and pressures. These conditions can promote undesirable chemical reactions, poor wetting or residual stresses at the matrix-reinforcement interface. Differences in thermal expansion between the constituents may also generate internal stresses during cooling and thermal cycling. Consequently, the quality and stability of the interface are critical to load transfer and the long-term integrity of the composite [16, 17].

2.1.2 Reinforcements

The reinforcement is the dispersed phase responsible for carrying a substantial proportion of the applied load and for increasing the stiffness, strength, fatigue resistance and damage tolerance of a composite material. The introduction of reinforcements may be effected by means of particles, flakes, whiskers, short or continuous fibres, and 2D or 3D fabrics. The form that is selected is contingent upon the requisite mechanical response, the manufacturing process, and the degree of directional control that is required [17, 24, 25].

Fibres represent the principal reinforcement employed in high-performance structural composites, a material choice that is predicated on the fact that their high length-to-diameter ratio enables efficient load transfer along the longitudinal direction. The reduced diameter of these fibres also serves to minimise the likelihood of critical internal defects, thereby enabling them to attain a greater tensile strength in comparison to the corresponding bulk material. Consequently, continuous fibres provide the highest performance when aligned with the principal loading direction. However, multidirectional or woven arrangements are required when loads act along several directions [23].

The final properties of a fibre-reinforced composite are contingent on the fibre material, length, orientation, distribution and adhesion to the matrix. The fibre volume fraction is also a fundamental design parameter, insofar as it determines the relative contribution of the reinforcement and matrix to the overall response. It is evident that an increase in reinforcement content typically results in enhanced stiffness and load-bearing capacity. However, it is imperative to note that values that are excessively high may impede impregnation processes and, consequently, lead to the formation of voids or interfacial defects [12].

In relation to the materials utilised in reinforcements, three primary categories are identified: carbon, glass and organic, which are predominantly combined with polymeric matrices.

2.1.2.1 Carbon Fibres

Carbon fibres are extensively utilised in lightweight structural composites due to their ability to combine low density with high specific tensile strength, high specific modulus, good fatigue resistance and a low coefficient of thermal expansion. Furthermore, the materials exhibit favourable thermal and electrical conductivity, in addition to excellent dimensional stability. The aforementioned characteristics lend support to the utilisation of the materials in question within the domains of aerospace, automotive and protective structures. The necessity to reduce weight must be achieved without compromising stiffness or load-bearing capacity is a key consideration in these fields [26].

The primary precursor of carbon fibres is polyacrylonitrile (PAN), although rayon and petroleum pitch may also be used as precursors. The manufacturing process of PAN-based fibres typically involves stabilisation in an oxidising atmosphere, followed by carbonisation at temperatures in excess of 1000 °C in an inert environment. These treatments are designed to remove non-carbon elements and progressively develop an oriented carbon structure along the fibre axis. It has been

demonstrated that additional heat treatment at elevated temperatures can enhance structural order and elastic modulus, resulting in fibres that are often characterised as graphitic or high-modulus carbon fibres [27, 28].

Following carbonisation, the fibre surface is typically subjected to a treatment that aims to enhance chemical activity and adhesion to the matrix. Subsequently, a sizing layer is applied to protect the fibres during handling and to promote compatibility with the selected resin. The effective interfacial bonding that is required for the transfer of load from the matrix to the reinforcement is of paramount importance, with the objective of avoiding both premature debonding and fibre damage [27].

The highly oriented structure of carbon fibres produces marked anisotropy, resulting in a high modulus along the layer plane, potentially reaching 1000 GPa, while the modulus along the c-axis (the direction perpendicular to the stacked carbon layers) remains comparatively lower, at approximately 35 GPa. The relatively low strain to failure of these materials results in brittle behaviour. It is therefore vital that composite laminates use appropriate fibre orientations and stacking sequences to withstand ultidirectional loading. Typical carbon fibres have micrometre-scale diameters and densities that are substantially lower than those of structural metals. However, it should be noted that the strength and modulus of carbon fibres can vary considerably depending on the precursor and the conditions of the heat treatment [17].

2.1.2.2 Glass Fibres

Glass fibres are the most widely used synthetic reinforcement in polymer composites because they provide high tensile strength, chemical resistance and electrical insulation at a comparatively low cost. They are produced from silica-rich mineral mixtures combined with metallic oxides, whose proportions determine the chemical composition and resulting properties. Their principal limitations include brittleness, relatively high density compared with carbon and organic fibres, and sensitivity to abrasion and surface defects [28].

The production process may be executed through an indirect marble-melting process or by direct melting. In the indirect method, raw materials are initially formed into glass marbles measuring between 15 and 20 mm in diameter. These marbles are subsequently re-melted and extruded into fibres. The direct-melt process eliminates the intermediate production and remelting of glass marbles, thereby reducing the number of processing stages [28].

The tensile strength of glass fibres is found to be significantly influenced by the condition of their surface. It has been demonstrated that physical stress, in the form of handling, abrasion and environmental exposure, has the capacity to induce microscopic defects, which, in turn, have been shown to result in a reduction in performance. A sizing treatment is thus administered immediately following fibre formation for the purpose of protecting the surface, facilitating processing and enhancing adhesion to the polymer matrix. The formulation of sizing is commonly accompanied by the incorporation of coupling agents, which are selected in accordance with the specific matrix material intended for use [17, 28].

In the realm of glass fibre composition, E-glass stands out as a prevailing formulation due to its optimal balance of mechanical performance, electrical insulation, and cost-effectiveness. S-glass provides greater tensile strength and improved fatigue and temperature resistance, but its higher cost limits its use to demanding aerospace, defence and high-performance structural applications. Other specialised formulations include alkali-resistant glass (AR-glass) and corrosion-resistant glass (ECR-glass), which are selected for chemically aggressive environments [17, 28].

2.1.2.3 Organic Fibres

Organic fibres encompass both synthetic polymeric fibres and lignocellulosic fibres that are naturally derived. The materials' generally low density provides favourable specific mechanical properties, rendering them attractive for lightweight structures. In high-performance and ballistic applications, the principal synthetic organic reinforcements are Aramid and Ultra-High Molecular Weight Polyethylene (UHMWPE), whereas natural fibres are used mainly when low cost, reduced environmental impact and moderate structural performance are prioritised [29].

Aramid fibres are aromatic polyamides that have been commercialised under various trade names, including Kevlar and Twaron. The molecular chains of these materials are characterised by a high degree of rigidity and orientation, which contributes to their exceptional tensile strength, toughness, thermal stability, and resistance to abrasion and cutting[30]. These properties facilitate the efficient absorption of impact energy, thereby elucidating their extensive utilisation in protective equipment and lightweight structural components. The primary limitations of these materials pertain to their comparatively low compressive strength, sensitivity to ultraviolet radiation and moisture, and potential degradation in aggressive chemical environments [31, 32]. Aramid fibres are typically produced by solution spinning, a process that aligns the polymer chains along the fibre axis [33].

UHMWPE fibres, including Dyneema and Spectra, consist of polyethylene chains of considerable length that are aligned predominantly in the direction of the fibre. Gel spinning is the principal production route, as it is able to reduce molecular entanglement and enable extensive chain orientation. The resulting fibres demonstrate a low density, high specific tensile strength, toughness and excellent ballistic-energy absorption [34]. However, their thermoplastic nature results in limited temperature resistance, viscoelastic creep under sustained loading and relatively weak surface adhesion to conventional polymer matrices. It is therefore vital that surface treatments and suitable interface design are given due consideration when UHMWPE fibres are incorporated into composite laminates [35].

Natural fibres encompass bast fibres, including those derived from sources such as flax, hemp, jute, and kenaf, leaf fibres, such as sisal and pineapple-leaf fibre, and seed fibres, including cotton. They are a renewable, biodegradable, inexpensive, and low-density material that can provide competitive specific properties in secondary structural applications [36]. However, their hydrophilic composition promotes moisture absorption, swelling and biological degradation, while their natural variability leads to less uniform properties than those of synthetic fibres. The compatibility of

these materials with hydrophobic polymer matrices is also limited, and fibre treatment or coupling agents are commonly required to improve interfacial adhesion [37].

The selection of an organic reinforcement is therefore dependent on achieving an optimal balance between mechanical performance, impact resistance, thermal stability, environmental durability and cost. Aramid and UHMWPE fibres are especially relevant to the ballistic applications considered in this work, while natural fibres provide a sustainable alternative for less demanding structural components.

2.1.3 Hybrid Composite Laminates

The fabrication of polymer-matrix composite components is typically accomplished through the stacking of thin laminae to form a laminate. It is important to note that each ply may contain unidirectional (UD), bidirectional or woven reinforcement, and consequently exhibits direction-dependent mechanical properties. It has been demonstrated that UD plies exhibit optimal stiffness and strength when aligned along the fibre direction. In contrast, the transverse response is predominantly influenced by the matrix and the fibre-matrix interface. The combination of plies with different orientations, including cross-ply, angle-ply and quasi-isotropic configurations, enables the laminate response to be tailored to the loading conditions and structural requirements of a particular application [38]. As illustrated in Figure 2.2, the various stacking configurations are presented.

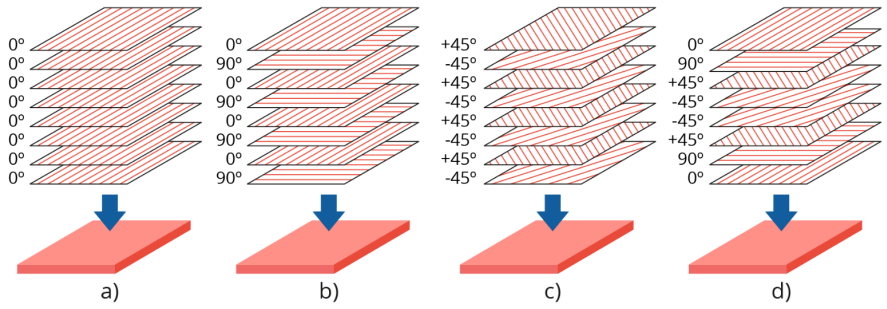


Figure 2.2: Examples of laminates configurations: (a) Unidirectional, (b) Cross-ply, (c) Angle-ply and (d) Quasi-isotropic [39].

The design approach is further extended by hybrid laminates, which combine two or more reinforcement or material systems within the same structure. The objective is to exploit complementary properties that cannot readily be achieved using a single constituent. Such properties include the stiffness of carbon fibres, the toughness of glass or aramid fibres, and the low density and energy-absorption capacity of UHMWPE. The resulting behaviour is contingent on the constituent properties, relative volume fractions, stacking sequence and quality of the interfaces. Appropriate hybridisation has been demonstrated to enhance damage tolerance, delay delamination, and reduce material cost. However, these benefits may be accompanied by increased manufacturing complexity and more intricate failure mechanisms [40].

Fibre-metal laminates represent a significant category of hybrid structures, characterised by the alternation of thin metallic sheets with layers of Fibre-Reinforced Polymer (FRP). Representative systems include Glass Reinforced Aluminium Laminate (GLARE), Aramid-Reinforced Aluminium Laminate (ARALL) and Carbon Reinforced Aluminium Laminate (CARALL). The combination of these materials results in a synthesis of the ductility, impact resistance and damage visibility of metals with the high specific stiffness, fatigue resistance and corrosion resistance of FRP. The favourable structural efficiency exhibited by these materials has thus far supported their application in the field of aerospace engineering, particularly with regard to the manufacture of impact-resistant components. However, it should be noted that their performance remains sensitive to interfacial adhesion, residual stresses and delamination under severe loading [41].

Beyond their mechanical efficiency, hybrid laminates offer the potential for cost optimisation and enhanced material utilisation. The integration of cost-effective fibre systems in conjunction with high-performance materials enables a reduction in overall material expenditures without substantial compromise to performance. Furthermore, favourable interactions between constituent materials, such as enhanced crack deflection or delayed delamination, have the potential to augment damage tolerance and fatigue life. Consequently, hybrid laminates are well-suited for applications necessitating repeated or multi-hit resistance [38].

2.1.4 Composites in Aeronautical Engineering

The utilisation of composite materials within the aeronautical industry is undergoing consistent expansion. FRP matrices represent the predominant category of this material within the industry. This can be justified by their high specific strength and stiffness. In addition to these inherent properties, the possibility of tailoring their characteristics according to the specific application under consideration constitutes a further substantiating factor. The utilisation of composite materials instead of conventional aeronautical metals, such as steel and aluminium, is advantageous in terms of enhanced resistance to fatigue and corrosion [12, 42].

Despite its considerable appeal, the introduction of the concept into the aeronautical industry, within both civilian and military contexts, has been subject to rigorous oversight by the relevant certification authorities. In order to ensure that composite materials meet the high safety standards employed in the field of aeronautics, extensive testing is required, since these materials exhibit different behaviour to that of ordinary metallic materials. The utilisation of the "Building Block" strategy constitutes a commendable methodological approach for the investigation and demonstration of the behaviour of this particular material. The method is initiated with the execution of static, fatigue, and damage tolerance tests on coupons. These are then conducted on elements, followed by sub-components, and culminating in full-scale structures. In addition to providing support for the design and certification phase, it is also imperative for enhancing manufacturing processes [3, 12].

As previously stated, the utilisation of composite components in the field of aircraft engineering has the potential to reduce the structural weight of the aircraft. Nevertheless, the reduction in weight is concomitant with a number of advantages, including a reduction in fuel consumption,

an increase in the capacity for cargo and a reduction in both wing area and engine power. The combination of these advantages with the tailoring capability offered by composites has the potential to enhance the aerodynamic performance of structures such as wings and empennage, thereby increasing the overall efficiency of aircraft [12, 42].

In the domain of military aviation, there is a multitude of instances that illustrate the utilisation of composite materials. The earliest documented instances of the utilisation of these materials are from the 1950s, at which time their application was limited to a small number of components. In the contemporary aircraft, their utilisation is imperative, with their presence being a feature of the majority of the aircraft's structures. Structures of this nature encompass wings, empennage, vertical stabilisers, fuselages, doors/covers and engine components [12, 43].

As demonstrated in Figure 2.3, the proportion of composite structures in relation to the total weight of aircraft has been traced from the 1970s to the end of the 2010s. With regard to military aviation (indicated in blue), it is possible to observe a growth trend by comparing, for instance, the F/A-18C/D (1980s), which has approximately 10% of its composition made up of composites, to the most recent F-35 JSF (2010), which has a percentage of approximately 40%. Indeed, this tendency is also observable in the domain of civil aviation. To illustrate this point, the MD-80 aircraft (1970) had only 10% of its structural weight in composite material, whereas contemporary aircraft such as the B787 and A350 have values of around 50%. This is a key factor in ensuring their successful performance [4].

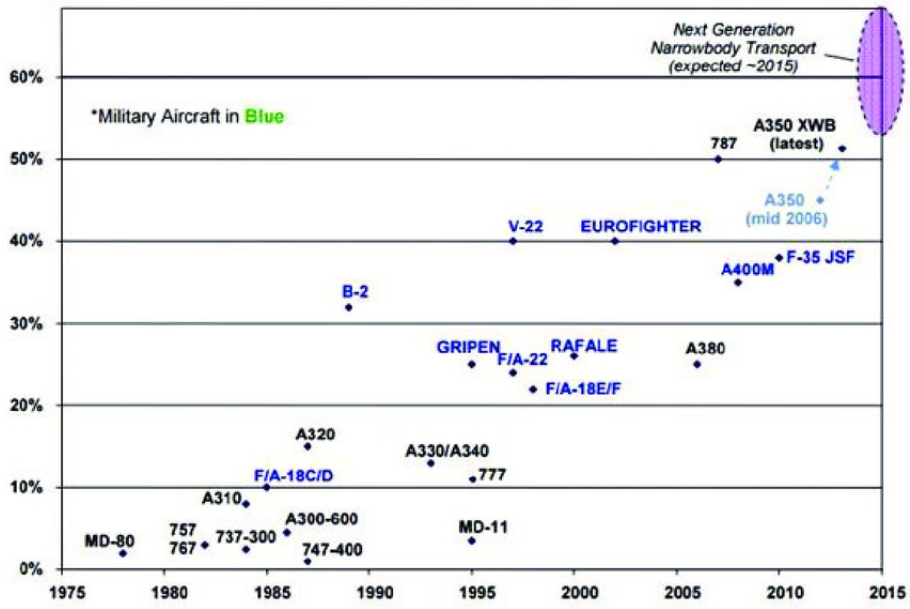


Figure 2.3: Evolution of composites in the aeronautical industry [4].

To illustrate the practical application of composites, the Lockheed S-3A aircraft, developed in the 1960s for submarine surveillance, was initially equipped with aluminium spoilers weighing approximately 5.9 kg each. Subsequently, an alternative was developed which incorporated CFRP and a honeycomb core. The final weight was determined to be 3.6 kg, representing a reduction of

approximately 40% [42]. In the 1990s, composite materials were incorporated into various structures of the Lockheed Martin F-22 Raptor. As illustrated by the F-22's spars, skin, empennage, and fuselage, which collectively represent approximately 23% of the aircraft's structural weight, the utilisation of CFRP is a prominent feature in modern aerospace engineering [42, 43]. A more contemporary example is the C-390 Millennium aircraft, which was developed by Embraer for the purpose of multi-mission transport. The design incorporates composite materials in elements such as the flaps, ailerons, rudder and horizontal tail plane [44, 45].

2.2 Military Aircraft Certification

Aviation systems, in both civil and military contexts, are designed to fulfil specific operational objectives in a manner that optimises the utilisation of available resources. Nevertheless, a considerable divergence exists among their fundamental missions, operational constraints, and performance expectations. Civil aviation is an industry that is inherently commercial in nature. It is characterised by the generation of revenue and is driven by market-driven investments. There is an overarching emphasis on consistent safety, efficiency, and service reliability. Conversely, the domain of military aviation is geared towards the fulfilment of strategic national interests. Its operational scope encompasses a range of missions, including search and rescue, reconnaissance, air defence, and logistical support. These operations are frequently undertaken in environments characterised by volatility and hostility. It is evident that the operations in question are state-funded, and as such, mission success is prioritised over cost-efficiency. Consequently, the notion of a mission is understood in a divergent manner across the two domains. In the domain of civil aviation, a mission is defined as the operation of transporting passengers or cargo in a safe and efficient manner from one location to another. Conversely, the domain of military aviation is characterised by the delineation of missions in terms of the attainment of specific operational objectives. These objectives frequently entail the execution of complex, high-risk operations that transcend the scope of transportation, encompassing activities such as surveillance, combat engagement, and the provision of logistical support within conflict-affected regions [26, 46].

Moreover, disparities are evident in the composition of fleets and the operational scale employed. Civil fleets characteristically exhibit two distinguishing features: firstly, they are typically large in size; secondly, they are homogeneous in nature. These features are optimised for standardised operations across global routes. In contradistinction, military fleets are characterised by their smaller size, greater diversity with regard to aircraft types, and customisation in accordance with specific operational requirements. It should be noted that such fleets are often produced in limited quantities. It is evident that these variations also have an impact on safety thresholds. Civil aviation is characterised by the adherence to rigorous and consistent safety standards. In contrast, military aviation may be associated with an elevated degree of operational risk, particularly in wartime contexts where limitations on airworthiness may be more readily accepted. It is evident that, despite both sectors considering safety to be of paramount importance to operational

integrity, the acceptable level of risk and the regulatory frameworks governing their airworthiness are inherently shaped by their divergent purposes and environments [26].

In the ensuing sections, an exhaustive examination of the military certification frameworks of Europe and the United States will be conducted. The focus will be on the regulatory structures, certification processes, and key documentation of these frameworks, with particular attention given to aspects pertinent to aircraft survivability and protection systems.

2.2.1 European Military Certification Network

In contrast to the domain of civil aviation, which is overseen by a centralised regulatory authority, the European Union Aviation Safety Agency (EASA), military aviation functions without the benefit of a universally binding international regulatory framework. It is evident that each nation maintains its own Military Aviation Authority (MAA), the remit of which is the development and application of national airworthiness requirements. This decentralised model has resulted in significant heterogeneity in certification approaches, thereby rendering cross-border collaboration a particularly complex undertaking [5].

In response to the issue of fragmentation, the European Defence Agency (EDA) was established in 2004 with the objective of enhancing defence cooperation within the European Union (EU). One of the primary objectives of the initiative was to foster greater integration and competitiveness within the European defence equipment market, while concurrently fortifying the technological and industrial foundations of the continent's defence sector. The EDA has pursued a policy of encouraging joint capability development and greater harmonisation across Member States, with a particular emphasis on technical domains such as certification. It is acknowledged that civil aviation standards are characterised by a high level of maturity and efficiency. In light of this, the EDA concluded that the EASA framework constituted a viable foundation for military application. This strategic decision resulted in the transposition of EASA's principles to the defence sector [5, 47].

In 2008, the EDA inaugurated the Military Airworthiness Authorities (MAWA) Forum, which convened representatives from national MAAs. The fundamental objective of the Forum was to establish a harmonised military airworthiness system across Europe through the implementation of common requirements, procedures, and mutual recognition. A structured roadmap was formulated, endorsed by ministerial consensus, with the objective of developing a unified regulatory framework, shared certification processes, common design codes and organisational approvals, and long-term mechanisms for joint oversight. This initiative constituted the foundational element for the establishment of the European Military Airworthiness Requirements (EMARs) [47].

The EMARs represent a series of military airworthiness regulations, the implementation of which is to be undertaken by each national MAA. This ensures that each country retains sovereignty while contributing to an interoperable and recognisable certification system. It is evident that the regulations under discussion here are similar to the EASA regulatory model, but it should be noted that they have been adapted in such a way as to take into account military-specific conditions. It is evident that within the extensive corpus of EMARs, a number are of particular pertinence to

the subject of this dissertation, given their direct applicability to the domains of military aircraft design, maintenance, training, and ensuring ongoing airworthiness, along with the organisations involved in these processes [47, 48].

The following EMARs are the most relevant for the context of this work:

- EMAR 1: Definesthe general regulatory framework for military airworthiness, specifying responsibilities for initial certification and continuing airworthiness.
- EMAR 21: Governs the certification of military aircraft, parts, and appliances, and sets out requirements for Design and Production Organisation Approvals.
- EMAR 66: Specifies the requirements for the qualification and licensing of certifying staff responsible for maintenance activities on military aircraft, ensuring competence through knowledge, skills, and experience standards.
- EMAR 145: Establishes standards for military maintenance organisations, particularly in relation to procedures, qualified personnel, and quality management.
- EMAR 147: Regulates training organisations responsible for the certification and qualification of military maintenance personnel.
- EMAR M: Describes the Continuing Airworthiness Management framework, including maintenance scheduling, compliance tracking, and airworthiness reviews.

Concomitant with the EMARs, the MAWA Forum has developed a complementary set of documents known as European Military Airworthiness Documents (EMADs). The purpose of these documents is to facilitate the implementation, interpretation and mutual recognition of EMARs-based frameworks across Member States. For the purposes of this thesis, particularly in the context of certification, organisational approval, and test operations, certain EMADs are of particular pertinence. These are outlined briefly below [48–50].

- EMAD-R (Recognition): Defines a formal process for mutual recognition of certificates and approvals issued under the EMARs between different MAAs.
- EMAD-A(Arrangements): Outlines the administrative agreements required to implement EMARs in a harmonised and coordinated manner across participating nations.
- EMAD-G (Guidance): Provides technical interpretation and practical guidance to ensure consistent application of EMARs provisions.
- EMAD 1 (Military Airworthiness Policy): Sets out the strategic objectives and guiding principles for a coherent and cooperative European military airworthiness environment.
- EMAD 20 (European Military Design Organisation Approval (EMDOA)): Specifies requirements for the multinational approval and mutual recognition of military design organisations.

- Military Flight Test Permit (MFTP): Establishes the conditions under which experimental or prototype military aircraft may be operated for testing purposes prior to full certification.

In the European context, the certification of military aircraft is conducted through a structured and methodical process. This process draws from civil aviation principles, but is adapted with care to meet the unique operational and security demands of defence applications [51].

The process is initiated with the approval of the Design Organisation (DOA), which bestows upon an entity the authority to undertake the design and development of military aircraft and associated products. In order to receive such approval, it is incumbent upon the organisation to demonstrate that it possesses the technical capability, internal procedures, and safety assurance systems necessary to support airworthiness. It is an established regulatory framework that only organisations with a recognised DOA are permitted to engage in the certification of military aerospace systems [51, 52].

Subsequent to the establishment of design authority, it is imperative that the aircraft fulfils the criteria for both initial and continuing airworthiness. The concept of initial airworthiness is predicated on the principle of verifying that the design in question complies with all relevant military standards. This is particularly pertinent in relation to areas such as structural safety, system reliability, and overall compliance with airworthiness codes. In contrast to the concept of "continuing airworthiness" is defined as the maintenance of that compliance throughout the service life of the aircraft. This encompasses scheduled inspections, configuration control, defect monitoring, and adherence to maintenance requirements. This ensures that the aircraft remains safe and effective in operation [48, 52].

In the event of satisfactory demonstration of initial airworthiness, the relevant MAA is permitted to issue a Military Type Certificate (MTC). The MTC serves to provide formal confirmation that the aircraft design meets all mandatory military airworthiness criteria and is suitable for its intended operational role. The issuance of the MTC represents a critical milestone in the aircraft's progression towards operational deployment [52, 53]. Subsequent to this, the Release to Service (RTS) is issued at the national level by the competent authority. The RTS, in contrast to the MTC, is responsible for the certification of the design. In addition, the RTS takes into account the specific configuration, the current maintenance state, and any operational restrictions associated with a particular aircraft or fleet. The RTS is pivotal in ensuring a seamless interface between the regulatory oversight and the operational responsibilities of the military command, thereby guaranteeing that aircraft are not only technically certified but also operationally equipped for effective mission execution [51].

2.2.2 United States Military Certification Network

Contrasting to civil aviation, which in the United States (US) is regulated centrally by the Federal Aviation Administration (FAA), as previously mentioned, military aviation functions under a discrete system of governance. The designation of US military aircraft as public aircraft within

national borders and as state aircraft when operating internationally exempts them from FAA airworthiness procedures. The Department of Defense (DoD) functions as the primary governing body for military airworthiness. However, it delegates the responsibility for the implementation of these policies to the individual service branches. Each of the military services, that is to say the Air Force, Navy and Army, functions as an autonomous Military Airworthiness Authority. This means that they are responsible for developing and enforcing their own airworthiness policy, and they do so under the legal authority of their respective Secretary [54, 55]. This decentralised model enables each branch to customise certification frameworks according to its operational requirements. However, it also engenders regulatory divergence across the services [47].

In order to address the issue of fragmentation that has resulted, the DoD has developed a unifying policy structure with the intention of improving standardisation and enabling mutual recognition across the various service branches. A fundamental element of this initiative is the implementation of the DoD Joint Airworthiness Policy, which serves to formalise the process of authority derivation and delineates the respective responsibilities of the relevant airworthiness organisations. The policy stipulates that, in instances where aircraft are engaged in analogous roles, possess analogous configurations, and operate within analogous environments, the respective certifications of these aircraft are to be recognised by the relevant branches [54, 55]. The mechanism under discussion provides an operational bridge across services and improves the coherence of the certification landscape.

The fundamental principle underpinning the US military's harmonisation initiative is the implementation of a unified certification standard, as delineated in the document entitled MIL-HDBK-516. The MIL-HDBK-516C, first published in 2002 and now in its C revision, defines a set of comprehensive and performance-based airworthiness certification criteria applicable across all services [54]. The handbook provides comprehensive coverage of the fundamental domains of structural integrity, system safety, crashworthiness, human-machine integration and cybersecurity. The document under review does not stipulate particular design solutions. Rather, it establishes objectives that permit engineering flexibility whilst ensuring operational safety and compliance. It is this adaptability which renders it particularly suitable for the diverse operational profiles and technical architectures encountered in military aviation [56].

It is evident that each service implements the framework delineated in MIL-HDBK-516C, in accordance with its organisational structure and mission profile. The United States Air Force (USAF) is responsible for the management of airworthiness certification, a process which is overseen by the Air Force Life Cycle Management Center (AFLCMC). The Director of Engineering at the AFLCMC is designated as the Technical Airworthiness Authority (TAA). The aforementioned authority is responsible for establishing certification standards, issuing compliance findings, and authorising flight via MTCs. The USAF has codified its policy in AFPD 62-6 and implemented it via Air Force Instructions. However, there have been noted discrepancies between policy and execution. The devolution of operational and maintenance oversight responsibilities to the unit level, coupled with the enforcement of compliance through internal mechanisms rather than external independent evaluations, has the potential to compromise the reliability of assurance in these

domains [47].

In the US Navy and Marine Corps, the Chief of Naval Operations has designated the Commander of Naval Air Systems Command (NAVAIR) as the lead airworthiness authority. The responsibility is operationalised through the Airworthiness Office, which issues flight clearances as the Navy's formal airworthiness approval. The process is structured around a comprehensive systems engineering review and is closely associated with the documentation delineated in the Naval Aviation Maintenance Program (NAMP). Whilst the Navy's regulatory model integrates policy, process and oversight into a unified framework, this integrated approach has the potential to obfuscate the delineation between design, operational and maintenance responsibilities [47].

The US Army's regulatory framework for airworthiness is delineated in Army Regulation 70-62. The Deputy Chief of Staff is responsible for establishing policy, while the Commanding General of the Army Aviation and Missile Command is responsible for certification. The Army's certification methodology is comprised of three fundamental pillars: the assessment of design against the relevant standards, the definition of safe operating limits and the maintenance of compliance through the implementation of routine inspections and the execution of quality-controlled maintenance procedures. The Army's regulatory structure is characterised by a less centralised approach, whereby operational airworthiness and maintenance are governed by distinct and independently enforced policy documents. Maintenance assurance is validated through Aviation Resource Management Survey (ARMS) inspections, with a significant reliance placed on embedded quality management systems [47].

In the context of military aircraft certification, a structured process is employed across all services. This process commences with the designation of the design authority. It is imperative that organisations engaged in the development of aircraft demonstrate their technical capability, adherence to engineering standards, and internal safety oversight mechanisms, in order to be recognised as competent for certification activities. The certification process is usually based on MIL-HDBK-516C, which serves as the standard reference for the comprehensive airworthiness criteria applicable to both manned and unmanned systems throughout their entire lifecycle. The present handbook provides a standardised, bespoke set of criteria with which to evaluate design safety, structural integrity and system reliability. In accordance with the stipulated framework, the certification process encompasses both the initial and ongoing validation of the aircraft's airworthiness. Initial airworthiness is defined as the confirmation that a design meets all applicable technical and operational safety requirements. In contrast, continued airworthiness can be understood as the process of ensuring that compliance is maintained throughout the aircraft's service life through proper maintenance, defect tracking, and configuration control [57].

In the event of successful verification of the airworthiness requirements, the responsible Military Airworthiness Authority is required to issue a formal type approval. In the USAF, this process is known as a MTC, whereas in the Navy and Army, it is referred to as a flight clearance or airworthiness qualification. Whilst these approvals are necessary prerequisites for entry into service, they are not, in and of themselves, sufficient. It is imperative to recognise the necessity of an additional step, which is commonly undertaken in the form of an operational release or a flight

readiness review. This step is integral in ensuring that the specific aircraft or fleet is in an optimal state of configuration and maintenance, and that it is deemed safe for its intended operational use [58]. This ultimate authorisation functions as a conduit between the regulatory certification and the deployment of the mission, thereby ensuring that the aircraft meets both technical and tactical requirements [47].

2.2.3 Ballistic Testing Standards used by the US Military: The Case of MIL-STD-662F

This subsection specifically addresses the MIL-STD-662F military standard, entitled V_{50} *Ballistic Test for Armour*. This standard is utilised by some authors as a reference for numerical simulations [59].

The MIL-STD-662F method is a standardised procedure for the experimental determination of V_{50}, defined as *"the velocity at which the probability of penetration of an armour material is 50 percent"*. Its utilisation is directed towards the development of internal and external aircraft armouring, amongst other purposes, as evidenced in [59].

In order to facilitate a more profound comprehension of the standard, a comprehensive description is provided in Table 2.1, which enumerates and elaborates upon the constituent chapters. Moreover, Figure 2.4 presents a simplified depiction of the test setup. Initially, the plate/armour must be correctly affixed. A thin aluminium plate, known as a "witness plate", is positioned behind the subject. The function of the witness plate is to ascertain whether total or partial penetration has occurred. Following a series of firings, the V_{50} is calculated as the arithmetic mean between the highest total penetration velocity and the lowest partial penetration velocity [9, 59].

Table 2.1: MIL-STD-662F description [59]

Chapter	Description
1	Defines the objective of the standard and its applicability.
2	Lists the documentation used as a reference.
3	Lists and defines all the concepts/parameters used in the standard.
4	Presents the requirements for the materials to be used (projectile, weapon, measuring material, etc.).
5	Details the requirements for test preparation and conditions, for processing the data obtained, and for preparing the report.
6	Provides additional information.
Table I	Provides test velocities and distances for different projectiles.

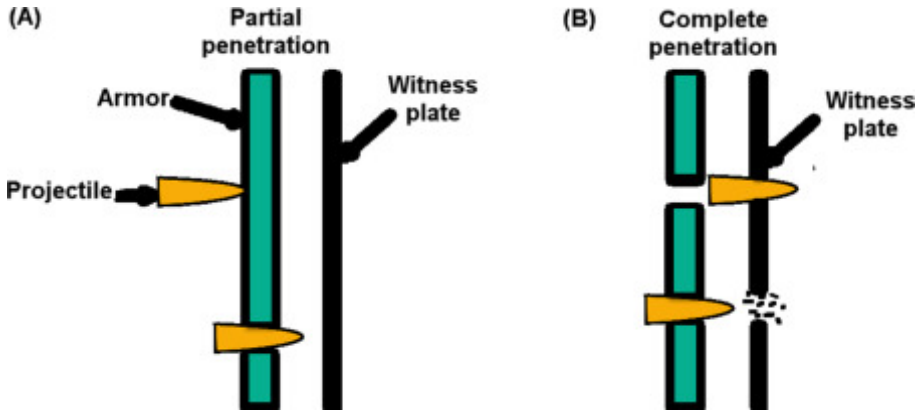


Figure 2.4: Schematic representation of the projectile impact outcomes: (A) Partial penetration and (B) Complete penetration [9].

2.3 Ballistic Protections

Ballistic protection can be defined as the design of systems which are intended to resist or absorb the energy of high-velocity projectiles. The aforementioned systems encompass personal protective equipment, including vests and helmets, as well as bomb blankets. In addition, they comprise rigid structures such as vehicle panels and protective shields. The selection of materials and configurations is contingent upon the nature of the threat, which may be constituted by knives, handguns, or rifle bullets, with the objective being to ensure effective protection [60].

Ballistic systems are typically categorised as either flexible or rigid. Flexible systems are defined as those which are wearable and composed of high-performance fibres arranged in woven, knitted, or nonwoven fabrics. Rigid systems frequently incorporate ceramic plates, including boron nitride and tungsten carbide, in conjunction with fibre-reinforced textiles such as Kevlar, Twaron, and UHMWPE materials, including Dyneema and Spectra. The configuration of these hybrid systems is such that the rigid plates serve to disperse the impact force, whilst the textile layers are responsible for the deformation of the projectile and the absorption of the residual energy. In both cases, the objective is to absorb and dissipate kinetic energy. In the case of soft armour, this is achieved through fibre stretching and rupture. By contrast, hard armour uses inserts to prevent penetration and blunt the bullet. The selection of material is contingent upon the velocity of the projectile, which can vary significantly depending on the type of weapon. For instance, handguns typically have a velocity of approximately 400 m/s, while rifles can reach speeds of up to 800 m/s [61].

In addition to considerations of personal protection, the design of military and structural components exposed to high-velocity impacts must also take ballistic resistance into account. The following categories are included: aircraft, land vehicles and infrastructure. Impacts of this nature have the potential to result in penetration or fragmentation, which in turn necessitates materials that are capable of withstanding extreme loading conditions [62].

2.3.1 Hybrid Laminates for Ballistic Applications

The development of lightweight, high-performance armour systems has recently focused on the use of hybrid laminates. The formation of these composites is achieved through the amalgamation of diverse reinforcing fibres, with the objective of optimising protection, energy absorption, and structural integrity. The impetus for hybridisation stems from the potential to leverage disparate material properties within a layered configuration, thereby facilitating a more efficacious response to ballistic threats [63].

In the early stages of development, hybrid systems were frequently composed of aramid fibres, such as Kevlar, due to their ability to withstand significant levels of stress and their resistance to degradation when exposed to high temperatures. The combination of aramids with brittle but hard ceramics or stiff carbon fabrics has been demonstrated to enhance energy dissipation and curtail damage propagation in multilayer configurations [64]. Glass fibres have also been used in hybrid panels as a cost-effective alternative, although their lower energy absorption compared to aramids and polyethylenes has limited their use in high-threat scenarios [63].

In recent years, there has been a paradigm shift in focus towards UHMWPE, a material that has been demonstrated to exhibit a high strength-to-weight ratio, low density, and superior ballistic resistance. UHMWPE fibres possess viscoelastic properties and are capable of significant deformation prior to failure. This characteristic renders them highly effective in the absorption and dispersion of kinetic energy from projectiles.The function of these elements within the context of hybrid laminates is frequently that of backing layers. In this capacity, they collaborate with harder strike-face materials, such as carbon or ceramic, to blunt, break and decelerate the incoming projectile [65].

Recent experimental findings indicate that the ratio and sequencing of hybrid materials have a substantial impact on performance. A study was conducted using carbon/UHMWPE laminates, which demonstrated that an increase in the proportion of UHMWPE resulted in enhanced energy absorption and a reduction in backface deformation. A configuration with 75% UHMWPE and 25% carbon, for instance, has been shown to successfully stop 7.62 mm projectiles while achieving lower bulge height and slower deformation rate compared to pure UHMWPE or carbon laminates [65].

The structure and orientation of UHMWPE layers have been demonstrated to have a substantial impact on ballistic performance. A study was conducted to ascertain the impact of stacking sequence on the properties of woven and UD UHMWPE fabrics in hybrid laminates. The findings of this study indicated that stacking sequence is a critical factor in determining the performance of these materials. In the configuration of panels, the employment of woven layers at the front in conjunction with UD layers at the rear has been demonstrated to yield superior performance. This configuration has been shown to minimise backface deformation and maximise energy absorption. The findings of both experimental trials and finite element simulations have identified an optimal hybrid ratio consisting of 25% woven and 75% UD UHMWPE [66].

As indicated by the extant literature, hybrid laminates incorporating UHMWPE have been the

subject of extensive research in relation to their performance in ballistic applications. The significance of the modular design, low weight and energy dissipation characteristics of the system has been thoroughly researched and is considered a primary factor for utilisation in military systems, particularly in scenarios where protection and mobility are of paramount importance [65, 66].

2.3.2 Ballistic Protection Development and Pratical Examples

The initial methodologies employed in the realm of ballistic protection were predominantly characterised by a process of trial and error experimentation. The designs were subjected to a process of iterative testing and modification, a process which was both time-consuming and costly due to the expense of advanced materials and full-scale ballistic trials, until such time as the required performance was achieved. The advent of computational modelling, most notably the Finite Element Method (FEM), precipitated a paradigm shift in this process by enabling engineers to simulate impact events utilising established material properties and defined loading conditions [67]. Contemporary development strategies now integrate virtual simulations with physical testing. The utilisation of simulations serves to refine designs and minimise the necessity for prototypes, while targeted experiments remain imperative for the validation and calibration of numerical models. This integrated approach has been demonstrated to have a significant impact on development costs, with a notable acceleration in the innovation process. This assertion is supported by the widespread utilisation of FEM platforms, such as Abaqus, CATIA V5 and Ansys [9].

In the domain of military aviation, the implementation of complete airframe armour is deemed impractical. This is primarily due to the substantial weight penalties that would be incurred, which would have a detrimental effect on aircraft performance. In contrast, protection is applied in a selective manner through the utilisation of modular armour systems. These systems are designed to safeguard exclusively the areas that are deemed to be most vulnerable or mission-critical. Specialist manufacturers supply composite or hybrid panels that are tailored for installation in a variety of locations, including but not limited to pilot and co-pilot seats, cargo doors, floors, loading ramps, and engine nacelle fairings, as illustrated in Figure 2.5. The design of these systems is underpinned by advanced numerical modelling, most notably finite element analysis. This is supported by standardised ballistic testing, which is used to ensure compliance with military protection standards [68, 69].



Figure 2.5: Ballistic protection for aircraft and helicopters [68].

A notable operational illustration of this approach is evident in the A-10C Thunderbolt II, an aircraft designed for close air support missions in high-threat environments. The aircraft was introduced into service in 1977 with the objective of providing assistance to ground forces. It is equipped with a ballistic protection box, which is referred to as the "bathtub" due to its geometric configuration. This device is designed to protect the pilot and certain flight control systems. In order to achieve the required specifications, the structure was fabricated from 3.8 cm-thick plates of titanium, with a total weight of approximately 550 kg. The cockpit enclosure of the vehicle is engineered to ensure the protection of the pilot and critical flight controls from ground fire. The armour has been tested and proven to withstand direct hits from 23 mm armour-piercing projectiles and, in certain instances, larger calibre rounds [6]. As illustrated in Figure 2.6, the A-10C Thunderbolt II is presented in conjunction with a close-up view of its titanium "bathtub" armour, thereby emphasising its geometry and the manner in which it encloses the pilot within the cockpit structure.

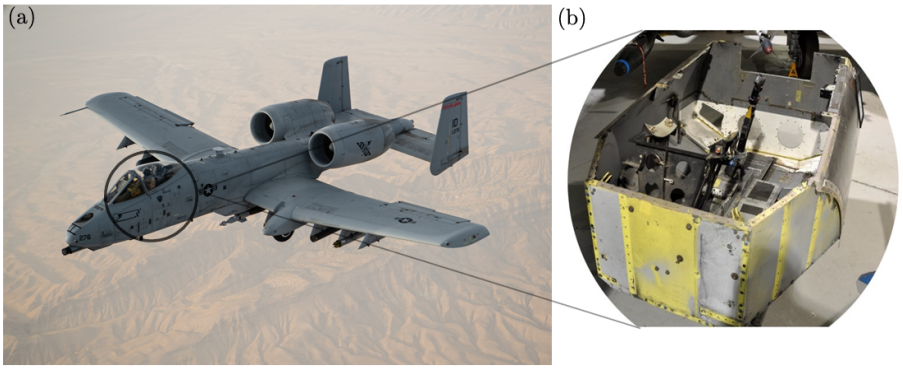


Figure 2.6: (a) A-10C Thunderbolt II ("Warthog"), (b) Titanium "Bathtub" [6].

2.4 Impact Velocity Regime

The categorisation of impact events into discrete velocity regimes is predicated upon the manner in which energy is transferred from the projectile to the target, the mechanisms of energy dissipation, and the nature of damage produced in the target. As the projectile velocity undergoes change, these factors can vary significantly, thus resulting in distinct categories: low-velocity, intermediate-velocity, high-velocity (ballistic), and hypervelocity impacts [62].

From a structural dynamics perspective, an impact is considered to be low-velocity if the duration of contact exceeds the fundamental period of vibration of the structure. By way of contrast, high-velocity or ballistic impacts are distinguished by contact durations that are considerably shorter than the lowest natural period of the target. In the most extreme cases, the projectile's velocity is such that the material behaviour in the immediate vicinity approximates that of a fluid. This phenomenon is known as hypervelocity impact, and it occurs when a projectile moves at speeds that are so great that the material undergoes a transition in its behaviour from a solid to

a fluid [62]. The term "ballistic impact" is typically used to describe the impact of low-mass projectiles moving at high speeds, often generated by a propelling device.

In the context of practical engineering and testing, impact velocities are frequently delineated by means of approximate numerical ranges. Low-velocity impacts are typically characterised by velocities below 10 m/s, intermediate-velocity impacts are classified as those between 10 m/s and 50 m/s, high-velocity impacts are defined as those ranging from 50 m/s to 1000 m/s, and hypervelocity impacts are defined as those extending from 2000 m/s to 5000 m/s [70, 71]. The precise boundaries are contingent on the stiffness of the target, its material properties, and the mass and stiffness of the projectile [71].

Low-velocity impacts represent a particular concern for composite structures in service, as they have the potential to occur during operation or maintenance and may result in damage that is barely visible to the naked eye. The typical effects of this phenomenon include matrix cracking, fibre breakage and interlaminar delamination, particularly at ply interfaces with different fibre orientations. This can significantly reduce residual tensile and compressive strength. The assessment of such events is typically conducted through the utilisation of standardised methodologies, encompassing the employment of pendulum devices (Charpy and Izod tests) and instrumented drop-weight towers. The latter approach facilitates the exploration of a more extensive range of geometries and enables the execution of more representative component tests [70, 71].

It has been established that impacts of intermediate velocity result in greater levels of damage in comparison to those of low velocity. This is due to an increased potential for through-thickness cracking and fibre fracture. The impact of such occurrences is, on occasion, not addressed with the requisite frequency in the standards that are applied in the context of certification. Nevertheless, in certain operational scenarios, such as instances of heavy tool drops or runway debris strikes, these impacts can be considered to be of relevance.

It is an established fact that high-velocity or ballistic impacts are capable of causing immediate and catastrophic damage to aerospace and automotive structures. In the domain of aviation, pertinent examples encompass the presence of foreign objects resulting in damage to turbine blades, and the impact of debris on leading edges, canopies, and radomes. The velocities involved can be sufficiently high to cause instantaneous penetration or gross structural failure. The experimental investigation of such events is typically conducted using single-stage launchers, such as powder guns or gas guns. The latter are capable of achieving projectile velocities in the range of 2.0–2.2 km/s [71].

In the field of space applications, hypervelocity impacts represent a primary concern. In such cases, the effects of micrometeoroid and orbital debris impacts can induce localised shock loading and cause severe structural erosion. In such conditions, both the projectile and the impacted material have been observed to demonstrate fluid-like behaviour upon contact [62].

2.5 Dynamic Explicit Finite Element Modelling

As previously discussed in Section 2.3.2, the FEM has become an indispensable tool in the design and optimisation of ballistic protection systems. The FEM enables engineers to replicate complex impact scenarios virtually before proceeding to experimental validation. As was outlined in the preceding discussion, numerical modelling has a well-established role in reducing development costs and accelerating innovation.

The finite element method (FEM) has become one of the most significant tools in engineering for the numerical simulation of complex systems. The method under discussion enables the resolution of differential equations that govern physical phenomena through the discretisation of geometry into finite elements. In this framework, nodal values are approximated by means of shape functions, and the global behaviour is captured by assembling the contributions of all individual elements. This methodology has been demonstrated to be especially useful in the resolution of problems involving complex geometries, heterogeneous materials, and non-trivial boundary conditions [72, 73].

In the field of structural dynamics, the finite element method (FEM) facilitates the simulation of time-dependent events, including vibrations, impacts, and explosions. The simulations are driven by the governing equation of motion,

$$M\ddot{u} + C\dot{u} + Ku = f \tag{2.1}$$

In this equation, M is the global mass matrix, C is the damping matrix, K is the stiffness matrix and u is the nodal displacement vector. Its first and second time derivatives, $\dot{u}$ and $\ddot{u}$, represent the nodal velocity and acceleration vectors, respectively, while f is the external force vector containing the applied nodal loads [74]. The mass matrix, M, can be constructed using either a distributed (consistent) or a lumped formulation. In explicit time integration, including the formulation adopted in this study, a lumped mass matrix is typically preferred. This approach concentrates the element mass at the nodes, producing a diagonal matrix that allows nodal accelerations to be calculated without solving a coupled system of equations. Consequently, the computational cost of each time increment is reduced. The damping matrix, C, can be formulated using proportional or non-proportional damping approaches. A common proportional formulation is Rayleigh damping, in which C is expressed as a linear combination of the mass and stiffness matrices. This representation simplifies modal analysis by allowing the damping terms to be decoupled in the undamped modal basis. Non-proportional damping does not generally permit this decoupling and may be required to represent spatially heterogeneous or localised dissipative mechanisms that cannot be adequately described by a proportional formulation.

In order to compute the response of the system over time, two distinct numerical strategies are employed: implicit and explicit time integration. It has been demonstrated that, whilst both approaches solve the same governing equation, there is a discrepancy in the manner in which the unknown variables are estimated at each time step [74].

The following simplified example is provided to facilitate a more profound comprehension of this distinction. It is imperative to consider a generic function, $f(t)$, where the value at a known time, t_1, is given and the objective is to estimate the value at a future time, $t_1 + 1$. The explicit method is employed to calculate the derivative at the specified point, t_1, thus yielding the following expression,

$$f(t_1 + 1) = f(t_1) + \Delta t \cdot \left.\frac{df(t)}{dt}\right|_{t=t_1} \tag{2.2}$$

Conversely, the implicit method evaluates the derivative at the unknown point $t_1 + 1$,

$$f(t_1 + 1) = f(t_1) + \Delta t \cdot \left.\frac{df(t)}{dt}\right|_{t=t_1+1} \tag{2.3}$$

In these equations, $f(t)$ denotes a time-dependent variable, Δt signifies the time increment between successive time steps, and $\frac{df(t)}{dt}$ represents the slope of the function. The implicit method is contingent upon values that have yet to be determined. Consequently, the utilisation of iterative numerical procedures is imperative for the convergence of the solution. The explicit method avoids iteration by utilising solely known values, thereby engendering a more expeditious and direct computation [74]. This distinction is visually represented in the example function presented in Figure 2.7.

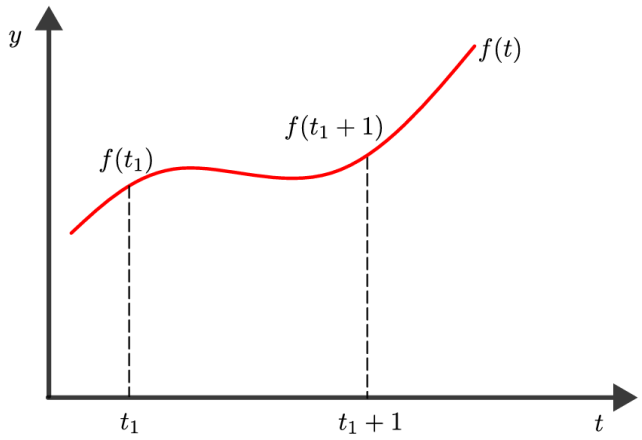


Figure 2.7: Example function $f(t)$.

The suitability of each method is influenced by these characteristics. Implicit solvers are generally considered to be the preferred option for problems that are characterised by slow evolution. Such problems include static analyses, creep, and thermal expansion, where the utilisation of longer time steps and unconditional stability is deemed advantageous. Nevertheless, this approach is accompanied by a greater computational demand, necessitating matrix inversion and convergence checks. Explicit solvers are more appropriate for problems involving short-duration, high-speed phenomena where large deformations, contact, and material failure are expected [75].

The explicit method is predicated on the central difference integration scheme, which advances the solution through time by means of a leap-frog approach. The acceleration at time t_i is calculated by means of the following formula,

$$\ddot{u}_i = M^{-1}(f_i^{\text{ext}} - f_i^{\text{int}}) \tag{2.4}$$

In this expression, $\ddot{u}_i$ is defined as the acceleration vector at time increment i, f_i^{ext} is defined as the force vector at time t_i, f_i^{int} is defined as the internal force vector developed within the elements and M is defined as the lumped mass matrix, which is diagonal to enable fast inversion [74].

Once the acceleration has been ascertained, the velocity and displacement are to be updated by means of the following equations,

$$\dot{u}_{i+\frac{1}{2}} = \dot{u}_{i-\frac{1}{2}} + \Delta t \cdot \ddot{u}_i \tag{2.5}$$

$$u_{i+1} = u_i + \Delta t \cdot \dot{u}_{i+\frac{1}{2}} \tag{2.6}$$

In the context of the given equation, $\dot{u}_{i\pm\frac{1}{2}}$ are the velocities at staggered time steps (midpoints),u_{i+1} is the displacement at the next full time step and Δt is the explicit time increment. The procedure is characterised by its use of known quantities and its avoidance of stiffness matrix assembly. These properties contribute to its high level of efficiency and its suitability for use with large, nonlinear models.

Despite its efficiency, the explicit method is conditionally stable. It is imperative that the time increment satisfies a stability condition based on the maximum natural frequency $\omega_{\max}$ of the system.

$$\Delta t \leq \frac{2}{\omega_{\max}} \tag{2.7}$$

In this condition, the maximum frequency of the model, designated as $\omega_{\max}$, is contingent upon the parameters of stiffness, density, and element size. As the mesh is refined or the stiffness increases, the maximum angular velocity rises, leading to smaller, more stable increments Δt and consequently a higher number of time steps being required to simulate the same physical duration. The effect was especially pronounced in the ballistic impact analyses conducted in this study. In such analyses, highly refined meshes were necessary to accurately capture stress wave propagation and localised damage. Whilst this refinement did guarantee the physical fidelity of the simulations, it also led to a substantial reduction in the stable time increment, which resulted in an increase in the computational cost. Notwithstanding, the explicit method continues to be a potent and dependable technique for simulating dynamic problems involving intricate contact interactions, progressive damage and fragmentation [74].

2.5.1 Element Size Requirements for Resolving Stress Waves

The frequency-based stability condition that was introduced previously (Equation 2.7) can also be expressed in terms of stress wave propagation and the size of the finite elements [74]. This alternative formulation is of particular pertinence for explicit simulations, as it provides a more intuitive and practical criterion for mesh design [76].

In explicit analysis, it is imperative that the stable time increment is sufficiently small in order to ensure that a dilatational (longitudinal) wave can traverse each element within a single time step. In the event of this condition not being met, there is a possibility that the numerical integration scheme will become unstable. Furthermore, the wave may bypass elements without adequately interacting with them, which will result in a loss of accuracy [76].

The general stability condition, accounting for potential damping effects, is given by:

$$\Delta t_{\text{stable}} \leq \frac{L}{c_d} \cdot \frac{1}{\sqrt{1+\xi}} \tag{2.8}$$

In this equation, the maximum allowable time increment is denoted by Δt_{stable}, the characteristic element length is indicated by L, the dilatational wave speed of the material is represented by c_d, and the damping-related term is denoted by ξ [76]. In the present study, no supplementary damping mechanisms such as Rayleigh damping or viscoelastic behaviour were implemented. Consequently, the parameter of damping, ξ, was set to zero, a critical factor in maintaining the stability condition.

The wave speed c_d is defined as the velocity at which compressive disturbances propagate through an elastic medium. The following definition can be given in terms of the Lamé parameters,

$$c_d = \sqrt{\frac{\hat{\lambda}+2\hat{\mu}}{\rho}} \tag{2.9}$$

where $\hat{\lambda}$ and $\hat{\mu}$ are the first and second Lamé parameters, respectively, and ρ is the material density. These parameters are functions of more commonly used engineering constants, namely Young's modulus, E, and Poisson's ratio, ν, and can be expressed as,

$$\hat{\lambda} = \frac{E\nu}{(1+\nu)(1-2\nu)} \tag{2.10}$$

$$\hat{\mu} = \frac{E}{2(1+\nu)} \tag{2.11}$$

The wave-speed calculations for the hybrid laminate take into account the mechanical properties and densities of both the composite and the aluminium constituents. Since the laminate is heterogeneous and anisotropic, these constituent properties should not be interpreted as a single set of isotropic properties for the entire laminate. For a homogeneous, isotropic material, substituting the Lamé relations into the preceding equation yields the wave speed in terms of E, ν and ρ,

$$c_d = \sqrt{\frac{E(1-\nu)}{\rho(1+\nu)(1-2\nu)}} \tag{2.12}$$

In order to resolve wave propagation with sufficient accuracy, it is necessary that the element length L_e is smaller than the wavelength of the highest frequency of interest in the problem [76]. In the absence of other factors, numerical dispersion may occur, which may result in an inaccurate capture of the stress wave. The requirement is defined by the following criterion,

$$L_e \leq \frac{\lambda_{\min}}{n} \tag{2.13}$$

where $\lambda_{\min}$ is the shortest wavelength that needs to be resolved and n is a safety factor typically taken as 10. The wavelength is related to the wave speed by,

$$\lambda_{\min} = \frac{c_d}{f_{\max}} \tag{2.14}$$

The maximum frequency corresponding to $f_{\max}$ is indicated here. It is evident that the mesh resolution is sufficiently fine to capture the physics of wave propagation in dynamic events, such as impacts or high-speed deformations [76]. As outlined in Section 4.2.7.1 the CFRP laminates, the calculations were explicitly conducted to ascertain the adequacy of the selected element sizes in resolving stress wave propagation in both instances.

Chapter 3

Failure Models Theoretical Description

The preceding review of the extant literature addressed the various failure mechanisms of composite materials during an impact event. In order to simulate this material type accurately in such scenarios, it is necessary to use material models that include failure criteria, i.e. the parameters that indicate whether failure occurs. Such models must also describe the evolution of damage.

The literature presents several failure criteria, ranging from global empirical formulations to mode-specific approaches. Criteria such as Tsai-Wu, Tsai-Hill, Azzi-Tsai, Hoffman and Chamis are mainly based on calibrated mathematical expressions from experimental procedures and do not explicitly distinguish matrix and fibre failure. In contrast, models such as Hashin, Puck, Yamada-Sun and Chang-Chang evaluate these mechanisms separately, providing a more detailed description of composite damage [77, 78].

The failure criteria employed in the development of this work are as follows:

- Hashin criterion in 2D and 3D formulations;
- Cohesive zone model to analyse interlaminar damage;
- Johnson-Cook model for aluminium materials.

The present chapter delineates the theoretical basis of the failure models and damage evolution laws that have been adopted to describe the mechanical response of the hybrid composite shields under impact loading developed in this work. The models selected for analysis encompass intralaminar damage in composite plies, ductile plasticity and failure in metallic layers, and interlaminar degradation between adjacent laminae. In this context, failure is not represented by a single scalar limit, but by a set of mechanisms associated with fibre rupture, matrix cracking, plastic flow, delamination and progressive stiffness degradation.

3.1 Hashin Failure Criterion

The development of the Hashin criterion began with the work of Z. Hashin and A. Rotem in 1973, where the approach was presented as the Hashin-Rotem criterion [79]. This initial proposal was

later extended by Hashin in 1980, giving rise to the formulation that is now commonly applied in both two-dimensional (2D) and 3D composite failure analyses [80].

The main feature of this criterion is the separation of intralaminar failure into four independent mechanisms: tensile failure of the fibres, compressive failure of the fibres, tensile failure of the matrix and compressive failure of the matrix. For each mechanism, a specific quadratic expression is evaluated. When the value of the corresponding failure function becomes equal to or greater than one, the onset of damage is considered to have occurred.

Although the criterion is available in 2D and 3D forms, its scope is restricted to damage developing within the lamina itself. Consequently, interlaminar phenomena, particularly delamination, are not represented by the Hashin equations. This limitation is relevant in the present context because, as discussed in the literature review, delamination is a common consequence of impact loading and may explain deviations between finite element predictions and experimental results when it is not modelled separately.

As previously stated, this criterion serves to differentiate between the failure of the matrix or the reinforcement/fibre. Furthermore, a distinction is to be made between the failure of the constituent intention and compression. In order to achieve the desired result, the application of a series of stress tests and allowable stresses is necessary. The formulation for the 3D version is presented below [77, 80].

Fibre failure in tension ($\sigma_{11} \geq 0$)

$$\left(\frac{\sigma_{11}}{X_T}\right)^2 + \left(\frac{\sigma_{12}}{S_{12}}\right)^2 + \left(\frac{\sigma_{13}}{S_{13}}\right)^2 \geq 1 \tag{3.1}$$

Fibre failure in compression ($\sigma_{11} < 0$)

$$\left(\frac{\sigma_{11}}{X_C}\right)^2 \geq 1 \tag{3.2}$$

Matrix failure in tension ($\sigma_{22} + \sigma_{33} \geq 0$)

$$\left(\frac{\sigma_{22} + \sigma_{33}}{Y_T}\right)^2 + \frac{1}{S_{23}^2}(\sigma_{23}^2 - \sigma_{22}\sigma_{33}) + \left(\frac{\sigma_{12}}{S_{12}}\right)^2 + \left(\frac{\sigma_{13}}{S_{13}}\right)^2 \geq 1 \tag{3.3}$$

Matrix failure in compression ($\sigma_{22} + \sigma_{33} < 0$):

$$\left(\frac{\sigma_{22} + \sigma_{33}}{2S_{23}}\right)^2 + \left[\left(\frac{Y_C}{2S_{23}}\right)^2 - 1\right]\frac{\sigma_{22} + \sigma_{33}}{Y_C} + \frac{1}{S_{23}^2}(\sigma_{23}^2 - \sigma_{22}\sigma_{33}) + \left(\frac{\sigma_{12}}{S_{12}}\right)^2 + \left(\frac{\sigma_{13}}{S_{13}}\right)^2 \geq 1 \tag{3.4}$$

In some formulations,a weighting factor α is used to adjust the contribution of shear stress to fibre tension failure ($\sigma_{11} \geq 0$):

$$\left(\frac{\sigma_{11}}{X_T}\right)^2 + \alpha\left(\frac{\sigma_{12}}{S_{12}}\right)^2 + \alpha\left(\frac{\sigma_{13}}{S_{13}}\right)^2 \geq 1 \tag{3.5}$$

where σ_{11} refers to the normal stress in the fibre direction, σ_{22} to the normal stress in the transverse matrix direction, and σ_{33} to the normal stress through the laminate thickness. The shear stress components acting in the material planes are represented by σ_{12}, σ_{13} and σ_{23}. The symbols X_T and X_C represent the tensile (T) and compressive (C) strengths in fibre direction, whereas Y_T and Y_C define the corresponding strengths in matrix direction. The shear strengths are identified by S_{12}, S_{13} and S_{23}.

The adaptation of the criterion to 2D involves a simplification of the previous set of equations by removing the effect of the stresses acting in the third direction, i.e. in the thickness of the lamina, $\sigma_{13} = \sigma_{23} = \sigma_{33} = 0$. Therefore, the following equations present the modifications implemented.

Fibre failure in tension ($\sigma_{11} \geq 0$)

$$\left(\frac{\sigma_{11}}{X_T}\right)^2 + \left(\frac{\sigma_{12}}{S_{12}}\right)^2 \geq 1. \tag{3.6}$$

Fibre failure in compression ($\sigma_{11} < 0$)

$$\left(\frac{\sigma_{11}}{X_C}\right)^2 \geq 1. \tag{3.7}$$

Matrix failure in tension ($\sigma_{22} \geq 0$)

$$\left(\frac{\sigma_{22}}{Y_T}\right)^2 + \left(\frac{\sigma_{12}}{S_{12}}\right)^2 \geq 1, \tag{3.8}$$

Matrix failure in compression ($\sigma_{22} < 0$)

$$\left(\frac{\sigma_{22}}{2S_{23}}\right)^2 + \left[\left(\frac{Y_C}{2S_{23}}\right)^2 - 1\right]\frac{\sigma_{22}}{Y_C} + \left(\frac{\sigma_{12}}{S_{12}}\right)^2 \geq 1. \tag{3.9}$$

If desired, and, as mentioned before, the shear terms can also be scaled using an α parameter.

$$\left(\frac{\sigma_{11}}{X_T}\right)^2 + \alpha\left(\frac{\sigma_{12}}{S_{12}}\right)^2 \geq 1. \tag{3.10}$$

The two-dimensional form is computationally efficient and is commonly used with shell or continuum-shell elements. However, because it neglects the through-thickness stress components, it is most appropriate when the laminate response is dominated by in-plane stresses and when delamination is treated separately through cohesive or contact-based formulations.

3.1.1 Hashin Criterion - Damage Evolution Law

The preceding section delineated the criteria that determine the occurrence of damage and the circumstances in which it arises, according to the Hashin criterion. In the event of damage, it

is imperative to delineate the manner in which the damage evolves and the characteristics of the material that are affected by it.

In the context of composite materials, various methodologies are employed, which are based on the principles of *Continuum Damage Mechanics* (CDM). The development of the CDM has been undertaken for the purpose of modelling the evolution of damage. In this study, the damage evolution law that accompanies the Hashin criterion (2D and 3D) is based on the fracture energy dissipated during damage. The extent of the damage is dictated by a set of variables, d, which are associated with the various failure modes. These are calculated with the introduction of equivalent displacements δ_{eq}. Furthermore, δ_{eq} is determined by the equivalent stresses, σ_{eq}, and the fracture energies, G_{c}, of the composite material in question. In consideration of the effect of damage on the material, it is to be expected that the material's stiffness properties will undergo degradation [81, 82].

The damage evolution law associated with the 3D Hashin criterion is presented below. For each failure mode i, the damage variable d_i is determined from the corresponding equivalent displacement $\delta_{i,\text{eq}}$.

$$d_i = \frac{\delta^{\text{f}}_{i,\text{eq}}(\delta_{i,\text{eq}} - \delta^{0}_{i,\text{eq}})}{\delta_{i,\text{eq}}(\delta^{\text{f}}_{i,\text{eq}} - \delta^{0}_{i,\text{eq}})} \tag{3.11}$$

where the subscript i can be substituted by ft (fibre tension), fc (fibre compression), mt (matrix tension) or mc (matrix compression). The superscript f is used to denote the final equivalent displacement, while the superscript 0 indicates the equivalent displacement at the beginning of damage. The absence of any superscript ($\delta_{i,\text{eq}}$) is indicative of the current equivalent displacement. It is imperative to note that the formulation under consideration in Equation 3.11 guarantees that the damage variable commences at zero and ascends in a consistent manner to one as failure progresses. Figure 3.1 illustrates the evolution of d according to the equivalent displacements.

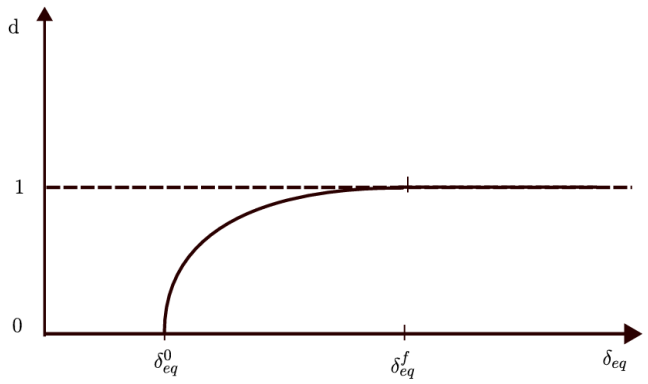


Figure 3.1: Damage parameter d evolution as a function of the equivalent displacement $\delta_{i,\text{eq}}$.

Turning to the variables involved in the d computation, the following Equations 3.12 to 3.15 introduce the calculation of the current equivalent displacements.

$$\delta_{\text{ft,eq}} = L_{\text{e}}\sqrt{\langle\varepsilon_{11}^2\rangle + \varepsilon_{12}^2 + \varepsilon_{13}^2} \tag{3.12}$$

$$\delta_{\text{fc,eq}} = L_{\text{e}}\langle-\varepsilon_{11}\rangle \tag{3.13}$$

$$\delta_{\text{mt,eq}} = L_{\text{e}}\sqrt{\langle\varepsilon_{22}^2\rangle + \langle\varepsilon_{33}^2\rangle + \varepsilon_{12}^2 + \varepsilon_{23}^2 + \varepsilon_{13}^2} \tag{3.14}$$

$$\delta_{\text{mc,eq}} = L_{\text{e}}\sqrt{\langle-\varepsilon_{22}^2\rangle + \langle-\varepsilon_{33}^2\rangle + \varepsilon_{12}^2 + \varepsilon_{23}^2 + \varepsilon_{13}^2} \tag{3.15}$$

where L_{e} is representative of a characteristic length, that will be presented later in Section 4.2.7.1, whilst ε_{xy} is indicative of the different strain components. $\langle\rangle$ is the Macaulay operator, defined as:

$$\langle x\rangle = \frac{x+|x|}{2}, \forall x \in \mathbb{R} \tag{3.16}$$

Once δ_{eq} has been determined, the equivalent stresses, σ_{eq}, can be calculated, by the set of Equations 3.17 to 3.20.

$$\sigma_{\text{ft,eq}} = \frac{L_{\text{e}}(\langle\sigma_{11}\rangle\langle\varepsilon_{11}\rangle + \sigma_{12}\varepsilon_{12} + \sigma_{13}\varepsilon_{13})}{\delta_{\text{eq}}^{\text{ft}}} \tag{3.17}$$

$$\sigma_{\text{fc,eq}} = \frac{L_{\text{e}}\langle-\sigma_{11}\rangle\langle-\varepsilon_{11}\rangle}{\delta_{\text{eq}}^{\text{fc}}} \tag{3.18}$$

$$\sigma_{\text{mt,eq}} = \frac{L_{\text{e}}(\langle\sigma_{22}\rangle\langle\varepsilon_{22}\rangle + \langle\sigma_{33}\rangle\langle\varepsilon_{33}\rangle + \sigma_{12}\varepsilon_{12} + \sigma_{23}\varepsilon_{23} + \sigma_{13}\varepsilon_{13})}{\delta_{\text{eq}}^{\text{mt}}} \tag{3.19}$$

$$\sigma_{\text{mc,eq}} = \frac{L_{\text{e}}(\langle-\sigma_{22}\rangle\langle-\varepsilon_{22}\rangle + \langle-\sigma_{33}\rangle\langle-\varepsilon_{33}\rangle + \sigma_{12}\varepsilon_{12} + \sigma_{23}\varepsilon_{23} + \sigma_{13}\varepsilon_{13})}{\delta_{\text{eq}}^{\text{mc}}} \tag{3.20}$$

For a failure index that is homogeneous and quadratic in stress, the equivalent displacement at damage initiation can be estimated under proportional elastic loading using Equation 3.21, with the material properties held fixed during this scaling.

$$\delta_{i,\text{eq}}^{0} = \frac{\delta_{i,\text{eq}}}{\sqrt{F_i}} \tag{3.21}$$

where F_i is the dimensionless damage-initiation index for the corresponding failure mode. It is calculated by substituting the local stress components and material strengths into the left-hand side of the relevant Hashin criterion in Equations 3.1-3.4. For example, fibre compression gives $F_{\text{fc}} = (\sigma_{11}/X_{\text{C}})^2$. Each mode is evaluated separately: values below unity indicate that its initiation threshold has not been reached, while the first attainment of $F_i \geq 1$ marks damage initiation.

The normalisation in Equation 3.21 applies to homogeneous quadratic criteria under proportional elastic loading. For matrix compression, which includes a linear stress term, the initiation point must instead be determined from the complete criterion.

The final step in this process is to present the calculation of $\delta^{\mathrm{f}}_{i,\mathrm{eq}}$. In order to accomplish this, the fracture energy of the respective failure mode, $G_{i,\mathrm{c}}$ and the equivalent stress at the onset of damage, $\sigma^{0}_{i,\mathrm{eq}}$ are utilised, as presented in Equation 3.22. In order to facilitate a more profound comprehension of the relationship, Figure 3.2 is hereby presented. The fracture energy, $G_{i,\mathrm{c}}$ (illustrated by the shaded area of the triangle), pertains to the energy that the material will absorb during the various failure modes. It is evident that, up to $\sigma^{0}_{i,\mathrm{eq}}$, the material is operating within the linear elastic regime. It has been demonstrated that elevated levels of stress result in the material undergoing a transition to a linear softening phase, a phenomenon that has been observed to occur subsequent to the occurrence of damage [81].

$$\delta^{\mathrm{f}}_{i,\mathrm{eq}} = \frac{2G_{i,\mathrm{c}}}{\sigma^{0}_{i,\mathrm{eq}}} \tag{3.22}$$

Regarding $\sigma^{0}_{i,\mathrm{eq}}$ its calculation philosophy is similar to that of $\delta^{0}_{i,\mathrm{eq}}$:

$$\sigma^{0}_{i,\mathrm{eq}} = \frac{\sigma_{i,\mathrm{eq}}}{\sqrt{F_i}} \tag{3.23}$$

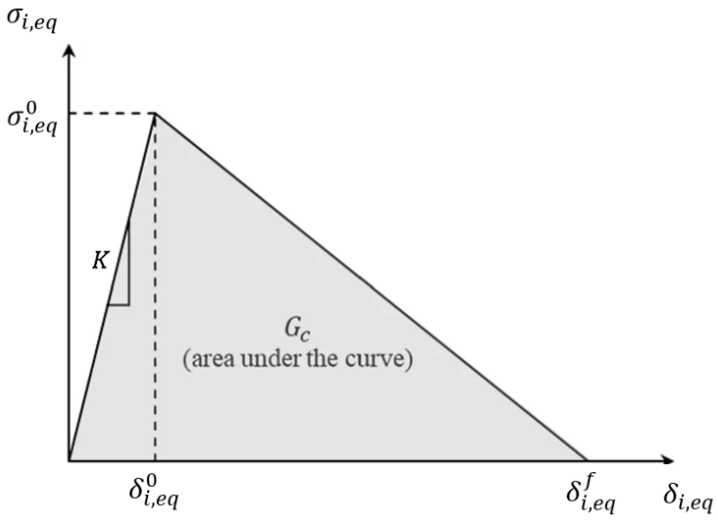


Figure 3.2: Linear elastic and linear softening regime (Adapted from [83]).

Following a comprehensive elucidation of the calculation of d, it is imperative to delineate the manner in which it influences the material response. Equation 3.24 presents the expression employed to calculate the stress state. In this equation, σ denotes the stress tensor, $\mathbf{C}$ represents the elasticity matrix and ε is the strain tensor. Consequently, in the event of damage, the variable d_i will be non-zero, affecting the components of the elasticity matrix $\mathbf{C}$. This will be referred to

as the damaged elasticity matrix, denoted by $\mathbf{C}_\mathrm{d}$. The calculation of this matrix is outlined in Equations 3.25 and 3.26.

$$\sigma = \mathbf{C}\varepsilon \tag{3.24}$$

$$\mathbf{C}_\mathrm{d} = \frac{1}{D}\begin{bmatrix} C_{11} & C_{12} & C_{13} & 0 & 0 & 0 \\ C_{21} & C_{22} & C_{23} & 0 & 0 & 0 \\ C_{31} & C_{32} & C_{33} & 0 & 0 & 0 \\ 0 & 0 & 0 & C_{44} & 0 & 0 \\ 0 & 0 & 0 & 0 & C_{55} & 0 \\ 0 & 0 & 0 & 0 & 0 & C_{66} \end{bmatrix} \tag{3.25}$$

with,

$$\begin{aligned} C_{11} &= d_\mathrm{f} E_{11}(1 - d_\mathrm{m}\nu_{23}\nu_{32}) \\ C_{22} &= d_\mathrm{m} E_{22}(1 - d_\mathrm{f}\nu_{13}\nu_{31}) \\ C_{33} &= E_{33}(1 - d_\mathrm{f} d_\mathrm{m}\nu_{12}\nu_{21}) \\ C_{12} &= C_{21} = d_\mathrm{f} d_\mathrm{m} E_{11}(\nu_{21} + \nu_{23}\nu_{31}) \\ C_{13} &= C_{31} = d_\mathrm{f} E_{11}(\nu_{31} + d_\mathrm{m}\nu_{21}\nu_{32}) \\ C_{23} &= C_{32} = d_\mathrm{m} E_{22}(\nu_{32} + d_\mathrm{f}\nu_{12}\nu_{31}) \\ C_{44} &= D d_\mathrm{f} d_\mathrm{m} G_{12} \\ C_{55} &= D d_\mathrm{f} d_\mathrm{m} G_{23} \\ C_{66} &= D d_\mathrm{f} d_\mathrm{m} G_{13} \\ d_\mathrm{f} &= (1 - d_\mathrm{ft})(1 - d_\mathrm{fc}) \\ d_\mathrm{m} &= (1 - S_\mathrm{mt} d_\mathrm{mt})(1 - S_\mathrm{mc} d_\mathrm{mc}) \\ D &= 1 - d_\mathrm{f} d_\mathrm{m}\nu_{12}\nu_{21} - d_\mathrm{m}\nu_{23}\nu_{32} - d_\mathrm{f}\nu_{13}\nu_{31} - 2 d_\mathrm{f} d_\mathrm{m}\nu_{21}\nu_{32}\nu_{13} \end{aligned} \tag{3.26}$$

where E_{ii} ($i = 1,2$ or 3) represents the modulus of elasticity, G_{ij} ($i, j = 1,2,3$ with $i \neq j$) is the shear modulus and ν_{ij} ($i, j = 1,2,3$ with $i \neq j$) is the Poisson's ratio. S_mt and S_mc are coefficients for control of shear stiffness loss, under matrix tension and compression.

Subsequently, a detailed exposition of the simplifications is presented, with the objective of applying the damage degradation law to the 2D case. In essence, the alterations pertain to the calculation of $\delta_{i,\mathrm{eq}}$ (Equation 3.27 to 3.30), $\sigma_{i,\mathrm{eq}}$ (Equation 3.31 to 3.34) and C_d (Equation 3.35 and 3.36).

$$\delta_{\mathrm{ft,eq}} = L_\mathrm{e}\sqrt{\langle\varepsilon_{11}^2\rangle + \varepsilon_{12}^2} \tag{3.27}$$

$$\delta_{\mathrm{fc,eq}}^{\mathrm{fc}} = L_\mathrm{e}\langle -\varepsilon_{11}\rangle \tag{3.28}$$

$$\delta_{\mathrm{mt,eq}} = L_{\mathrm{e}}\sqrt{\langle\varepsilon_{22}^2\rangle + \varepsilon_{12}^2} \tag{3.29}$$

$$\delta_{\mathrm{mc,eq}} = L_{\mathrm{e}}\sqrt{\langle-\varepsilon_{22}^2\rangle + \varepsilon_{12}^2} \tag{3.30}$$

$$\sigma_{\mathrm{ft,eq}} = \frac{L_{\mathrm{e}}(\langle\sigma_{11}\rangle\langle\varepsilon_{11}\rangle + \sigma_{12}\varepsilon_{12})}{\delta_{\mathrm{eq}}^{\mathrm{ft}}} \tag{3.31}$$

$$\sigma_{\mathrm{fc,eq}} = \frac{L_{\mathrm{e}}\langle-\sigma_{11}\rangle\langle-\varepsilon_{11}\rangle}{\delta_{\mathrm{eq}}^{\mathrm{fc}}} \tag{3.32}$$

$$\sigma_{\mathrm{mt,eq}} = \frac{L_{\mathrm{e}}(\langle\sigma_{22}\rangle\langle\varepsilon_{22}\rangle + \sigma_{12}\varepsilon_{12})}{\delta_{\mathrm{eq}}^{\mathrm{mt}}} \tag{3.33}$$

$$\sigma_{\mathrm{mc,eq}} = \frac{L_{\mathrm{e}}(\langle-\sigma_{22}\rangle\langle-\varepsilon_{22}\rangle + \sigma_{12}\varepsilon_{12})}{\delta_{\mathrm{eq}}^{\mathrm{mc}}} \tag{3.34}$$

$$C_{\mathrm{d}} = \frac{1}{D}\begin{bmatrix} C_{11} & C_{12} & 0 \\ C_{21} & C_{22} & 0 \\ 0 & 0 & C_{66} \end{bmatrix} \tag{3.35}$$

with,

$$\begin{aligned} C_{11} &= d_{\mathrm{f}}E_{11} \\ C_{22} &= d_{\mathrm{m}}E_{22} \\ C_{66} &= d_{\mathrm{s}}G_{12}D \\ C_{12} &= C_{21} = d_{\mathrm{f}}d_{\mathrm{m}}E_{11}\nu_{21} \\ d_{\mathrm{f}} &= (1-d_{\mathrm{ft}})(1-d_{\mathrm{fc}}) \\ d_{\mathrm{m}} &= (1-d_{\mathrm{mt}})(1-d_{\mathrm{mc}}) \\ d_{\mathrm{s}} &= 1-d_{\mathrm{f}}d_{\mathrm{m}} \\ D &= 1-d_{\mathrm{f}}d_{\mathrm{m}}\nu_{12}\nu_{21} \end{aligned} \tag{3.36}$$

Note that, in this case, a new variable, d_{s}, is introduced responsible for quantifying shear damage.

3.2 Strain Rate Effect on Polymer Matrix Composites

In impact simulations, the strain rate dependence, $\dot{\varepsilon}$, of composite stiffness, strength and fracture toughness is accounted for exclusively in the 3D Hashin model. Following the methodology proposed by Millen et al. [84], selected material properties are adjusted using strain rate dependent scale factor β, whose values are defined according to three loading regimes:

- Quasi-static (QS), if $\dot{\varepsilon} \leq 0.1\ s^{-1}$;
- Intermediate rate (IR), if $0.1 < \dot{\varepsilon} < 100\ (s^{-1})$;
- High rate (HR), if $\dot{\varepsilon} \geq 100\ s^{-1}$.

In the context of the QS regime, no influence is noted. For IR regime a linear adjustment of the scale factor is made. Finally, in the HR case, it is imperative to employ the maximum value of the scale factor. The various conditions delineated are mathematically represented in Equation 3.37 [84].

$$\beta = \begin{cases} 1.0, \text{ for QS} \\ \frac{(\dot{\varepsilon}-0.1)(\beta_{max}-1)}{100-0.1} + 1, \text{ for IR} \\ \beta_{max}, \text{ for HR} \end{cases} \tag{3.37}$$

Subsequent to the presentation of the regimes and conditions, the maximum values of the scaling factors for the various properties affected must be presented. It is important to note that only the in-plane and out-of-plane transverse stiffness is affected, E_{22} and E_{33}, respectively. This is due to the fact that, in the case of unidirectional composites, it is assumed that the stiffness in the fibre direction, E_{11}, is defined entirely by the properties of the fibre and is insensitive to the strain rate. The same philosophy of thought applies to fracture energies, with the result that only those relating to the matrix are affected [84].

It is noteworthy that the composite under investigation in the present study differs from the composite examined in [84]. Consequently, the maximum scaling factors were calibrated through a series of simulations of the composite target. The values reported in [84] were utilised as preliminary estimates, with each factor being varied in order to assess its influence on the numerical response. The final values, presented in Table 3.1, correspond to those that exhibited the closest agreement with the experimental results.

Table 3.1: Calibrated maximum strain rate scaling factors (Adapted from [84]).

Property	$E_{22} = E_{33}$	X_C	X_T	Y_C	Y_T	$G_{mc,c}$	$G_{mt,c}$
β_{max}	1.29	1.39	1.38	1.37	1.38	1.63	1.42

3.3 Johnson-Cook Model

The J-C model [85, 86] is frequently employed to describe the behaviour of mettalic materials under large strains, high strain rates, and elevated temperatures. These models are utilized to analyze and predict the response of materials to dynamic loads. The J-C model incorporates the hardening behaviour and strain rate effects of the material under dynamic loads. The model's structure is straightforward, and the parameters are relatively straightforward to determine. Consequently, it is extensively utilised to simulate impacts, explosions, and associated problems.

The J-C model decomposes the equivalent stress into three functions that depend on the strain, strain rate and temperature degrees and is specified by the constitutive relations presented in Equation 3.38.

$$\sigma_{\text{y, eq}} = [A + B(\bar{\varepsilon}^p)^n] \left[1 + C \ln \left(\frac{\dot{\bar{\varepsilon}}^p}{\dot{\bar{\varepsilon}}_0}\right)\right] (1 - T^{*m}) \tag{3.38}$$

where $\sigma_{\text{y, eq}}$ is the equivalent stress, A, B and n are the static yield stress, the strain strengthening coefficient and the strain strengthening index, respectively. These three parameters can be determined by fitting the plastic section of the static tensile curves. C is the strain rate sensitivity, m is the temperature softening coefficient, $\bar{\varepsilon}^p$ is the equivalent plastic strain, $\dot{\bar{\varepsilon}}^p$ is the equivalent plastic strain rate, $\dot{\bar{\varepsilon}}_0$ is the reference plastic strain rate, which normally takes the value of 1.0 s^{-1}. Finally, the non-dimensional homologous temperature, T^*, is defined in Equation 3.39.

$$T^* = \frac{T - T_{\text{r}}}{T_{\text{m}} - T_{\text{r}}} \tag{3.39}$$

where T is the material temperature, T_{r} is the room temperature and T_{m} is the melting point of the material.

In the Johnson-Cook model, the linear accumulation is utilized to consider the failure behaviour in the material deformation history. This involves more than just the change of failure strain with stress state, strain rate and temperature. It also reflects the accumulation of failure during the deformation process. The plastic failure strain, ε_{f}, is expressed by the stress state, strain rate and temperature as follows,

$$\varepsilon_{\text{f}} = [D_1 + D_2 \exp(D_3 \sigma^*)] \left[1 + D_4 \ln \left(\frac{\dot{\bar{\varepsilon}}^p}{\dot{\bar{\varepsilon}}_0}\right)\right] [1 + D_5 T^*] \tag{3.40}$$

In this context, D_1 through D_5 are the failure parameters measured by experimental data and σ^* is the mean stress normalized by the equivalent stress.

The parameter D is a damage accumulation value and is calculated in Equation 3.41,

$$D = \sum \left(\frac{\Delta \bar{\varepsilon}^p}{\varepsilon_{\text{f}}}\right) \tag{3.41}$$

where $\Delta\bar{\varepsilon}^{\text{p}}$ is equivalent plastic strain increment, and ε_{f} is equivalent strain to fracture under the existing parameters of stress, temperature, and strain rate. In the context of fracture, the material strength undergoes a decline during the process of distortion. The constitutive connection of stress for damage growth can be expressed as follows,

$$\sigma_D = (1 - D)\sigma_{\text{y, eq}} \tag{3.42}$$

As demonstrated above, σ_D denotes the equivalent stress after damage-induced degradation, $\sigma_{\text{y, eq}}$ is the equivalent stress and D, as mentioned above, signifies the damage parameter ($0 \leq D < 1$). Furthermore, it is possible to calculate stress triaxiality and equivalent stress from the uncracked material by observing the plastic behaviour up to the formation of the necking.

The utilization of ballistic materials is a strategic measure employed to mitigate substantial deformations in both architectural structures and automotive vehicles. It is evident that, under conditions of elevated strain rates, materials undergo plastic deformation, accompanied by an escalation in temperature. Consequently, the material exhibits a propensity for fracture upon the impact of the blast wave with the structural element. The significance of Johnson-Cook model lies in its incorporation of temperature effects, strain rate, and hardening, elements that are crucial in understanding the dynamics of material behaviour [87]. In explicit finite element simulations, this damage variable can be coupled with element deletion to reproduce ductile perforation and plugging of metallic layers.

3.4 Interlaminar Failure Model

Interlaminar failure, otherwise known as delamination, is one of the failure mechanisms associated with composite laminates. In this study, the phenomenon under investigation will be introduced by means of cohesive elements, which describe both the initiation and propagation phases of interlaminar failure.

In order to provide a description of the behaviour exhibited by this particular type of failure, the research undertaken by Camanho and Dávila [88] was utilized. The occurrence of delaminations under mix mode loading is, according to the authors, a fairly common phenomenon. This is illustrated in Figure 3.3, which shows a combination of Mode I (opening), II (sliding) and III (tearing). Accordingly, the initiation of this type of damage is given by the Equation 3.43.

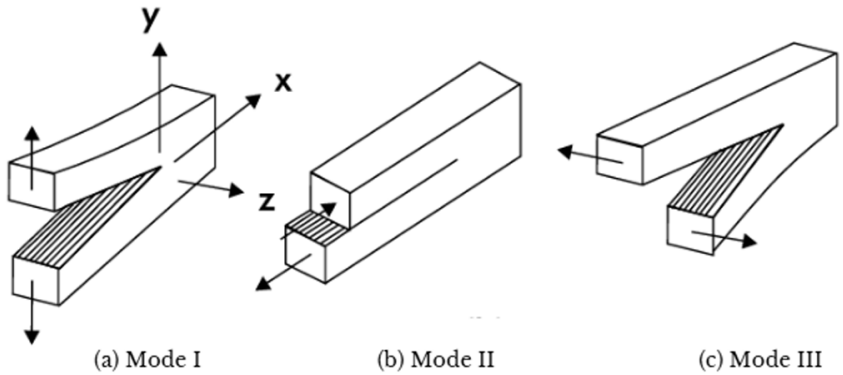


Figure 3.3: Fracture crack separation modes [89].

$$\left(\frac{\langle t_n \rangle}{t_n^{max}}\right)^2 + \left(\frac{t_s}{t_s^{max}}\right)^2 + \left(\frac{t_t}{t_t^{max}}\right)^2 = 1 \tag{3.43}$$

where t_n, t_s and t_t are the normal and shear action traction forces. The maximum admissible values of these forces are indicated by t_n^{max}, t_s^{max} and t_t^{max}.

Before damage initiation, the acting tractions are related to the separation displacements through the linear elastic relationship defined in Equation 3.44.

$$\begin{bmatrix} t_n \\ t_s \\ t_t \end{bmatrix} = \begin{bmatrix} K_n & 0 & 0 \\ 0 & K_s & 0 \\ 0 & 0 & K_t \end{bmatrix} \begin{bmatrix} \delta_n \\ \delta_s \\ \delta_t \end{bmatrix} \tag{3.44}$$

where K_n, K_s, and K_t are the normal and shear penalty stiffnesses, respectively, and δ_n, δ_s, δ_t concern the relative displacements across the interface.

3.4.1 Interlaminar Failure Model - Damage Evolution Law

Following the initiation of the damage process, the subsequent damage evolution must be introduced. In this particular instance, the basis is fracture energy and the evolution is linear (Figure 3.4). The damage parameter, d, that quantifies the amount of damage is measured through the calculation of effective displacements, as delineated in Equation 3.45 [88].

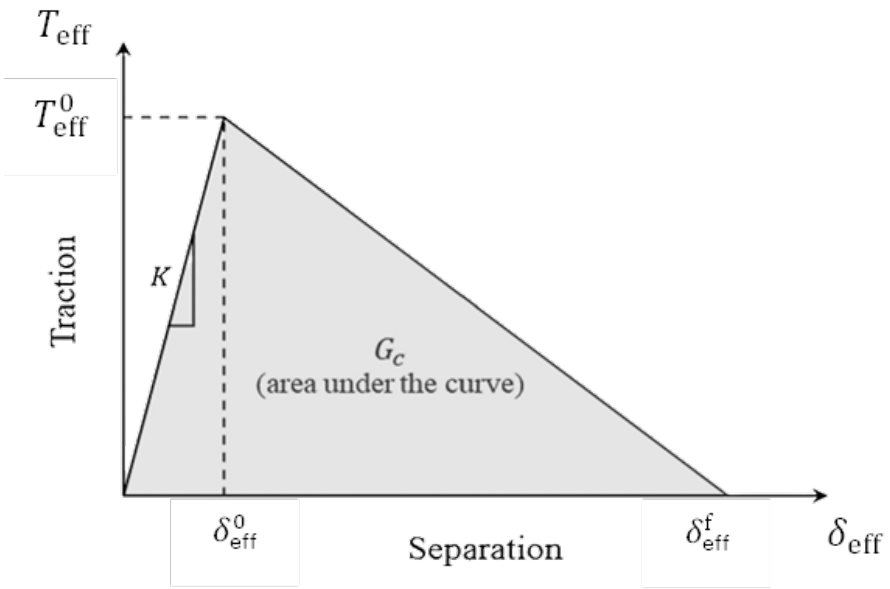


Figure 3.4: The bilinear traction-separation law in cohesive zone model for the coesive elements (Adapted from [83]).

$$d = \frac{\delta^f_{eff}(\delta^{max}_{eff} - \delta^0_{eff})}{\delta^{max}_{eff}(\delta^f_{eff} - \delta^0_{eff})} \tag{3.45}$$

where the variable δ^0_{eff} denotes the effective displacement at the onset of damage, δ^{max}_{eff} is the peak value reached throughout the loading history, and δ^f_{eff} corresponds to the displacement at complete failure. The effective displacement and the displacement at complete failure are given by Equations 3.46 and 3.47, respectively.

$$\delta_{eff} = \sqrt{\langle \delta_n \rangle^2 + \delta_s^2 + \delta_t^2} \tag{3.46}$$

$$\delta_{\text{eff}}^{\text{f}} = \frac{2G_{\text{c}}}{T_{\text{eff}}^{0}} \tag{3.47}$$

where G_{c} is the fracture energy and T_{eff}^{0} is the effective traction at damage initiation, denoted by Equation 3.48.

$$T_{\text{eff}}^{0} = K \cdot \delta_{\text{eff}}^{0} \tag{3.48}$$

In order to take into account the influence of the loading mode on fracture toughness, a mode-dependent energy interaction law is applied. There are two widely utilised approaches: the power law criterion and the Benzeggagh–Kenane criterion, which is also referred to as the B-K criterion.

The power law criterion expresses the interaction between Modes I, II and III fracture energies as,

$$\left(\frac{G_{\text{I}}}{G_{\text{Ic}}}\right)^{\alpha} + \left(\frac{G_{\text{II}}}{G_{\text{IIc}}}\right)^{\alpha} + \left(\frac{G_{\text{III}}}{G_{\text{IIIc}}}\right)^{\alpha} = 1 \tag{3.49}$$

where G_{Ic}, G_{IIc} and G_{IIIc} denote the critical fracture energies associated with Modes I, II and III, respectively, and α is an experimentally determined material parameter.

Alternatively, the B-K criterion provides a more accurate representation of fracture in composite materials, particularly when all three fracture modes are involved, as it describes damage evolution under mixed-mode loading. The criterion is defined by Equation 3.50.

$$G_{\text{c}} = G_{\text{Ic}} + (G_{\text{IIc}} - G_{\text{Ic}}) \left(\frac{G_{\text{shear}}}{G_{\text{T}}}\right)^{\eta} \tag{3.50}$$

where η is an experimentally determined material parameter. The total and shear energy release rates are defined by Equation 3.51.

$$G_{\text{T}} = G_{\text{I}} + G_{\text{II}} + G_{\text{III}}, \qquad G_{\text{shear}} = G_{\text{II}} + G_{\text{III}} \tag{3.51}$$

This formulation is well suited to impact simulations because delamination usually develops under mixed-mode loading rather than pure opening or pure shear.

In order to ascertain the point at which complete decohesion transpires, the critical relative displacement, $\delta_{\text{m}}^{\text{f}}$, is calculated by equating the energy release rate to G_{c}. In order to satisfy the power law criterion,

$$\delta_{\text{m}}^{\text{f}} = \begin{cases} \sqrt{\frac{2(1+\beta^2)}{K\delta_{\text{m}}^{0}} \left(\left(\frac{1}{G_{\text{Ic}}}\right)^{\alpha} + \left(\frac{\beta^2}{G_{\text{IIc}}}\right)^{\alpha} \right)^{-1/\alpha}} & \text{if } \delta_3 > 0 \\ \sqrt{(\delta_1^{\text{f}})^2 + (\delta_2^{\text{f}})^2} & \text{if } \delta_3 \leq 0 \end{cases} \tag{3.52}$$

For the B-K criterion,

$$\delta_{\mathrm{m}}^{\mathrm{f}} = \begin{cases} \sqrt{\frac{2}{K\delta_{\mathrm{m}}^{0}}\left[G_{\mathrm{Ic}} + (G_{\mathrm{IIc}} - G_{\mathrm{Ic}})\left(\frac{\beta^2}{1+\beta^2}\right)^{\eta}\right]} & \text{if } \delta_3 > 0 \\ \sqrt{(\delta_1^{\mathrm{f}})^2 + (\delta_2^{\mathrm{f}})^2} & \text{if } \delta_3 \leq 0 \end{cases} \tag{3.53}$$

where β is the mode mixity ratio and is defined by Equation 3.54.

$$\beta = \frac{\delta_{\mathrm{shear}}}{\delta_3} = \frac{\sqrt{\delta_1^2 + \delta_2^2}}{\delta_3} \tag{3.54}$$

Notwithstanding the criterion employed, pure mode loading constitutes a specific instance of the proposed formulation, whereby $\delta_{\mathrm{m}}^{\mathrm{f}} = \delta_3^{\mathrm{f}}$ for $\beta = 0$ (Mode I) and $\delta_{\mathrm{m}}^{\mathrm{f}} = \delta_{\mathrm{shear}}^{\mathrm{f}}$ for $\delta_3^{\mathrm{f}} = 0$ (or when $\beta \to \infty$) corresponding to shear-dominated delamination.

The cohesive zone model utilized in this study offers a physically consistent framework for simulating delamination under both quasi-static and dynamic loading conditions. This is achieved by combining a rigorous initiation criterion with an energy-based evolution law.

3.5 Numerical Implementation of Failure Criteria

The purpose of this subsection is to describe the implementation of the previously presented failure and damage models within the Abaqus/Explicit finite element framework. These models were employed to represent the failure behaviour of both composite and metallic domains, utilising either the software's native built-in capabilities or user-defined subroutines when more advanced formulations were required. It is evident that the 2D Hashin criterion and the interlaminar failure model, based on cohesive zone elements, are natively available in the base version of the Abaqus material library [90]. Consequently, these criteria and their corresponding degradation laws were activated and configured directly through the Graphical User Interface (GUI), requiring no custom coding beyond a full understanding of the online manual's formulations.

Conversely, the 3D version of the Hashin criterion, which is necessary to capture out-of-plane stress effects in thick composite domains is not natively present in the Abaqus library. In order to address this limitation, the models were introduced into the explicit dynamic environment by means of Vectorized User Material subroutine (VUMAT) subroutines programmed in Fortran. The implementation of the 3D Hashin criterion was contingent upon the preceding research contributions of Miranda [91]. It is evident that Miranda's original model incorporated a number of key elements that were central to the simulation of crashworthiness. These elements included orthotropic elasticity, Hashin-based intralaminar failure, strain rate effects and progressive stiffness degradation.

In addition, the J-C model was employed to represent the viscoplastic response and progressive failure of the metallic components subjected to the large strains, high strain rates and temperature

variations associated with projectile-target interaction. This constitutive model is natively available in Abaqus/Explicit and can be fully defined through the GUI by introducing the required elastic, plastic, strain rate, thermal-softening and damage parameters in the material definition.

As illustrated in Table 3.2, a comprehensive overview of the various implementation options for each failure model in Abaqus/Explicit is provided, along with their respective method of access or integration. This underscores the utilisation of both built-in capabilities and user-defined routines to ensure that all essential material behaviours are incorporated within the numerical framework developed.

Table 3.2: Access to material models

Failure Model	Availability in Abaqus	Implementation Method
Hashin 2D	Available	GUI
Hashin 3D	Not available	VUMAT
Interlaminar Damage	Available	GUI
Johnson-Cook	Available	GUI

A significant numerical issue that has been identified is that of mesh dependency. In the absence of fracture-energy regularisation, the phenomenon of stiffness degradation or element deletion may occur. Consequently, the dissipated energy may decrease as the mesh is refined. Therefore, the evolution of damage should be associated with the characteristic length of the element (Section 4.2.7.1) or the cohesive fracture energy. In ballistic impact simulations, stable contact, sufficiently small time increments, and carefully selected output variables are also required to avoid non-physical penetration, artificial energy growth, or premature failure.

3.6 Previous Work Developed at FEUP

This sub-chapter reviews relevant research previously conducted at the Faculty of Engineering of the University of Porto (FEUP) within the scope of composite materials, impact simulations, and aerospace structures. Specifically, it summarizes the contributions of three recent Master's dissertations in Mechanical Engineering, all developed under the supervision of Professor Volnei Tita. Together, these studies provide a foundational background for the methodologies and analyses developed in this thesis.

Mário Miranda (2023) [92] focused on simulating the crashworthiness of composite fuselage components for civil transportation aircraft. His main contribution was improving the accuracy of damage prediction in virtual simulations by developing advanced numerical models for intra- and interlaminar damage evolution, implemented in the Abaqus software via VUMAT subroutines. By employing Hashin and Puck failure criteria, alongside a strain rate dependent criterion, the author validated his methodology through low-velocity impact and Open Hole Tensile tests. The study

concluded that the proposed virtual testing approach provided higher fidelity results regarding the crash behaviour of fuselage elements when compared to simplified models previously used.

Building upon advanced numerical modelling, André Rocha (2024) [93] investigated material models capable of simulating the behaviour of hybrid laminates under ballistic impact for the protection of military aircraft, taking strain rate effects into account. Through explicit dynamic simulations in Abaqus, the study progressed from evaluating 2D and 3D criteria in low-velocity impacts to simulating high-velocity impacts on unidirectional composites, woven fabrics, and ceramic plates. The work's key contribution was demonstrating that the hybridization of protective structures, particularly combining ceramic front plates (modelled with the Johnson-Holmquist criteria) with composite backing layers, significantly increases the structure's overall energy absorption capacity.

Delving deeper into this specific theme, Catarina Silva (2025) [94] focused on the design and analysis of hybrid composite shields for military aircraft. Her research evaluated the behaviour of targets composed of an alumina strike face and a composite laminate backing under high-velocity impacts (400 m/s and 600 m/s). The study utilised the Johnson-Holmquist II model to simulate the ceramic's behaviour and a three-dimensional Hashin criterion implemented in a VUMAT for the intralaminar response. Her main contribution was a direct comparison between the arrest mechanisms of CFRP and UHMWPE laminates. The author concluded that UHMWPE provides significantly superior energy dissipation and stopping capability at high velocities compared to CFRP, albeit at the expense of a larger rear face deflection.

Chapter 4

Case Study on High-Velocity Ballistic Impacts

The present chapter is devoted to an examination of high-velocity impacts, otherwise referred to as ballistic impacts. The ultimate objective is to develop an accurate model of the behaviour of a hybrid laminate subjected to a high-velocity impact, taking the strain rate into account.

A significant proportion of research conducted in the domain of hybrid armour, as evidenced by the extant literature, involves the integration of composite and metallic materials. In the field of composite materials, laminates composed of woven layers are employed at a significantly higher frequency than their UD counterparts. Although the 3D Hashin criterion was developed for UD composites, it is frequently employed by authors to determine the failure onset of laminates with woven layers [95–97]. However, some authors advocate for the adaptation or comprehensive development of models to enhance the depiction of the behaviour exhibited by such structures [98].

The present study focuses on UD composites and the effect of hybridising them by adding a metallic material. The objective of this study is to develop 3D models. To this end, the behaviour of the composite materials is described using only the 3D Hashin criterion. It should be noted that the deletion of elements was introduced in VUMAT at this stage. This phenomenon transpires when the damage parameter, d, attains a value greater than or equal to 0.99. This section introduces the J-C model, which is employed to describe the behaviour of the metallic material.

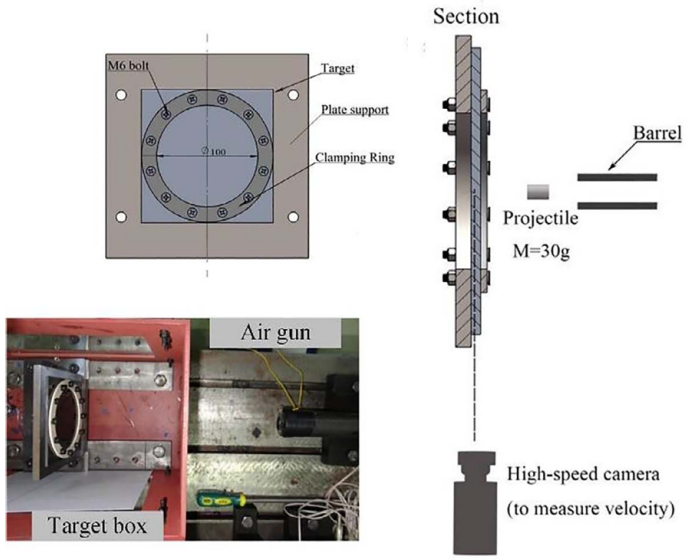
As was the case in the preceding section, the study of high-speed impacts is conducted in a gradual manner. Initially, the 3D Hashin criterion and its degradation law are validated. In the following section, the validation of the J-C model for metallic materials will be conducted. Subsequent to the validation of these two models individually, a study of plate hybridisation is conducted.

Prior to the presentation of the various case studies, it is essential to acknowledge a notable absence in the extant literature concerning the evolution of reaction force and transferred energy during the various impact stages of high-velocity impacts. Nevertheless, the primary parameters for comparison are frequently the final residual velocity of the projectile and/or the total energy

absorbed by the plate. Consequently, it becomes more complicated to ascertain whether the model correctly describes all phases of the high-speed impact event.

4.1 Experimental Setup

The experimental impact tests described in this section were conducted by Xu et al. [99] at ambient temperature, using an air gun adapted from a split Hopkinson pressure bar test platform. The apparatus was modified to ensure coaxial alignment between the gun barrel, projectile and target, thereby promoting impact normal to the specimen surface. As recorded by the high-speed photography, the projectile deflection angle remained below 5° throughout the experimental campaign. The air gun was constructed with a barrel measuring 2 m in length, with an internal diameter of 16 mm, and a pressure vessel with a maximum operating pressure of 20 MPa. The system was found to be capable of accelerating the 30 g steel projectile to velocities ranging from 80 to 350 m/s. The square target panels, measuring 130×130 mm, were affixed to the support using a steel clamping ring and twelve M6 bolts. The resulting circular exposed impact area measured 100 mm in diameter is presented in Figure 4.1. The specimen support plate was mounted on a steel containment box and positioned perpendicular to the gun barrel. The steel box was designed to support the test assembly and to collect fragments detached from the target during impact [99].



(a) Test platform. (b) Test layout.

Figure 4.1: Ballistic impact experimental setup [99].

The projectile velocity, impact conditions and maximum striking angle were recorded using a Phantom V710 high-speed camera system. The initial impact velocity, v_i, and the residual velocity, v_r, were calculated from the displacement of the projectile between successive frames according

to $v = \frac{\Delta d}{\Delta t}$, where Δd denote the projectile displacement between two frames and Δt denote the corresponding time interval. The images were obtained at a frame rate of 45,000 fps with a resolution of 550×300 pixels [99].

The projectiles were manufactured from 1045 steel and consisted of cylindrical bodies with flat, hemispherical or sharp nose geometries. All projectiles had a nominal diameter of 16 mm. Their lengths were adjusted slightly according to the nose geometry to maintain a constant mass of 30 g. The tests were designated F, H and S for the flat, hemispherical and sharp projectiles, respectively [99].

4.2 Model Construction and Setup

The numerical model was developed in Abaqus/Explicit following a structured procedure to ensure accuracy and reproducibility, given the strongly transient and highly nonlinear nature of ballistic impact. The complete model consists of a multilayer target plate and a rigid projectile, depending on the level of detail required for each case study. The target geometry reproduces the representative panel dimensions while maintaining a sufficiently large in-plane area to minimise edge effects during the short impact event. Furthermore, its thickness is discretised according to the laminate stacking sequence and any metallic front or backing layers included in the configuration. The modelling procedure is a multifaceted process that encompasses the definition of geometry, analysis steps, interactions and boundary conditions. The adoption of specific choices is guided by finite element best practices and extant literature on high-velocity ballistic impacts.

4.2.1 Part Definition and Model Geometry

In consideration of the high strain rates, contact nonlinearities, stress-wave propagation and progressive material degradation that are intrinsic to ballistic impact, a finite element model was developed using an explicit dynamic formulation in Abaqus/CAE. The model is a representation of a rigid projectile impacting a hybrid target composed of an aluminium front and back layer and a composite laminate in the middle (CARALL2/1). It is evident that all components of the model are defined as partitioned 3D solids. This facilitates mesh control and the assignment of material orientation. Furthermore, it facilitates the measurement of penetration, transient force transfer, and through-thickness damage evolution.

4.2.1.1 Target Plate

The target was modelled as a 3D deformable solid plate centred at the origin of the global coordinate system. This approach served to simplify the definition of the boundary conditions and subsequent post-processing. The diameter of the circular base is 100 mm, a measurement that corresponded with the dimensions of the experimental specimens. This was sufficient to limit the reflections of artificial stress waves from the constrained edges, thereby ensuring the integrity of the structure. The total thickness of the material was measured to be 2.4 mm, with the composition

of the material being two aluminium faces measuring 0.8 mm and a composite laminate measuring 0.8 mm. This layered representation facilitated the independent definition of the material properties, constitutive behaviour, damage criteria and orientations of the composite regions.

The composite laminate is composed of eight individual plies. In order to avoid the repetition of geometric operations, a single ply was initially created and partitioned as described in the following subsection. This component was then replicated sevenfold through the utilisation of the 'Create Part from Instance' tool within the Abaqus/CAE framework. Consequently, all plies were subjected to the same partition layout, while retaining independent material and orientation assignments throughout the laminate stacking sequence.

4.2.1.2 In-Plane Partitioning

In-plane partitioning was utilised to concentrate mesh refinement around the projectile trajectory, while permitting a gradual transition to a coarser mesh away from the contact region. As demonstrated in Figure 4.2, the impact zone, defined by a $40\,\text{mm} \times 40\,\text{mm}$ square, is surrounded by a coarse mesh region. The implementation of diagonal partitions resulted in the connection of the corners of the central square, thereby enhancing mesh regularity, controlling element distortion, and increasing the accuracy of the predicted stress, strain, and damage fields without incurring an excessive computational cost.

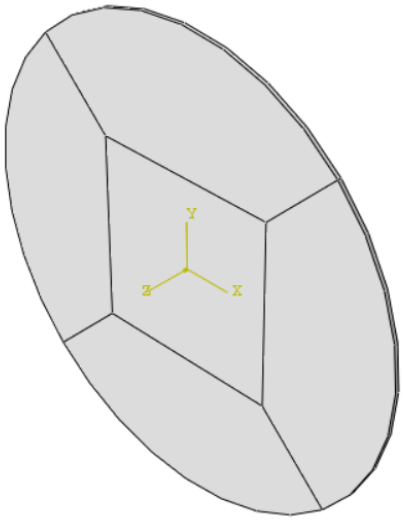


Figure 4.2: Aluminium and composite parts.

The partition layout was applied to the aluminium layers and to the initial composite ply before its duplication. Consequently, all eight plies were found to possess a consistent geometry and mesh structure, thereby eliminating the necessity to repeat the partitioning operations for each individual ply and consequently reducing the overall modelling time.

4.2.1.3 Projectiles

The projectiles were modelled in Abaqus/CAE as 3D analytical rigid bodies. As demonstrated in Figure 4.3, the diverse projectiles under consideration are presented, along with the pertinent measurements. In consideration of the constraints inherent to the extrusion of circular profile for the analytical rigid flat part, the cylindrical geometry was derived through the revolution of a rectangular sketch around the longitudinal axis. The same methodology was implemented for the different projectiles. This formulation neglects projectile deformation and consequently focuses the computational effort on the response of the target plate. The initial velocity was prescribed at the projectile reference point, and the projectile was positioned in close proximity to, though not in contact with, the target surface, with a view to preventing initial penetration and contact instabilities.

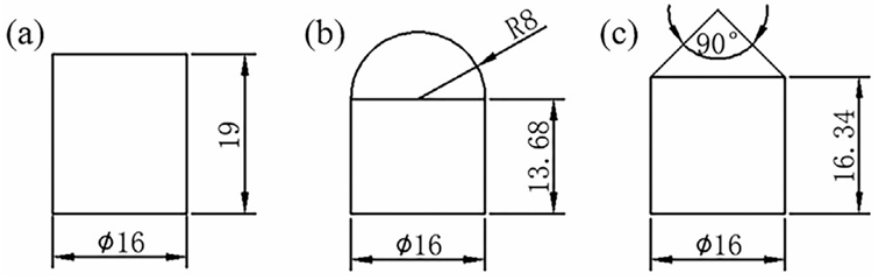


Figure 4.3: Geometric parameters of (a) flat, (b) hemispherical and (c) sharp projectiles [100]. Specimens dimensions are in mm.

In Figure 4.4 it is possible to observe the three shapes of projectiles modelled in Abaqus/Computer-Aided Engineering (CAE).

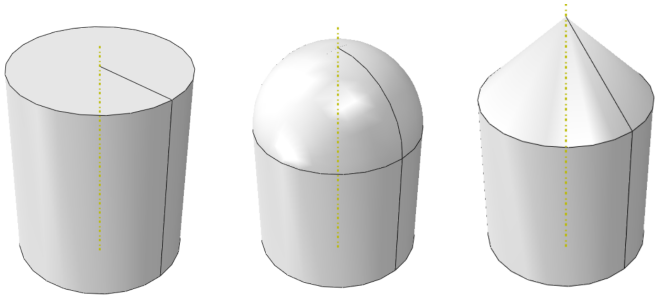


Figure 4.4: Projectiles analytical rigid parts.

4.2.2 Material Definition and Section Assignment

The model incorporated distinct materials corresponding to each physical region of the ballistic system, including the aluminium top and bottom faces and the composite plies. These were defined in the Property module of Abaqus/CAE and assigned to the respective parts using solid sections. In the case of the composite region, individual ply orientations were defined during section assignment in order to ensure accurate representation of the stacking sequence of the hybrid

laminate. In this phase, a uniform unit system was implemented in Abaqus/CAE for all quantities, encompassing geometry, material parameters, contact data, loads, boundary conditions, kinematic values, and output requests. Inconsistencies in units have been demonstrated to frequently result in nonphysical behaviour. Consequently, unit consistency was verified at every stage of the process.

4.2.2.1 Aluminium Layers

The aluminium layers were defined using an elastic-plastic constitutive law that is suitable for high strain-rate applications. In the field of ballistic loading, the J-C model is frequently adopted for its ability to account for strain hardening, strain-rate sensitivity and thermal softening in a compact phenomenological formulation. When coupled with a damage initiation and evolution law, this model can reproduce the onset of ductile failure and material erosion in regions undergoing intense plastic deformation.

The J-C parameters were entered directly in Abaqus/CAE and its values are displayed in Table 4.1.

Table 4.1: Properties of 2024-T3 aluminium alloy [100, 101].

Property	**Unit**	**Value**	**Property**	**Unit**	**Value**
ρ	kg/m^3	2750	$\dot{\varepsilon}_0$	s^{-1}	1.00
E	GPa	72.2	T_r	K	293
ν	-	0.35	T_m	K	775
A	MPa	369	D_1	-	0.112
B	MPa	684	D_2	-	0.123
C	-	0.0083	D_3	-	1.5
n	-	0.73	D_4	-	0.007
m	-	1.7	D_5	-	0.0

As the displacement at failure required to define damage evolution in Abaqus/CAE was not reported in the literature, this parameter was determined through a calibration study. A series of simulations was performed, involving solely the aluminium plate. In these simulations, the displacement at failure was systematically varied, while all other model parameters remained constant. A comparison was then made between the numerical predictions and the experimental results for the aluminium plate reported in the reference study [99]. In accordance with the agreement that was established between the numerical and experimental responses explained in Section 4.4, a displacement at failure of 0.01 was selected and subsequently adopted in the hybrid model.

4.2.2.2 Composite Region

The laminate adheres to the $[0/90]$ stacking sequence, signifying a total of eight plies. In the finite element model, each ply was explicitly represented as an individual solid part within the

assembly. Despite the uniformity in plies' geometry, distinct material orientations and section properties were assigned to reproduce the prescribed stacking sequence.

The mechanical response of the composite plies was described using a user-defined constitutive model implemented through a VUMAT subroutine. The subroutine governs the orthotropic elastic response and the progressive damage mechanisms of the carbon-fibre composite, including the initiation and evolution of fibre and matrix failure under strain-rate-dependent loading.

It is imperative that the 16 mechanical constants are entered in the precise order stipulated by the VUMAT subroutine. The complete enumeration of input values, accompanied by their physical interpretation and units, is delineated in Table 4.2. This compendium of data was also employed to populate the designated "Mechanical Constants" field within the Abaqus framework. Figure 4.5 shows the 16 mechanical constants in Abaqus/CAE.

Table 4.2: Composite material properties (CFRP) [99, 100].

General properties		**Strength Values**		**Damage evolution parameters**	
Property	Value	Property	Value	Property	Value
E_{11}	135 GPa	X_T	2550 MPa	G_{ft}	90 N/mm
$E_{22} = E_{33}$	10.3 GPa	X_C	1050 MPa	G_{fc}	48 N/mm
$\nu_{12} = \nu_{13}$	0.25	Y_T	24 MPa	G_{mt}	0.504 N/mm
ν_{23}	0.38	Y_C	132 MPa	G_{mc}	1.0 N/mm
$G_{12} = G_{13}$	6.5 GPa	$S_{12} = S_{13}$	53 MPa		
G_{23}	3.91 GPa	S_{23}	89 MPa		
ρ	1570 kg/m^3				

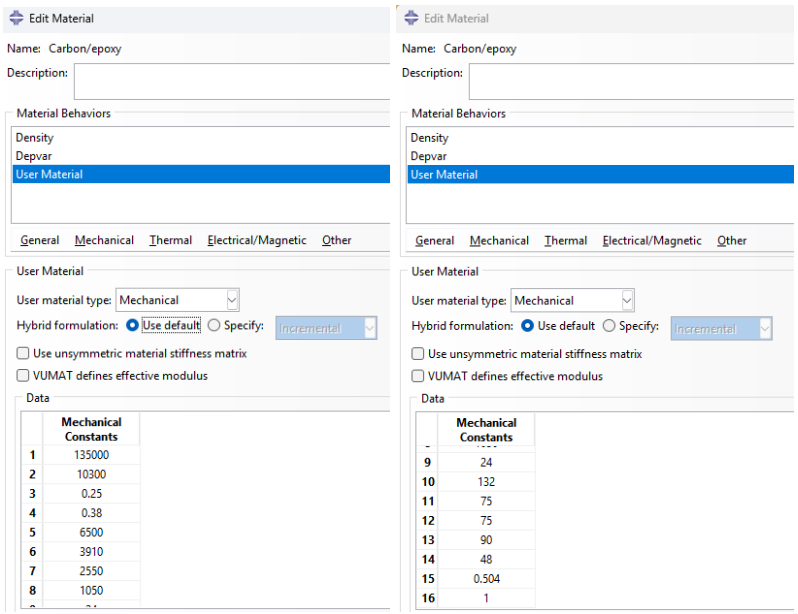


Figure 4.5: Mechanical constants input in Abaqus/CAE.

A concise excerpt of the VUMAT subroutine code is presented, illustrating the sequence in which these properties are processed. For comprehensive understanding, the complete subroutine is delineated in Appendix A.

```
C User defined material properties
C props(1) Young's Modulus E1
C props(2) Young's Modulus E2
C props(3) Poisson's ratio nu12
C props(4) Poisson's ratio nu23
C props(5) Shear modulus G12
C props(6) Shear modulus G23
C props(7) Fibre tensile stress Xt
C props(8) Fibre compressesive stress Xc
C props(9) Tranverse tensile stress mt
C propos(10) Tranverse compressive stress
C props(11) Matrix shear stress 12 S12
C props(12) Matrix shear sress 23 S23
C props(13) Fracture toughness E fibre tension Gft
C props(14) Fracture toughness E fibre compression Gfc
C props(15) Fracture toughness E matrix tension Gmt
C props(16) Fracture toughness E matrix compression Gmc
```

As stated in the opening paragraph of this section, the laminate lay-up was executed in accordance with a stacking sequence of $[0/90]$, thereby yielding a total of 8 plies. The implementation entailed the allocation of a distinct orientation definition to each ply, with the objective of aligning it with the in-plane fibre direction that corresponds to its nominal angle. The sequence and orientation of the stacking assignments have been meticulously designed to ensure that the model accurately captures the anisotropic and directional nature of the composite material under impact loading.

In order to simulate delamination between composite plies, a cohesive interface was defined using a traction–separation model. The material behaviour that is relevant in this case is that of the epoxy adhesive bonding the plies. This governs both the stiffness and the progressive damage across the interface. The properties employed, as outlined in Table 4.3, were subsequently incorporated into the Interaction module (Section 4.2.5) through the utilisation of surface-based cohesive contact definitions.

Table 4.3: Material parameters of the cohesive elements for CFRP interfaces [99, 102].

Property	**Unit**	**Mode I**	**Mode II**	**Mode III**
K_i	N/mm^3	10^6	10^6	10^6
$t_i^{\max}$	MPa	65	75	75
G_i^c	N/mm	0.504	1.0	1.0

In addition to the CFRP plies, thin adhesive interfaces were considered between the aluminium strike face and the first composite ply, and between the final composite ply and the rear aluminium face. In accordance with the experimental study, the aluminium and composite layers were bonded using the structural epoxy adhesive 3 M™ Scotch-Weld™ DP460 [99]. Accordingly, the cohesive properties assigned to these aluminium-CFRP interfaces represent the mechanical behaviour of the DP460 adhesive and were defined separately from those of the CFRP-CFRP interfaces. The adopted stiffness, peak traction and fracture-energy values are summarised in Table 4.4. These parameters strongly influence damage initiation and propagation at the bonded interfaces and, consequently, the predicted ballistic response of the hybrid laminate. The adhesive interfaces were subsequently implemented using surface-based cohesive contact in the Interaction module, as described in Section 4.2.5.

Table 4.4: Material parameters of the cohesive elements for the aluminium-CFRP bonded joint [100].

Property	Unit	Mode I	Mode II	Mode III
K_i	N/mm^3	10^6	10^6	10^6
$t_i^{\max}$	MPa	80	183	183
G_i^c	N/mm	0.3	0.6	0.6

4.2.2.3 Projectiles

The projectiles are defined as analytical rigid parts, thus rendering a material definition superfluous in Abaqus. The mechanical behaviour of the system is governed exclusively by its kinematic constraints. Consequently, there is no requirement to assign elastic or inertial properties within the "Property" module.

4.2.3 Assembly

The assembly was built up by precisely locating all the part elements in proper place. The part elements include the 8 CFRP plies, the aluminium faces and the projectile. In this case, each ply was modelled as an individual body, which simplified the use of the individual material orientation and interface definitions. The components were assembled without any impingement, which ensured a perfect contact between the plies that were adjacent to each other, as well as between the aluminium and composite regions.

The projectile was positioned at a standoff distance of 1 mm in front of the target, with alignment along the centre of the impact zone. It was imperative that the spacing was adequate to ensure that the initial contact occurred dynamically during the simulation. This was deemed necessary to facilitate the adequate development of contact forces and stress wave propagation upon impact, whilst concomitantly preventing initial contact interference.

The order in which the composite plies were inserted in the assembly was a matter of particular concern, since this sequence directly influences the fibre orientation and the resulting stacking

direction of the laminate. It is imperative that the correct stacking sequence is maintained in order to ensure that the model accurately reflects the intended laminate architecture. As demonstrated in Figure 4.6, a comprehensive overview of the complete assembly configuration is provided.

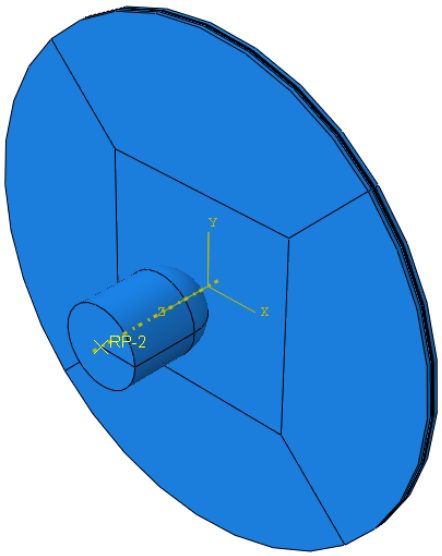


Figure 4.6: Complete assembly of the target and the hemispherical projectile.

The utilisation of a reference point proved instrumental in the control of the rigid body, the application of initial velocities, the assignment of mass to the projectile and the extraction of global quantities such as contact force, displacement and residual velocity. This assembly strategy also facilitates future parametric variations involving different impact locations, projectile geometries or target stacking sequences. This topic will be covered in Section 4.2.5.

4.2.4 Step Definition

The ballistic impact analysis was conducted using the Dynamic Explicit procedure available in Abaqus/Explicit. The selection of this formulation is attributable to the brief duration of the impact event and the severe nonlinearities associated with contact, large deformation and progressive material failure. A single analysis step, designated "Step-1", was defined with a total duration of 0.001 seconds, which was sufficient to capture the response from initial contact to projectile arrest or complete perforation.

In this step, the time incrementation was defined as *Automatic*, the stable-increment estimator was set to *Global*, and the *Improved Dt Method* option was enabled. No upper limit was imposed on the maximum time increment, and the time scaling factor was maintained at unity to preserve the physical time evolution of the impact event. Bulk viscosity was introduced to enhance numerical stability and suppress spurious oscillations during high-frequency wave propagation, using linear and quadratic coefficients of 0.06 and 1.2, respectively [90].

In this step, the time incrementation was defined as *Automatic*, the stable-increment estimator was set to *Global*, and the *Improved Dt Method* option was enabled. No upper limit was imposed

on the maximum time increment, and the time scaling factor was maintained at unity to preserve the physical time evolution of the impact event. Bulk viscosity was introduced to enhance numerical stability and suppress spurious oscillations during high-frequency wave propagation, using linear and quadratic coefficients of 0.06 and 1.2, respectively [90]. It should be noted that this feature provides purely artificial numerical damping to stabilize the explicit integration scheme and does not correspond to the physical structural damping of the materials, which was not modeled in this study.

In explicit dynamic analyses, severe element distortion can reduce the stable time increment to extremely small values, making the simulation computationally impractical. To overcome this limitation, mass scaling was implemented using the *Throughout Step* and *Scale to Target Time Increment* options as demonstrated in Figure 4.7. This technique selectively increases the density of the critical elements whose stable time increments fall below the prescribed target while leaving most of the model unaffected.

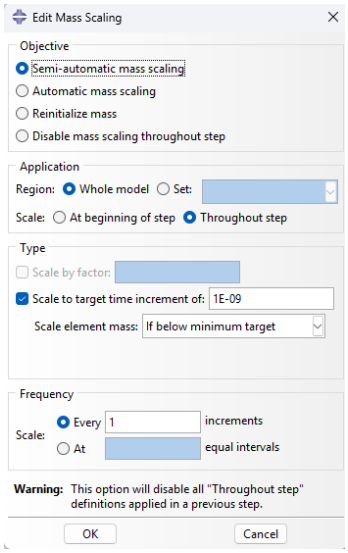


Figure 4.7: Mass scaling definitions in Abaqus/CAE.

Mass scaling was required only for the hemispherical and sharp projectiles because their geometries produced highly localised contact, severe element distortion and a substantial reduction in the stable time increment near the impact zone. By contrast, the flat projectile distributed the contact load over a larger area, resulting in less severe local distortion and a sufficiently large stable time increment. Consequently, mass scaling was not required for the flat-projectile simulations.

In order to assess the influence of the added mass on the predicted response, additional simulations were conducted, both with and without mass scaling. For an initial projectile velocity of 80 m/s, the rebound velocity was 1.695 m/s without mass scaling and 0.2271 m/s with mass scaling, corresponding to approximately 2.12% and 0.28% of the initial velocity, respectively. As kinetic energy is directly proportional to the square of velocity, the projectile retained only approximately 0.0449% of its initial kinetic energy without mass scaling and 0.00784% with mass scaling. Therefore, in both simulations, more than 99.9% of the initial projectile kinetic energy

was absorbed or dissipated. The minor discrepancy in rebound velocity is ascribed to the local unloading response of the severely distorted elements beneath the projectile, whose inertia undergoes a slight modification due to mass scaling. Nevertheless, the predicted structural integrity, damage development and impact-energy absorption remained effectively equivalent, thereby supporting the use of mass scaling in the hemispherical- and sharp-projectile models.

Field output was requested throughout the analysis step to monitor the transient response. The recorded variables included stress, strain, displacement, velocity, reaction force, and the relevant solution-dependent state variables associated with damage and failure. These outputs were stored at the appropriate nodal and integration-point locations to support the subsequent evaluation of contact forces, energy transfer, projectile residual velocity and the evolution of the different failure mechanisms.

4.2.5 Cohesive Zone Analysis and Contact Interaction

In this section, the cohesive zone analysis was performed for the purpose of simulating delamination between adjacent composite layers of different orientation and at the interfaces of aluminium and CFRP. Furthermore, the issue of contact interaction between the projectile and the target surface is also addressed.

It is noteworthy that all interactions between the model components were defined using the *General Contact (Explicit)* algorithm. This formulation is well-suited to ballistic impact simulations involving large deformation, evolving contact conditions, and element deletion. Throughout the analysis, a single general contact interaction, designated *Int-1*, was utilised to regulate contact between the projectile, the aluminium layers and the composite plies. While the general contact algorithm automatically detects the involved surfaces, specific frictional and cohesive responses were modelled by defining individual contact-property assignments for the different material interfaces, as demonstrated in Figure 4.8.

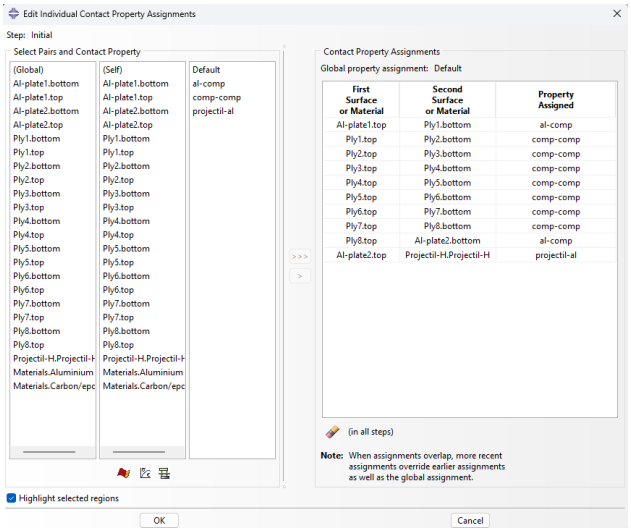


Figure 4.8: Contact property assignments for the projectile, aluminium and CFRP interfaces.

In this contact property assignment, interaction properties are assigned to specific surface interactions:

- *comp-comp*, applied between each pair of adjacent CFRP plies, with cohesive behaviour representing interlaminar delamination;
- *al-comp*, applied between the front aluminium layer and the first composite ply and between the final composite ply and the rear aluminium layer, with cohesive properties representing the DP460 adhesive;
- *projectil-al*, applied between the projectile impact surface and the external aluminium surface.

In these contact properties, the normal behaviour response was defined using the *Hard Contact* formulation, which prevents surface penetration while permitting separation after contact. Tangential behaviour was described using the *Penalty* formulation with isotropic Coulomb friction. They also include a friction coefficient of $\mu = 0.30$ which realistically simulates the interaction between the materials. Assigning explicit contact properties ensures that the mechanical behaviour of each contact interface is correctly reflected during impact, delamination and sliding.

Cohesive behaviour was implemented directly within the contact properties *comp-comp* and *al-comp*, which were both assigned to general contact interaction *Int-1*. These properties incorporated the cohesive stiffness, traction limits and fracture energy values defined in Tables 4.3 and 4.4.

In both cases, damage initiation was governed by a quadratic nominal-stress criterion and damage evolution was defined through an energy-based mixed-mode formulation, following the theoretical model introduced in Section 3.4. The implementation of the *comp-comp* cohesive property in Abaqus/CAE is presented in Figure 4.9. The *al-comp* property followed the same definition procedure but used different numerical parameters. All cohesive interactions were active from the start of the analysis and remained valid throughout the simulation.

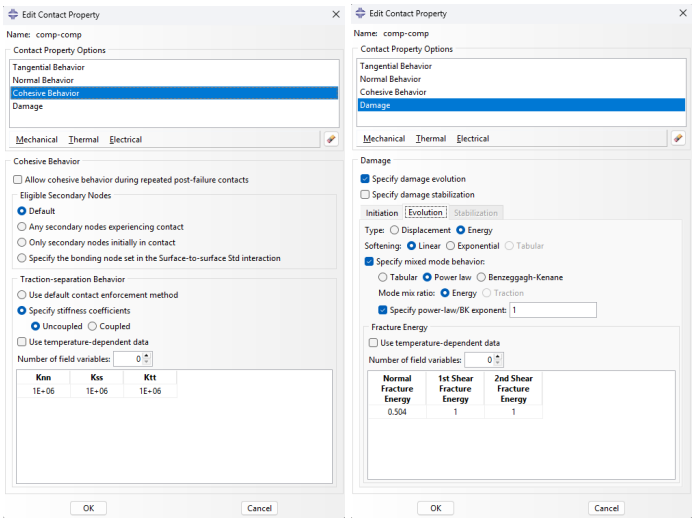


Figure 4.9: Definition of the *comp-comp* contact property in Abaqus/CAE.

The analytical rigid projectile was controlled through a *Rigid Body* constraint defined in the *Interaction* module. Its analytical surface was linked to a reference point that governed the translational and rotational motion of the projectile. The projectile inertia was introduced by assigning an isotropic point mass of 30 g to this reference point using the *Special* menu with *Create Inertia* and *Point Mass/Inertia* option. This approach provides the required inertial response while retaining the computational efficiency of an analytical rigid-body representation.

4.2.6 Boundary and Initial Conditions

The load and boundary conditions were defined in the *Initial* step of the explicit dynamic process in order to reproduce the experimental impact configuration. These comprised the prescribed projectile velocity and the constraints applied to the target boundaries. As the analyses represented ballistic impact under ambient and initially unstressed conditions, no initial stress or temperature fields were introduced.

The impact velocity was set at the reference point of the analytical rigid projectile and oriented perpendicular to the target surface. Various impact velocities were considered in order to reproduce the experimental test conditions, assess the velocity-dependent response of the hybrid plate and determine its ballistic limit. These values also lie within the ballistic testing range discussed in Section 2.4. As the projectile was modelled as a rigid body, the velocity assigned to its reference point determined the motion of the entire geometry. All translational and rotational degrees of freedom were constrained, except for translation along the impact direction, as demonstrated in Figure 4.10. This ensured purely axial motion and prevented unintended lateral displacement or rotation.

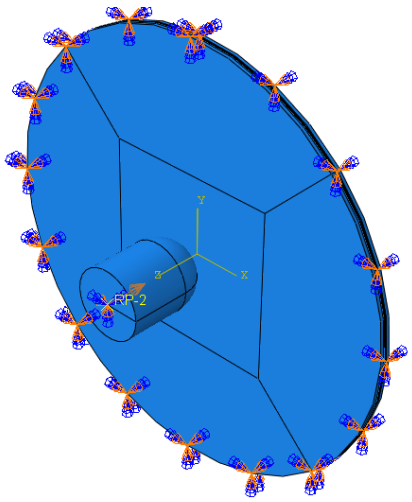


Figure 4.10: Boundary conditions applied to the target and projectile in Abaqus/CAE.

The experimental clamping system was modelled using *Encastre* boundary conditions on the outer edges of the front and rear aluminium layers. This configuration constrained all translational and rotational degrees of freedom in the supported region, while allowing the central impact area

to deform freely. In Section 4.3 is presented a sensitivity study to assess whether the constraints should be extended through the entire laminate thickness.

4.2.7 Mesh Definition

The mesh was designed to provide sufficient resolution of the projectile-target interaction while keeping the computational cost acceptable. Particular attention was given to the impact region, where steep gradients of stress, strain and damage were expected, as well as high-frequency stress-wave propagation. Therefore, a structured hexahedral mesh was adopted, with local refinement concentrated around the projectile trajectory and a gradual transition to a coarser discretisation away from the impact zone.

The target was discretised using eight-node, linear, reduced-integration brick elements (C3D8R). This element formulation strikes an effective balance between accuracy and computational efficiency in explicit analyses involving large deformation, progressive damage and element deletion. Reduced integration also limits artificial stiffness and decreases the computational cost, although appropriate hourglass control and element distortion monitoring remain necessary. Mesh biasing was applied through the thickness and towards the impact region to improve contact resolution and stress-wave transmission representation, and smooth mesh transitions were employed to minimise numerical instabilities (Figure 4.11).

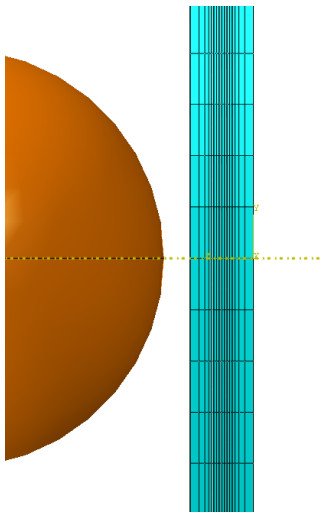


Figure 4.11: Local mesh refinement along the impact axis.

The final mesh comprised:

- 68 666 nodes;
- 40 960 C3D8R elements;
- a locally refined structured mesh in the impact region.

The characteristic element size was selected according to stress-wave propagation requirements, as discussed in the following subsection.

4.2.7.1 Mesh Size Selection for Stress Wave Resolution

The size of the characteristic element in the impact region was selected according to the requirements for resolving stress waves. In explicit dynamic analyses, the spatial discretisation must be sufficiently fine to accurately represent the highest-frequency components generated during the projectile–target interaction, while avoiding excessive numerical dispersion. The maximum admissible element size was therefore estimated using Equation 4.1,

$$L_{\mathrm{e}} \leq \frac{\lambda_{\min}}{n} \tag{4.1}$$

where L_e is the characteristic element length, $\lambda_{\min}$ is the shortest relevant wavelength and n is a safety factor typically set to 10.

The minimum wavelength is determined by Equation 4.2,

$$\lambda_{\min} = \frac{c_{\mathrm{d}}}{f_{\max}} \tag{4.2}$$

where $f_{\max}$ is the highest frequency considered relevant to the impact event and c_d is the representative dilatational wave speed of the hybrid target. The latter was estimated using Equation 4.3,

$$c_{\mathrm{d}} = \sqrt{\frac{E(1-\nu)}{\rho_{\mathrm{eff}}(1+\nu)(1-2\nu)}} \tag{4.3}$$

where E and ν are representative elastic properties and ρ_{eff} is the thickness-weighted effective density of the aluminium-CFRP target. Considering two aluminium layers, each with a thickness of 0.8 mm, and a CFRP laminate with a total thickness of 0.8 mm, the effective density was obtained in Equation 4.4,

$$\rho_{\mathrm{eff}} = \frac{\rho_{\mathrm{al}} \cdot t_{\mathrm{al}} + \rho_{\mathrm{CFRP}} \cdot t_{\mathrm{CFRP}}}{t_{\mathrm{al}} + t_{\mathrm{CFRP}}} = \frac{2750 \times (0.8+0.8) + 1570 \times 0.8}{0.8+0.8+0.8} \approx 2356.67 \text{ kg/m}^3 \tag{4.4}$$

where $t_{\mathrm{al}} = 1.6$ mm represents the combined thickness of the two aluminium layers and $t_{\mathrm{CFRP}} = 0.8$ mm is the total composite thickness. The equivalent in-plane elastic properties of the CFRP laminate were first calculated using classical laminate theory, based on the ply properties listed in Table 4.2. The laminate extensional stiffness matrix yielded the membrane properties $E_{\mathrm{eq}} = 72.906$ GPa and $\nu_{\mathrm{eq}} = 0.0354$. For consistency, the representative elastic properties E and ν used in the wave speed calculation were estimated using the same thickness-weighted average as the effective density. Considering the elastic properties of both the aluminium (mentioned in Table 4.1) and the CFRP layers, the effective values were calculated as $E = 72.435$ GPa and $\nu = 0.245$.

Using the effective target properties in Equation 4.3, a representative dilatational wave speed of approximately 6045.46 m/s was obtained. In the absence of a measured force-time history, a conservative maximum frequency of 250 000 Hz was adopted, consistent with frequency values

reported for fracture-related acoustic emissions in carbon/epoxy composites [103]. The corresponding minimum wavelength is calculated in Equation 4.5.

$$\lambda_{\min} = \frac{6045.46}{250\,000} = 24.18 \text{ mm}. \tag{4.5}$$

Substituting into Equation 4.1 yielded the maximum admissible characteristic element size,

$$L_e \leq \frac{24.18}{10} = 2.418 \text{ mm}. \tag{4.6}$$

Accordingly, elements with a characteristic length of approximately 1 mm were used in the region surrounding the impact point. A finer discretisation was adopted directly beneath the projectile contact surface. Away from the impact zone, the mesh gradually became coarser to reduce computational cost without introducing abrupt transitions in element size. All elements in the refined region remained below the calculated limit of 2.418 mm, providing adequate resolution of contact, stress-wave transmission, and progressive damage. The final discretisation was found to be suitable by monitoring the sensitivity of the principal response quantities, including residual velocity, absorbed energy and damage distribution. An overview of the final mesh distribution and refinement is shown in Figure 4.12.

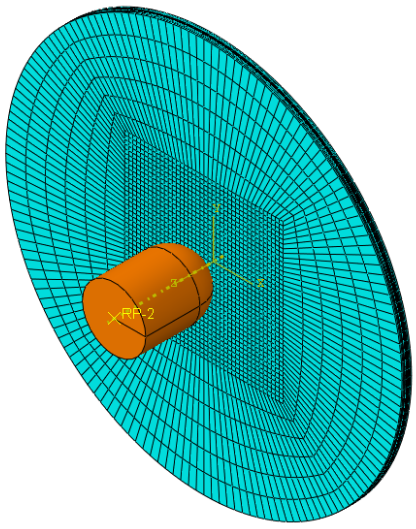


Figure 4.12: Final mesh configuration of the full model.

4.3 Boundary Condition Sensitivity

The sensitivity of the numerical response to the applied boundary conditions was assessed using two alternative constraint definitions. In the first configuration, the external boundaries of all aluminium and composite layers were fully constrained. In the second configuration, the constraints were applied exclusively to the upper and lower aluminium layers, while the internal composite plies remained connected through the previously defined contact and cohesive interactions. All

other material, geometrical, contact and numerical parameters were maintained unchanged, and both models were subjected to an initial projectile velocity of 100 m/s.

Table 4.5: Residual velocity obtained using the different boundary condition definitions.

Boundary Condition	v_r [m/s]
All layers constrained	55.308
Outer aluminium layers constrained	54.085

As demonstrated in Table 4.5, the constraining of all laminate layers resulted in an augmentation of the predicted residual velocity by only 1.223 m/s relative to the model in which solely the outer aluminium layers were constrained. This discrepancy corresponds to approximately 2.26% of the reference residual velocity and was therefore deemed inadequate to modify the interpretation of the global ballistic response. The results suggest that constraining solely the upper and lower aluminium layers provides an adequate representation of the target support for the present impact configuration.

Consequently, the outer-layer constraint was adopted in all subsequent simulations. This definition serves to reduce the number of directly constrained degrees of freedom and simplifies the process of model preparation, while preserving a residual-velocity prediction that is close to that obtained with the fully constrained laminate. This approach reproduced the experimental fixture without over-constraining the model while allowing the internal composite plies to deform as required.

4.4 Aluminium and Composite Models Calibration

Prior to the evaluation of the hybrid laminate, the aluminium and composite material models were calibrated independently against the constituent-only impact tests reported by Xu et al. [99]. The experimental responses of an aluminium-only plate and a composite-only laminate were utilised to ascertain the parameters that were not fully specified, as opposed to adjusting both material models simultaneously against the hybrid-target response. It is important to note that calibration was performed exclusively for the flat-nosed projectile. The resulting parameter sets were subsequently utilised without further adjustment for the hemispherical and sharp projectiles, with their applicability assessed through the comparisons presented in the following section.

In the case of the aluminium model, the displacement at failure that governs damage evolution was calibrated using a 2024-T3 plate with a thickness of 2.5 mm. The reported experimental ballistic-limit velocity of 123 m/s was prescribed as the initial projectile velocity. The parameter was adjusted with the aim of obtaining a final projectile velocity of zero or close to zero, whilst maintaining the adopted elastic properties, J-C plasticity, and damage-initiation parameters.

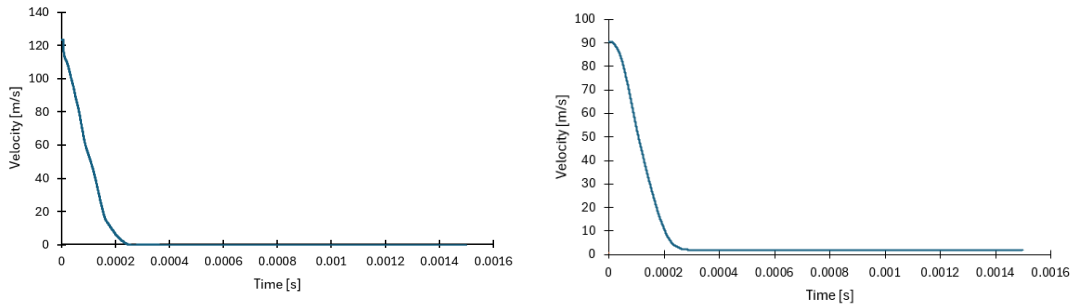
For the composite model, the calibration reference was a $[0/90]$ laminate with a thickness of 4 mm (40 plies). The experimental ballistic-limit velocity of 90.3 m/s was likewise prescribed as the initial projectile velocity. The parameters calibrated within the VUMAT were the maximum

strain rate scaling factors, β_{max}, whose calibrated values are presented in Table 3.1. These factors were adjusted with the same aim of obtaining a final projectile velocity of zero or close to zero.

For both constituent models, calibration therefore consisted of monitoring the projectile velocity at a prescribed initial velocity equal to the experimental ballistic limit, rather than independently determining a numerical ballistic limit from a range of impact velocities. Table 4.6 summarises the prescribed initial velocities and includes the numerical residual velocity, v_r, to assess how closely the final projectile velocity approaches the calibration target of zero. The corresponding numerical projectile velocity histories are presented in Figure 4.13. This procedure does not provide an independent estimate of the numerical ballistic limit or a percentage error relative to the experimental value.

Table 4.6: Aluminium and composite calibration results.

Target	**Thickness** [mm]	**Experimental** $v_{bl,\text{exp}}$ [99] [m/s]	**Numerical** v_r [m/s]
2024-T3 aluminium	2.5	123	0.817
Composite (40 plies)	4.0	90.3	−1.715



(a) Aluminium (b) Composite

Figure 4.13: Velocity-time history for aluminium and composite calibration models.

The residual velocities reported in Table 4.6 were 0.817 m/s for the aluminium plate and −1.715 m/s for the composite laminate. It is evident that both values are minimal in magnitude when compared to the prescribed initial velocities and are in close proximity to the calibration target of zero. Consequently, the two constituent models were deemed to have been satisfactorily calibrated for the adopted loading conditions. This conclusion pertains to the near-zero final projectile velocity achieved in each calibration simulation, and does not represent an independent determination of the numerical ballistic limits.

4.5 Results and Discussion

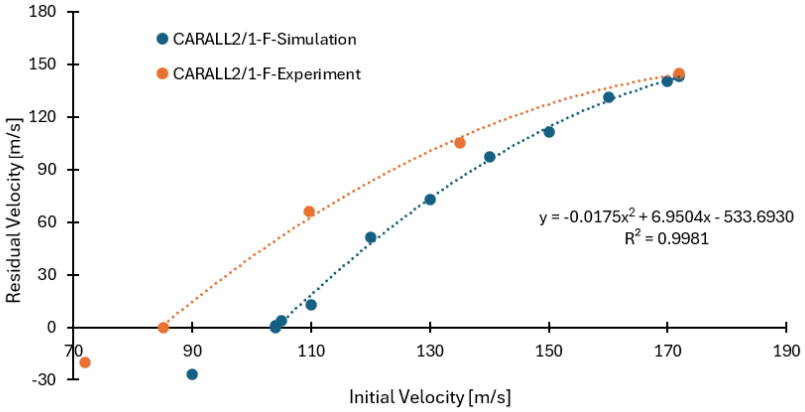
The primary objective of the present numerical campaign was to ascertain the ballistic limit of the aluminium-CFRP hybrid plate for the flat, hemispherical and sharp projectile geometries that were introduced in a previous study. For each projectile shape, simulations were conducted over a range of initial velocities, and the complete projectile velocity-time history was recorded. These histories provide a direct description of the deceleration process and allow the final outcome of each impact to be classified as projectile rebound, complete arrest or perforation with a positive residual velocity.

The ballistic limit for each projectile geometry was identified from the transition between non-perforating and perforating impacts. To elaborate further, the initial velocity was delineated as the highest velocity for which the projectile was arrested by the target, and the lowest velocity for which a positive residual velocity was obtained. The necessity to analyse the full interaction period, as opposed to solely the initial contact phase, was imperative, as it permitted the incorporation of late-stage mechanisms such as elastic recovery, interlaminar delamination, progressive fibre failure and secondary stress-wave reflections when assessing the final projectile velocity.

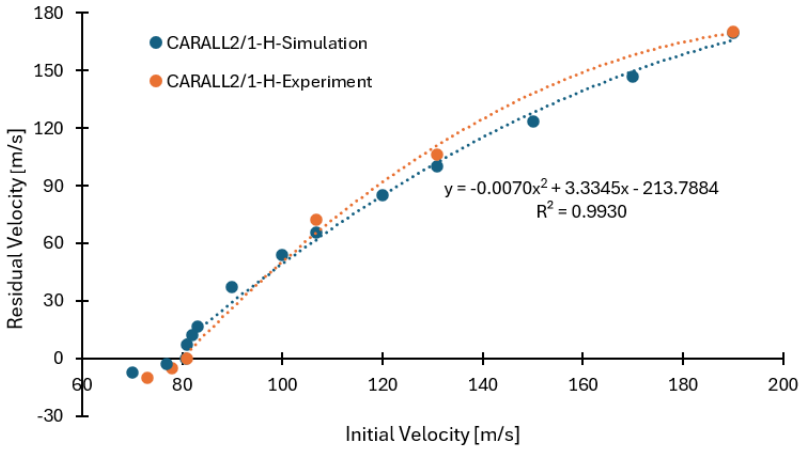
Projectile geometry exerts a direct influence on local contact pressure and the dominant failure mechanisms. Consequently, it was anticipated that this would result in different ballistic limits. The flat projectile distributes the load over a comparatively large area and promotes a more extensive shear- and plugging-dominated response. The hemispherical projectile produces progressive indentation and increases the contribution of laminate bending and delamination. Conversely, the sharp projectile concentrates the load over a small area, thereby promoting local penetration, fibre cutting and highly localised damage. Consequently, the ballistic resistance of the plate cannot be characterised by a single velocity independently of projectile shape.

A comparison was performed between the numerical results obtained in the present study and the experimental initial-residual velocity data reported by Xu et al. [99]. This comparison provides a reference for evaluating the ability of the numerical model to reproduce the global ballistic response of the aluminium-CFRP laminate. Nevertheless, disparities may emerge from the adopted mesh resolution, contact enforcement, element-deletion criteria, material parameters and post-processing procedure. In particular, the locally refined mesh preserves rapid variations associated with contact, stiffness degradation and ply-by-ply failure, potentially producing sharper changes in projectile deceleration than those obtained using a homogenised material description or a uniform mesh. The ensuing comparison will thus concentrate on the relationship between initial and residual velocities, and the resulting ballistic-limit estimate for each projectile geometry.

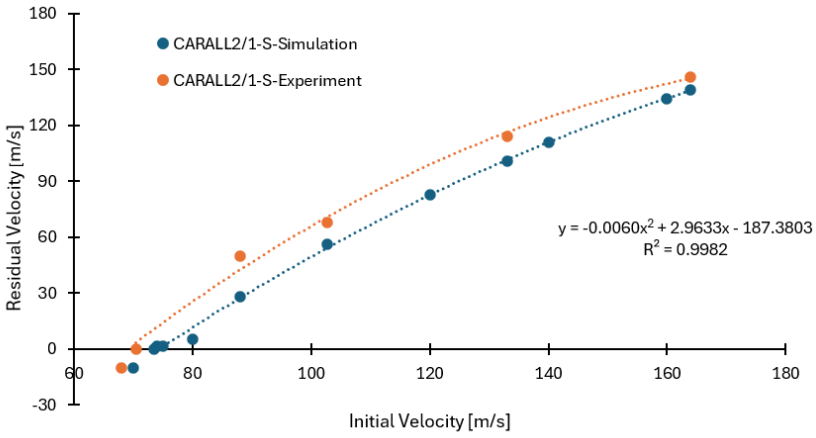
As illustrated in Figure 4.14, a comparison is drawn between the experimental data reported by Xu et al. [99] and the numerical results obtained for the flat, hemispherical and sharp projectiles.



(a) Flat projectile.



(b) Hemispherical projectile.



(c) Sharp projectile.

Figure 4.14: Comparison of numerical and experimental [99] initial-residual velocity curves for different projectile geometries.

In order to ascertain the value of the ballistic limit associated with each projectile geometry, the Lambert-Jonas correlation was utilised, which is expressed in Equation 4.7.

$$v_r = a\left(v_i^p - v_{bl}^p\right)^{1/p} \tag{4.7}$$

where v_i is the initial impact velocity, v_r is the residual velocity and v_{bl} is the ballistic-limit velocity. The parameters a and p are fitting coefficients obtained from the initial-residual velocity data. The application of this correlation independently to each projectile geometry enables a direct comparison of the influence of projectile shape on the ballistic resistance of the hybrid plate. The fitted coefficients and the resulting ballistic-limit velocity obtained for each projectile geometry are summarised in Table 4.7.

Table 4.7: Experimental and numerical results for the ballistic limits of CARALL2/1.

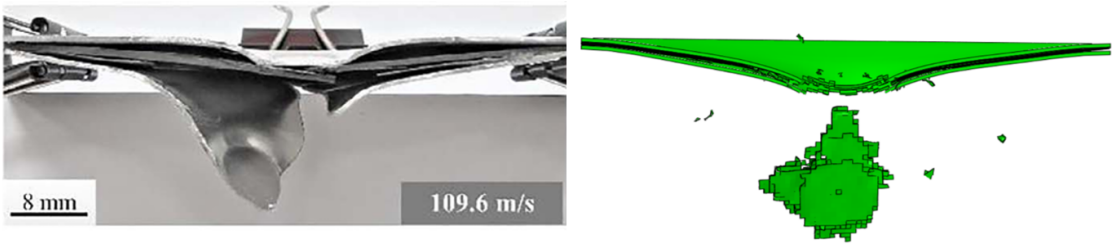
Projectile	**Experimental v_{bl} [99] [m/s]**	**Numerical v_{bl} [m/s]**	**Error**
Flat	85.2	103.928	21.98%
Hemispherical	80.9	80.756	0.178%
Sharp	70.5	73.495	4.25%

As demonstrated in Figure 4.14 and Table 4.7, the hemispherical projectile yielded the most proximate concurrence between the numerical and experimental ballistic limits, exhibiting an error of merely 0.178%. This agreement can be attributed to the comparatively progressive contact established by the rounded projectile nose, which promotes gradual indentation and macroscopic laminate bending. In this regime, the penetration resistance is predominantly governed by the in-plane tensile stretching of the composite plies and the global plastic deformation of the aluminium. Because the overall structural response is dominated by these well-characterised macroscopic mechanisms, the numerical prediction for the hemispherical configuration is inherently less sensitive to the uncertainties associated with the cohesive interface properties or the local element-deletion criteria.

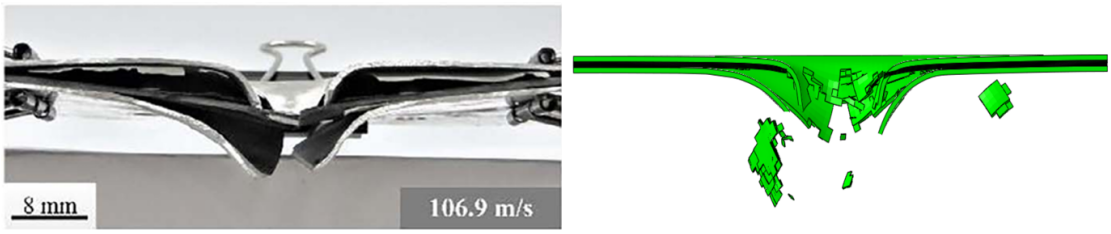
The larger discrepancies obtained for the flat and sharp projectiles reflect the greater sensitivity of their dominant penetration mechanisms to local modelling assumptions. The flat projectile promotes a plugging- and shear-dominated response over a relatively large contact area. Consequently, its predicted ballistic limit is strongly influenced by the J-C damage parameters, the calibrated displacement at failure, friction and the element-deletion criterion in the aluminium layers. Furthermore, although the numerical model aims to replicate the experimental tests conducted by Xu et al. [99], the cohesive zone properties were derived from multiple literature sources [99, 100, 102] (Tables 4.3 and 4.4). Therefore, it cannot be guaranteed that the exact same material specifications or manufacturing conditions were present. This inevitably leads to discrepancies in the results where delamination is a predominant failure mechanism, which is particularly the case for the flat projectile. The sharp projectile generates intense stress concentrations and highly localised fibre cutting, matrix damage and interface degradation, making its response particularly sensitive to mesh resolution and the progressive-damage formulation. However, the error obtained

for the sharp projectile remained relatively low at 4.25%. The results therefore demonstrate that the model captures the influence of projectile geometry.

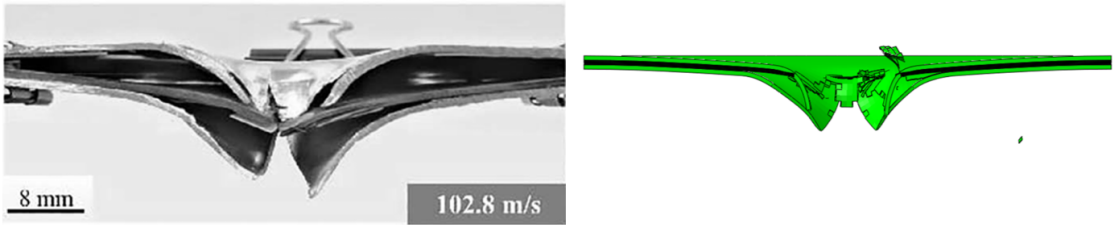
In order to complement the velocity-based assessment, a comparison is made in Figure 4.15 between the experimental cross-sections (left) with the numerical results (right) for flat, hemispherical and sharp projectiles at 109.6, 106.9 and 102.8 m/s, respectively. This enables a direct evaluation of the global deformation, failure patterns, interlayer separation and material fragmentation predicted by the model.



(a) Flat projectile.



(b) Hemispherical projectile.



(c) Sharp projectile.

Figure 4.15: Comparison between the experimental post-impact morphologies (left) and the corresponding numerical predictions (right) (Adapted from [99]).

The direct comparison presented in Figure 4.15 demonstrates close qualitative agreement between the experimental and numerical post-impact morphologies. The model successfully reproduces the global out-of-plane deformation of the multilayer target, including the characteristic dishing profile observed around the impact region. The magnitude and spatial extent of this deformation are consistent with the experimental cross-sections, indicating that the numerical formulation adequately captures the overall kinematic response of the target.

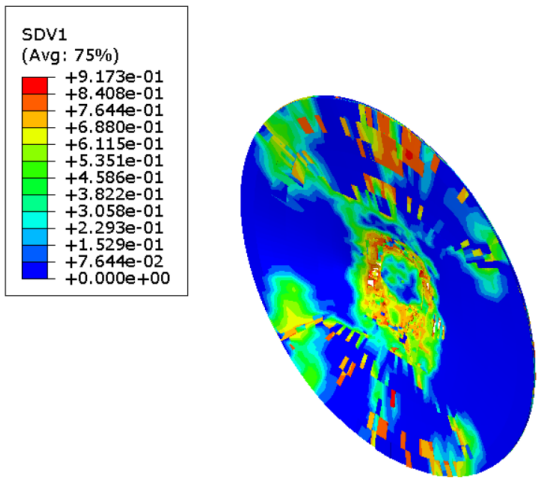
The principal failure mechanisms are also represented with good morphological fidelity. In particular, the simulations reproduce the formation and opening of petals on the rear face, together

with local material rupture and separation between adjacent layers. The experimental observation of interlayer opening is reflected in the numerical results, thereby providing support for the cohesive-interface and contact definitions that have been adopted. Furthermore, the generation and ejection of fragments during perforation indicate that the constitutive damage laws and element-deletion criteria reproduce the progressive loss of material associated with high-velocity impact.

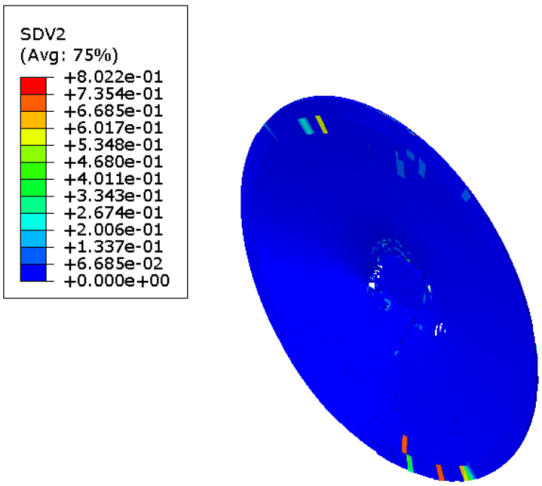
When considered in conjunction with the ballistic-limit results reported in Table 4.7, the morphological comparison provides both qualitative and quantitative support for the numerical model. The close ballistic-limit predictions obtained for the hemispherical and sharp projectiles, combined with the similarity between the experimental and numerical deformation and failure patterns, demonstrate that the model provides a robust representation of the dominant impact mechanisms. However, the larger error obtained for the flat projectile should be retained as a modelling limitation. The level of agreement achieved provides sufficient confidence for subsequent parametric investigations, whilst acknowledging that the accuracy of these investigations remains dependent on projectile geometry and the associated failure mode.

4.5.1 Influence of Projectile Geometry on Composite Damage

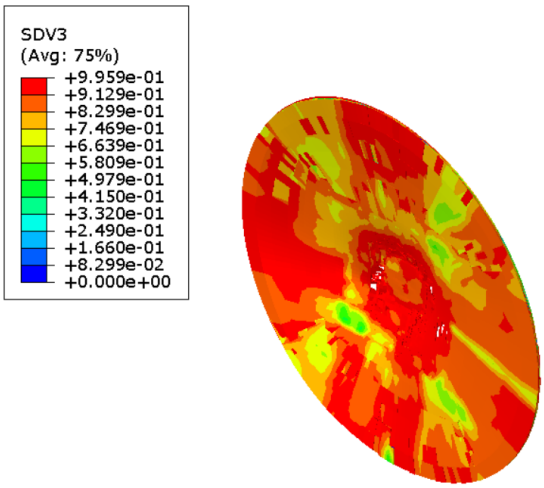
Beyond the comparison of ballistic limits and post-impact morphologies, a more detailed examination of the numerical results is required to investigate the failure mechanisms that develop during impact. The following discussion presents the State-Dependent Variables (SDVs) selected as most relevant to characterising these mechanisms for the flat, hemispherical and sharp projectiles, shown in Figures 4.16, 4.17 and 4.18, respectively. This analysis aims to examine how the failure modes and their spatial distribution differ between projectile geometries, since each nose shape may lead to a different failure response of the hybrid laminate. For each projectile, the reported values and contour plots were extracted at the instant immediately preceding complete perforation of the target. To provide an unobstructed view of the composite damage fields in these figures, the aluminium layers were hidden during post-processing, while remaining part of the simulated hybrid target.



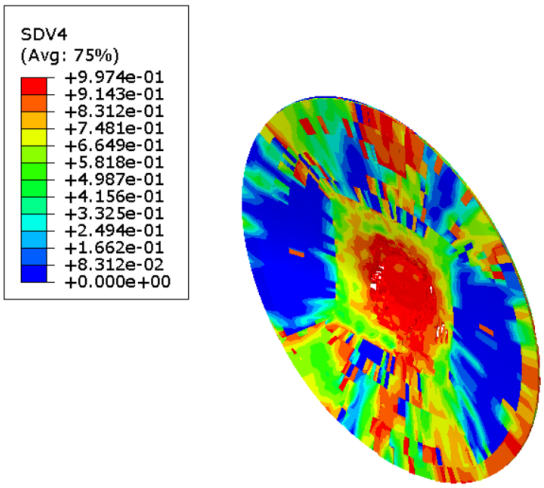
(a) SDV1–Fibre tensile damage.



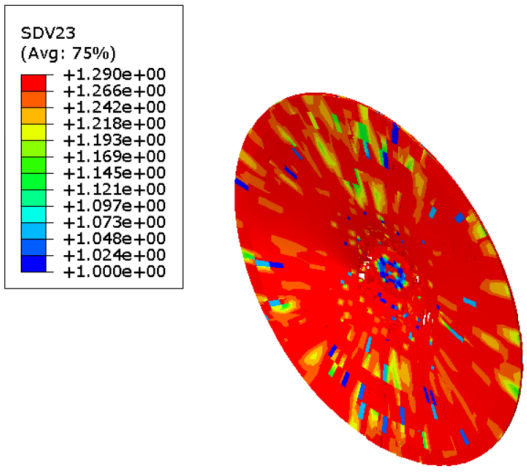
(b) SDV2–Fibre compressive damage.



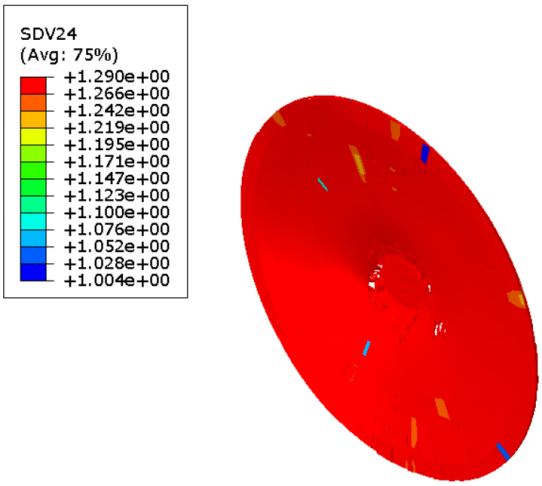
(c) SDV3–Matrix tensile damage.



(d) SDV4–Matrix compressive damage.

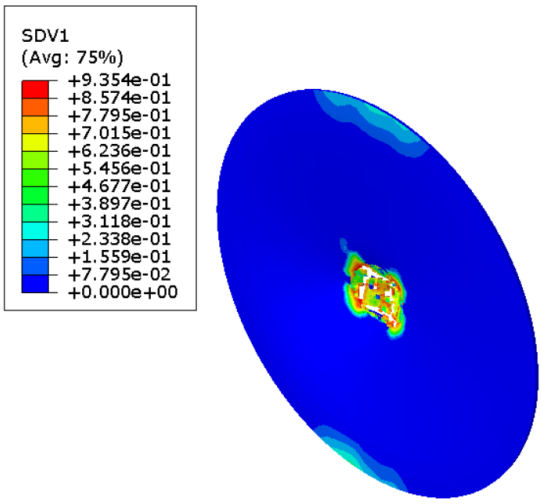


(e) SDV23–Strain rate amplification factor in the transverse direction (direction 2).

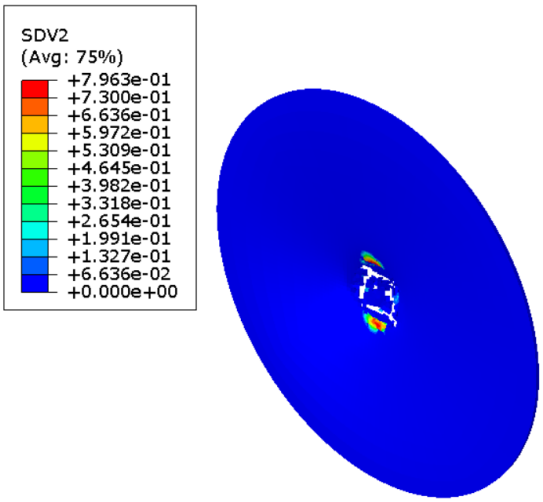


(f) SDV24–Strain rate amplification factor in the through-thickness direction (direction 3).

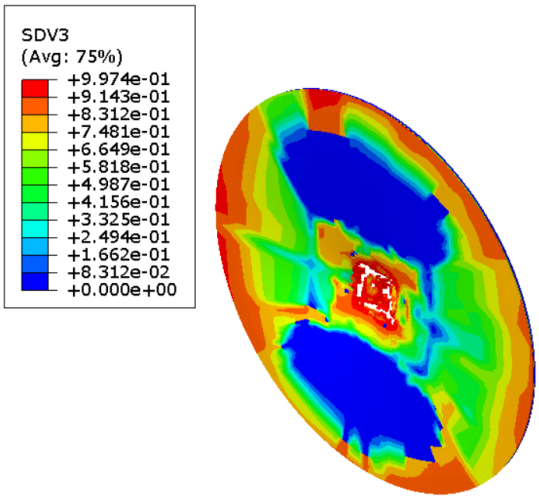
Figure 4.16: SDVs of the composite for the flat projectile impact.



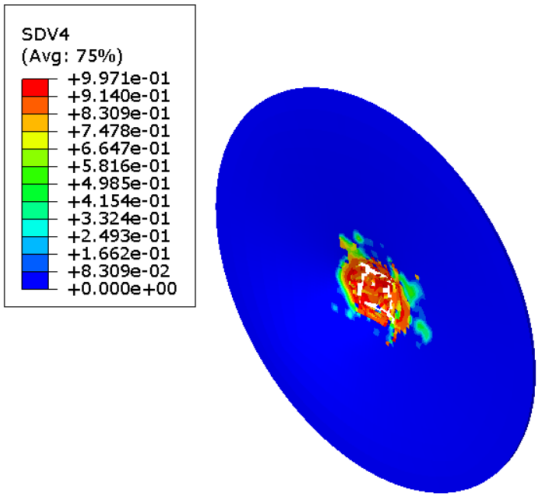
(a) SDV1–Fibre tensile damage.



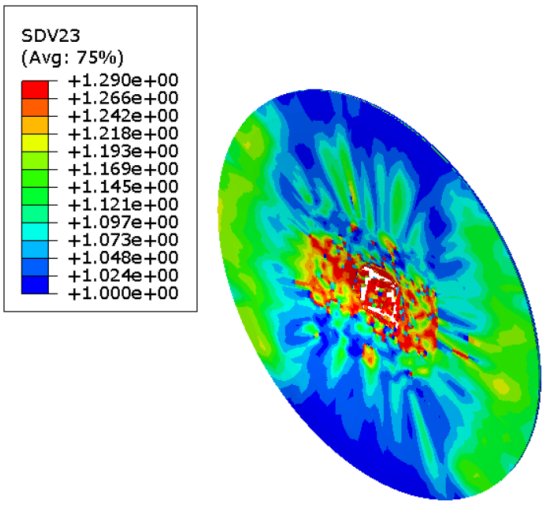
(b) SDV2–Fibre compressive damage.



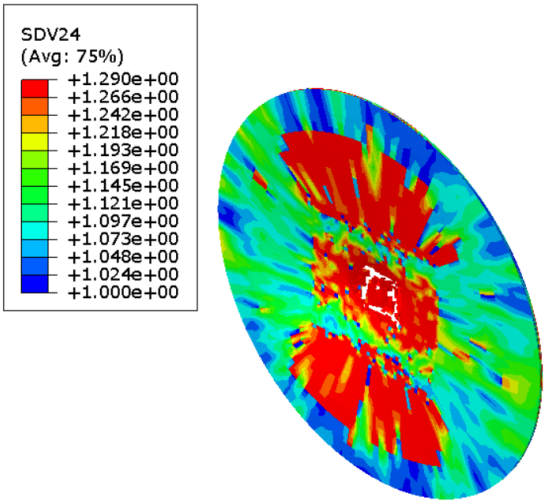
(c) SDV3–Matrix tensile damage.



(d) SDV4–Matrix compressive damage.

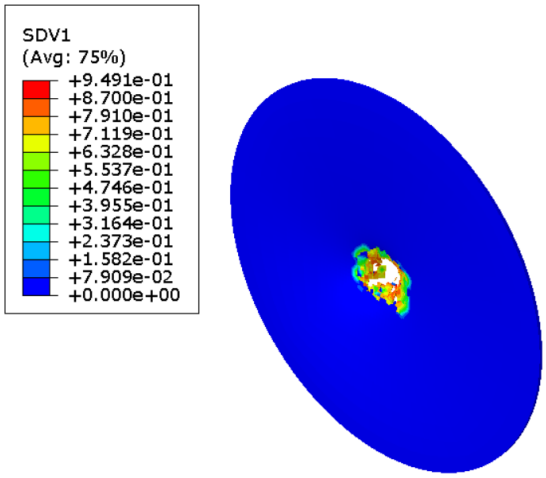


(e) SDV23–Strain rate amplification factor in the transverse direction (direction 2).

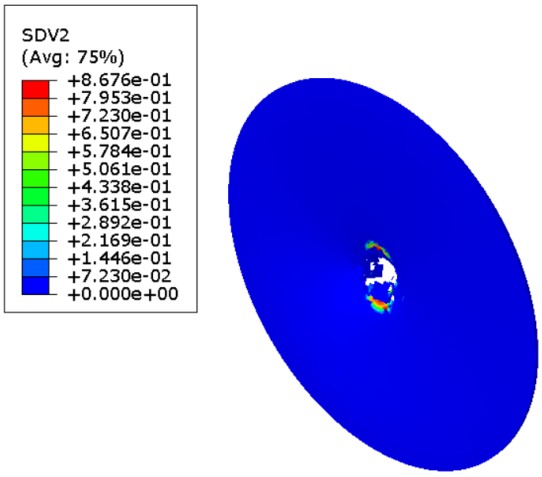


(f) SDV24–Strain rate amplification factor in the through-thickness direction (direction 3).

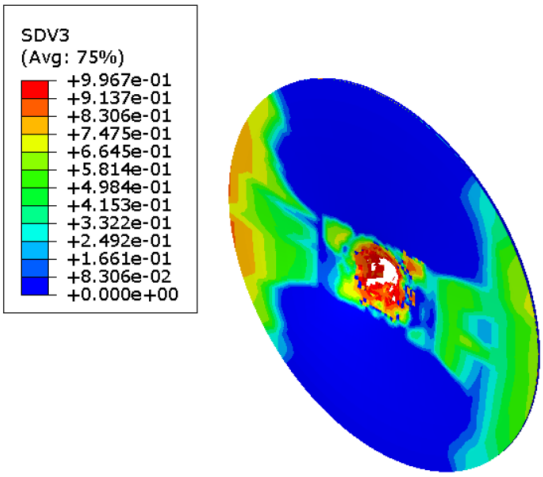
Figure 4.17: SDVs of the composite for the hemispherical projectile impact.



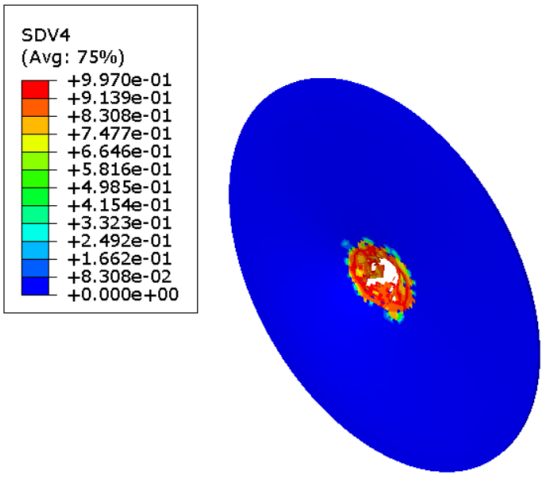
(a) SDV1–Fibre tensile damage.



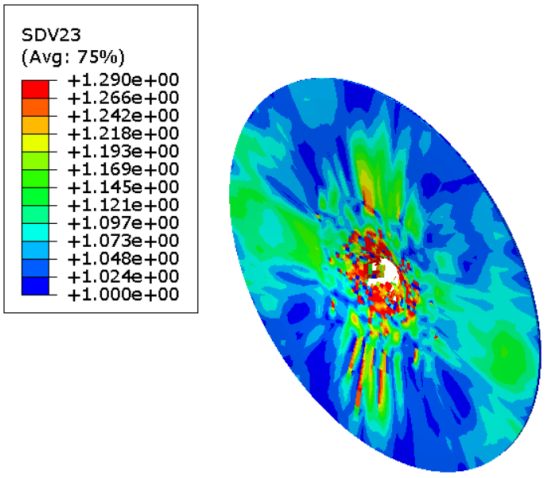
(b) SDV2–Fibre compressive damage.



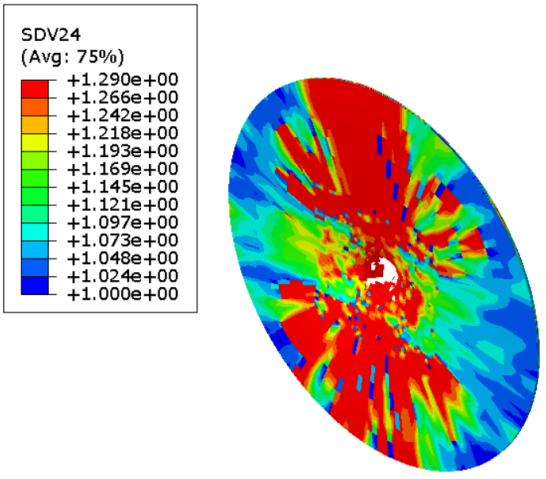
(c) SDV3–Matrix tensile damage.



(d) SDV4–Matrix compressive damage.



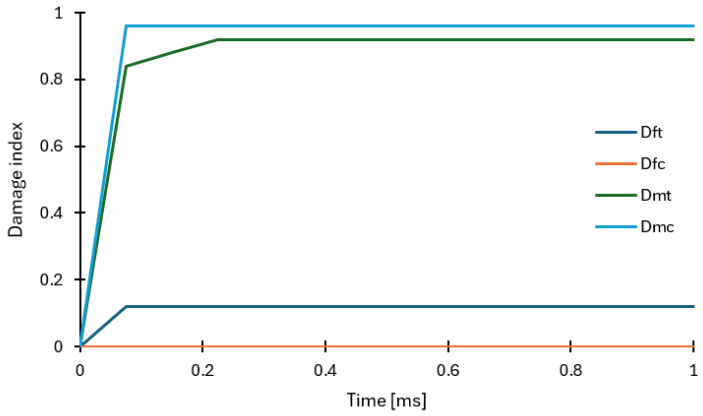
(e) SDV23–Strain rate amplification factor in the transverse direction (direction 2).



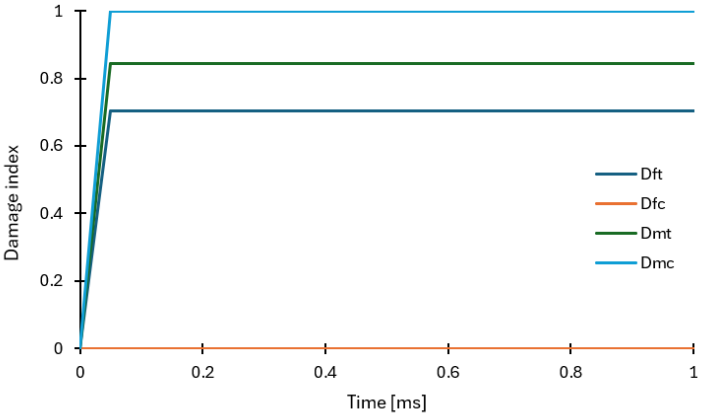
(f) SDV24–Strain rate amplification factor in the through-thickness direction (direction 3).

Figure 4.18: SDVs of the composite for the sharp projectile impact.

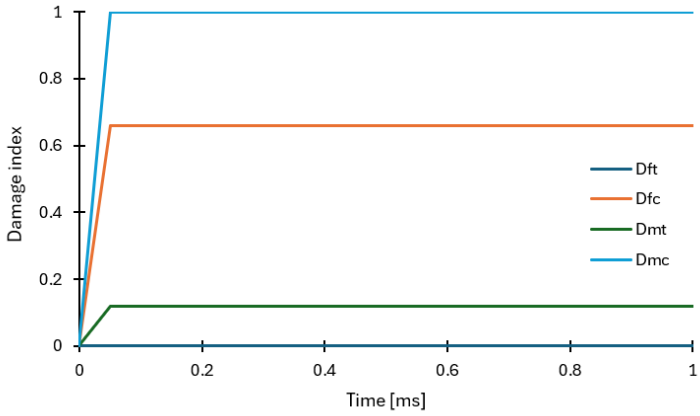
As demonstrated in Figures 4.16 to 4.18, there is a significant variation in the spatial distribution of composite damage immediately prior to complete target perforation. The flat projectile produces the most spatially extensive damage patterns, whereas the hemispherical and sharp projectiles concentrate fibre damage and matrix compressive damage around the penetration zone. These observations indicate a transition from a response involving a larger portion of the panel to a more localised penetration mechanism as the projectile nose becomes sharper. However, matrix tensile damage extends beyond the immediate contact region for all three geometries, so the response cannot be described as exclusively local, even for the sharp projectile. As the figures represent individual pre-perforation states, they characterise the accumulated damage at the selected stage rather than establishing the chronological sequence of failure initiation. In order to complement these observations, time histories of the fibre and matrix damage variables were extracted from a central element in the final composite ply, on the side opposite to impact, for each projectile geometry (flat, hemispherical and sharp). This location was selected because its response was considered more representative of the local damage evolution during impact. The resulting plots, presented in Figure 4.19, therefore describe the evolution at the monitored element rather than the damage state of the entire laminate.



(a) Flat projectile.



(b) Hemispherical projectile.



(c) Sharp projectile.

Figure 4.19: Comparison of fibre and matrix damage indexes for the different projectile geometries.

Figure 4.19 shows that most of the recorded damage develops during the early stages of impact, after which the variables approach approximately constant levels. Matrix compressive damage reaches high values for all three projectile geometries, while the other damage modes display distinct responses. At the monitored element, the flat projectile produces high matrix damage with comparatively limited fibre damage; the hemispherical case exhibits a more pronounced fibre tensile contribution, whereas fibre compression is more prominent in the sharp case. These observations provide an initial description of the local damage histories, without establishing the spatial extent or the mechanisms responsible for each response. The following sections examine fibre and matrix damage separately and relate these temporal trends to the corresponding Abaqus contour plots presented previously (Figures 4.16, 4.17 and 4.18).

4.5.1.1 Fibre Tensile and Compressive Damage

Fibre damage is important to the loss of load-carrying capacity of the composite. The spatial contours in Figures 4.16 to 4.18 are complemented by the time histories in Figure 4.19, extracted at the central element of the final composite ply. These histories describe the local evolution of fibre tensile damage (SDV1, labelled Dft) and fibre compressive damage (SDV2, labelled Dfc), rather than the maximum damage over the entire laminate.

The fibre tensile damage contours, represented by SDV1, provide a clear distinction between the three projectile geometries. As illustrated in Figure 4.16, the flat projectile's impact resulted in significant damage to the surrounding region, characterised by the presence of bands and patches of damage extending towards the perimeter of the panel. This distribution is consistent with load transfer to a wider region of the panel, although the spatial extent of damage alone does not establish whether bending, stretching or local shearing is the dominant mechanism. Fibre compressive damage, SDV2, is considerably less prevalent, with isolated affected regions observed near the impact zone and the perimeter. The flat projectile histories in Figure 4.19(a) show comparatively

limited fibre damage at the monitored element: SDV1 reaches approximately 0.12 following the initial loading, while SDV2 remains zero. Both curves subsequently remain essentially unchanged. In combination with the much higher matrix damage shown in the same graph, this response is compatible with punching-type loading dominated locally by matrix degradation and shearing, without substantial fibre damage at the selected location. The low local fibre values do not contradict the larger contour maxima elsewhere in the panel, nor do they imply negligible global bending or establish that material was ejected before fibre rupture.

Regarding the hemispherical projectile (Figure 4.17), the SDV1 field is more concentrated around the developing opening. It is evident that the region in question and the adjacent peripheral zones have undergone limited extension. However, the majority of the panel under scrutiny exhibits signs of low-fibre tensile damage. Similarly, SDV2 is highly localised. The rounded nose thus produces a pattern that is consistent with progressive indentation and local fibre loading, while maintaining some interaction with the wider panel. It is possible that bending and local shearing may contribute to this response, however, it is not viable to separate their individual contributions using these damage contours alone. For the hemispherical projectile, Figure 4.19(b) shows a substantially higher local SDV1, reaching approximately 0.70, while SDV2 remains zero. Unlike a gradual increase throughout the impact, the plotted history exhibits a rapid initial rise followed by a plateau. The predominance of tensile over compressive fibre damage is consistent with bending and membrane stretching of the rear composite ply as the rounded nose pushes into the laminate. This interpretation links the local tensile response to the progressive indentation mechanism, but the recorded value indicates partial fibre damage rather than complete tensile rupture at the monitored element.

The sharp projectile produces the most confined fibre damage pattern, as illustrated in Figure 4.18. As can be seen from the data, both SDV1 and SDV2 are concentrated around the immediate perimeter of the penetration zone. This distribution is consistent with a wedge-like penetration mechanism involving local fibre separation and rupture, rather than widespread fibre stretching. It is important to note that the higher local SDV1 maximum does not necessarily indicate a larger overall damaged region. In this case, the sharp projectile combines severe local degradation with low fibre damage over most of the visible panel. However, it is important to note that low SDV1 and SDV2 values away from the opening do not necessarily indicate that these regions are free from matrix or interlaminar damage. The sharp projectile histories in Figure 4.19(c) show the opposite local tendency: SDV2 rises rapidly to approximately 0.66, whereas SDV1 remains close to zero. Compression therefore dominates the fibre damage response at this location. This behaviour is consistent with a wedge-like penetration mechanism, in which the inclined nose surfaces displace material laterally and can compress fibres against the surrounding laminate. It contrasts with the tensile-dominated response of the monitored element in the hemispherical case. Nevertheless, this local comparison does not exclude tensile fibre damage elsewhere, as demonstrated by the SDV1 contours, and should not be interpreted as a uniform failure mode throughout the panel.

4.5.1.2 Matrix Tensile and Compressive Damage

The histories in Figure 4.19 complement the spatial contours by describing matrix tensile damage (SDV3, labelled Dmt) and matrix compressive damage (SDV4, labelled Dmc) at the monitored central element of the final composite ply. All three cases show substantial matrix degradation during the initial interaction, although the balance between tensile and compressive damage depends on projectile geometry. These curves identify the local evolution of damage, but their temporal resolution does not establish whether matrix damage initiates before fibre damage.

Matrix tensile damage, SDV3, is more spatially extensive than fibre damage in all three cases. As demonstrated in Figure 4.16, for the flat projectile the contour shows significant damage to the displayed panel. The widespread matrix degradation is consistent with substantial deformation and stress redistribution beyond the initial contact area. Matrix compressive damage, SDV4, also covers a comparatively large region, comprising an intensely damaged central zone and outward-extending bands. Collectively, these fields support the interpretation that the flat nose engages a larger portion of the laminate in the impact response. It has been demonstrated that global bending does not invariably establish itself as the predominant or sole mechanism, since local compression, shearing and plugging may coexist with distributed deformation. For the flat projectile, Figure 4.19(a) shows an abrupt increase in SDV4 to approximately 0.96, while SDV3 first rises to about 0.84 and subsequently approaches 0.92. The compressive contribution reaches its plateau earlier than the tensile contribution. These high matrix damage levels, compared with the limited fibre damage at the same element, are consistent with a local response dominated by matrix degradation under punching-type loading. Compression beneath the flat face and shearing near the boundary of the loaded region provide a plausible basis for plugging-type damage. However, the histories do not demonstrate a state of pure shear or complete matrix degradation at this element, since neither plotted matrix variable reaches unity.

In the case of the hemispherical projectile, the SDV3 field becomes more directional, displaying an approximately cruciform pattern, together with appreciable damage near parts of the perimeter. This morphology is consistent with preferential load redistribution along the principal directions of the cross-ply laminate, rather than an isotropic radial spread. In contrast, SDV4 is largely restricted to the contact region. The presence of both extended tensile matrix damage and confined compressive matrix damage indicates that local indentation occurs in conjunction with the deformation of the surrounding laminate. In Figure 4.19(b), the hemispherical projectile produces a rapid increase in SDV4 to approximately 1.0 during the first 0.05 ms, while SDV3 reaches approximately 0.84. Both variables then remain at essentially constant levels. The near-unity compressive damage is consistent with severe local matrix degradation as the rounded nose indents the laminate, whereas the tensile contribution is compatible with the accompanying bending and stretching response. Together with the directional SDV3 contours, these histories indicate that severe local compression can coexist with tensile matrix damage over a wider region. They do not, however, demonstrate progressive spatial propagation after the local curves have reached their plateaux; this would require contours at successive times.

The sharp projectile exhibits a directional SDV3 pattern, yet the visible affected area is more limited than that observed for the hemispherical projectile, particularly in regions distant from the principal damaged bands. The phenomenon of matrix compressive damage is characterised by its concentration around the penetration opening. The distinguishing feature is therefore the extent and morphology of matrix degradation. A smaller damaged footprint is consistent with more localised penetration, but does not demonstrate that stress waves have failed to reach the boundaries or that the remaining laminate is structurally intact. For the sharp projectile, Figure 4.19(c) also shows SDV4 reaching approximately 1.0 within the first 0.05 ms, whereas SDV3 remains much lower, at approximately 0.21. The local matrix response is therefore strongly dominated by compressive damage. This contrast is consistent with concentrated indentation and lateral displacement of material by the sharp nose, rather than extensive tensile deformation at the monitored element. When considered alongside the confined SDV4 contours, the history supports a localised penetration mechanism with severe matrix compression around the indentation zone. The directional tensile damage visible elsewhere nevertheless shows that the response is not restricted exclusively to the point of contact.

4.5.1.3 Strain-Rate Amplification Factors

As illustrated in Figures 4.16 to 4.18, the strain-rate amplification factors in the transverse and through-thickness directions are described by SDV23 and SDV24, respectively. It is important to note that, in contrast to SDV1-SDV4, these variables do not serve as damage measures. The upper value of approximately 1.290 corresponds to the calibrated maximum scaling factor for the transverse stiffnesses, as reported in Table 3.1. As demonstrated in Equation 3.37, this factor is subject to a limit in the high-rate regime. Consequently, identical maximum factors do not necessarily imply identical strain rates. Furthermore, these scalar fields are unable to identify whether the underlying deformation is tensile or compressive.

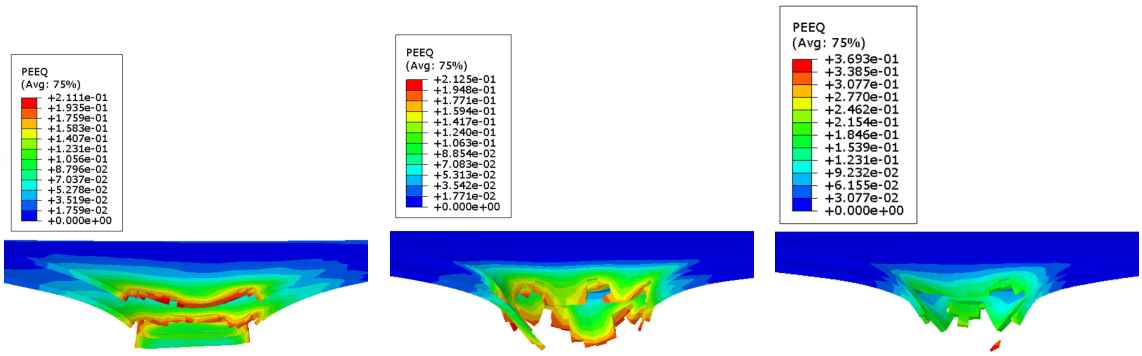
For the flat projectile, both amplification factors approach their upper limit over a substantial portion of the displayed panel, with SDV24 demonstrating a notably widespread near-saturated field. This pattern lends support to the observation that the rate-dependent material response is activated well beyond the immediate impact region. The hemispherical and sharp projectiles generate more heterogeneous fields, characterised by pronounced directional bands and substantial spatial variations. In particular, the sharp-projectile SDV24 contour contains high-amplification lobes extending towards the perimeter. It is therefore not confined to a narrow region adjacent to the hole. This distinction is of significance: localised irreversible fibre damage can coexist with a spatially extensive strain-rate-dependent response.

The analysis indicates that the flat projectile is associated with the widest distribution of composite damage, the hemispherical projectile combines local indentation with directional damage in the surrounding laminate, and the sharp projectile produces strongly localised fibre and matrix compressive damage. These patterns are qualitatively consistent with the ballistic-limit ordering in Table 4.7, where the flat projectile requires the highest initial velocity for perforation and the sharp projectile the lowest. However, it should be noted that contour extent alone does not quantify

absorbed energy or the relative contributions of fibre failure, matrix degradation, delamination and metallic plastic deformation. It is imperative that claims of maximum energy dissipation for the flat projectile, minimum dissipation for the sharp projectile, or higher residual velocities are assessed using energy histories and velocity comparisons at matched initial conditions. The present figures support a geometry-dependent change in damage morphology, while a quantitative assessment of penetration efficiency requires these complementary measures. The energy histories will be analysed in Section 4.5.3 to complement the damage assessment and examine the relationship between energy transfer to the target and projectile penetration.

4.5.2 Influence of Projectile Geometry on Aluminium Damage

The penetration response of the aluminium layers is examined through the Equivalent Plastic Strain (PEEQ), which characterises the accumulated plastic deformation and allows its magnitude and spatial distribution to be compared across the three projectile geometries. Although PEEQ is not a direct measure of fracture, its distribution helps identify regions of localised plastic deformation associated with the observed penetration mechanisms. In order to facilitate an unobstructed perspective on the deformation and tearing processes that occurred in the aluminium sheets, the intermediate composite layers were concealed during the post-processing stage. As illustrated in Figure 4.20, a comparative analysis is presented of the PEEQ distributions and cross-sectional penetration profiles for flat, hemispherical, and sharp projectiles. This analysis facilitates the localisation of plastic deformation, thereby enabling a correlation with material separation and displacement through the plate thickness.



(a) Flat projectile. (b) Hemispherical projectile. (c) Sharp projectile.

Figure 4.20: PEEQ of the aluminium for different projectiles geometries.

As demonstrated in Figure 4.20, the maximum PEEQ for the flat projectile is approximately 0.2111. Plastic deformation is observed to be concentrated in narrow bands that are aligned with the projectile perimeter. These bands define an approximate cylindrical boundary around the displaced material. In combination with the penetration profile, this configuration is indicative of a shear-dominated plugging mechanism, whereby a projectile propels a metallic plug through the plate, concomitant with the development of separation along its periphery. Global out-of-plane

deflection, or dishing, is less pronounced than in the hemispherical case, suggesting that local shearing contributes more strongly than distributed bending and stretching to the penetration process. However, PEEQ alone is unable to establish a state of pure shear or demonstrate that the material had insufficient time to bend, since it does not resolve the individual deformation components or their temporal evolution.

The hemispherical case attains a maximum PEEQ of approximately 0.2125, which is in close proximity to that achieved for the flat projectile. Despite the presence of analogous maxima, the deformation profile suggests a divergent failure mechanism. The distribution of plastic strain exhibited a more gradual nature around the impact region, while the cross-section demonstrated a more pronounced dishing effect. This combination is consistent with progressive indentation accompanied by bending and biaxial stretching of the central region. The presence of radial tearing and the formation of petals displaced towards the rear face suggest that ductile separation occurred following substantial deformation of the surrounding sheet. The rounded nose of the projectile engages a wider region of the aluminium through bending and stretching than the sharply bounded plugging response of the flat projectile. These mechanisms provide possible contributions to energy absorption, but their relative importance must be assessed from the energy histories rather than inferred from the local PEEQ maximum.

The sharp projectile exhibits the maximum local PEEQ among the three cases, with an approximate value of 0.3693. The largest values occur in the proximity of the torn edges of the opening, where the material undergoes severe local plastic deformation. The pointed extremity of the corolla acts as a wedge, displacing material laterally and producing pronounced petals folded in the direction of penetration. This morphology is consistent with local piercing and tearing as the opening expands. In comparison with the hemispherical case, plastic deformation and bending are more strongly concentrated around the hole, while the more distant portions of the displayed sheet remain comparatively flat. This does not establish that those regions are entirely undeformed or structurally intact, but rather indicates less extensive participation in the visible plastic deformation. The high local PEEQ is indicative of the accumulated plastic strain at the displayed stage, rather than an instantaneous rupture event or a universal fracture threshold.

The comparison presented in Figure 4.20 emphasises the distinction between the magnitude of local plastic strain and the mechanism governing penetration. It has been demonstrated that both the flat and hemispherical projectiles generate similar maximum values of approximately 0.211 and 0.213, respectively. However, it is noteworthy that these projectiles are linked to distinct phenomena, namely perimeter-controlled plugging and progressive stretching with petal formation. The sharp projectile produces a substantially higher maximum, approximately 0.369, within a more localised region of tearing and petal bending. It is imperative to refrain from interpreting these values as the plastic strains necessitated for perforation, or as a direct ranking of energy dissipation. The aluminium observations provide a valuable complement to the composite analysis by confirming differences in damage morphology between projectile geometries, without implying identical mechanisms in both constituents. Specifically, extensive composite damage under the flat projectile can coexist with localised plugging in the aluminium. The broader plastic de-

formation associated with the hemispherical projectile and the more confined tearing produced by the sharp projectile suggest different distributions of plastic work. However, they do not establish optimal energy absorption or a lower energetic barrier to perforation. These implications will be examined using the energy histories in Section 4.5.3.

4.5.3 Energy Balance

The preceding analysis identified differences in composite damage and aluminium deformation associated with the three projectile geometries. To complement these observations, this section examines how the initial projectile energy is distributed during impact and how this distribution relates to the penetration response of the hybrid laminate. The three simulations share an initial projectile velocity of 100 m/s and a projectile mass of 30 g, corresponding to an initial kinetic energy of 150 J ($\frac{1}{2} \times 0.030 \times 100^2 = 150$ J). Energy histories for the complete numerical model were extracted during post-processing. The analysis first establishes the global energy balance and its individual contributions, before comparing the kinetic and internal energy histories across the three projectile geometries.

4.5.3.1 Global Energy Contributions and Balance

The global balance provides the framework for accounting for the initial 150 J throughout the impact event. Considering the principal mechanical contributions, the reduced energy-balance expression is

$$\text{ETOTAL} = \text{ALLIE} + \text{ALLKE} + \text{ALLVD} + \text{ALLFD} - \text{ALLWK} \tag{4.8}$$

where `ALLIE` denotes the unmodified total internal energy, including artificial strain energy (`ALLAE`), recoverable strain energy (`ALLSE`), plastic disspation energy (`ALLPD`), damage dissipation energy (`ALLDMD`) and creep/viscoelastic dissipation energy (`ALLCD`). Also, `ALLKE` is the global kinetic energy, `ALLVD` is the energy dissipated by viscous effects, `ALLFD` is the energy dissipated by friction, and `ALLWK` is the work performed by externally applied loads [104]. Global kinetic energy includes both projectile and target motion, so the balance describes the response of the complete system rather than the projectile alone.

Artificial strain energy, recorded as `ALLAE`, is associated with numerical controls introduced by the element formulation, notably hourglass control in reduced-integration elements. Hourglass modes are deformation patterns that are not adequately resisted by the strain field evaluated at the integration points. Their control introduces an artificial resistance to suppress these non-physical modes. The associated energy is therefore not a direct measure of physical elastic storage, plastic deformation or fracture in the laminate [105].

In the present simulations, the value of `ALLWK` is found to be zero for all three projectile geometries. The clamped target boundaries remain static, thereby ensuring that their reaction forces do not contribute to the execution of work. It is important to note that no prescribed support motion or other external loading is performed during the impact step. The projectile velocity is

imposed as an initial condition, thereby supplying the initial kinetic energy rather than external work during the subsequent analysis. It is evident that the interaction between projectile and target results in a redistribution of energy within the complete model.

The contribution-by-contribution comparison is organised separately for the flat, hemispherical and sharp projectiles in Figures 4.21, 4.22 and 4.23, respectively. The assessment considers `ALLKE`, `ALLIE`, `ALLVD` and `ALLFD`, together with the reconstructed total, the directly requested `ETOTAL` history and the reference energy of 150 J. This representation provides the basis for assessing whether the selected terms adequately account for the initial energy, independently of the particular partition observed for each projectile.

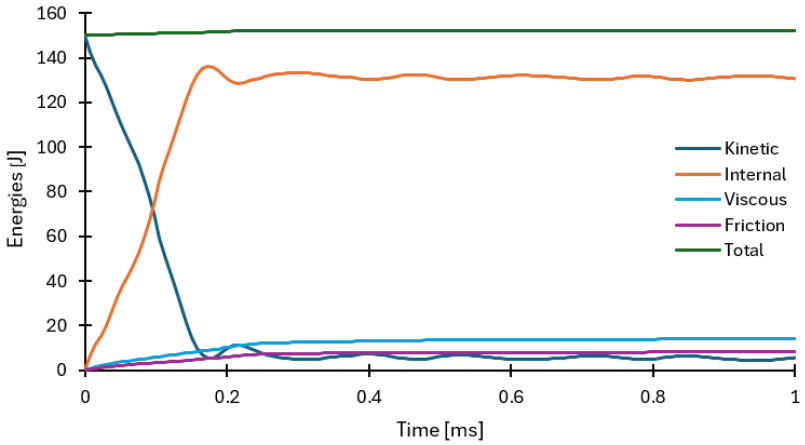


Figure 4.21: Energy contributions for the flat projectile.

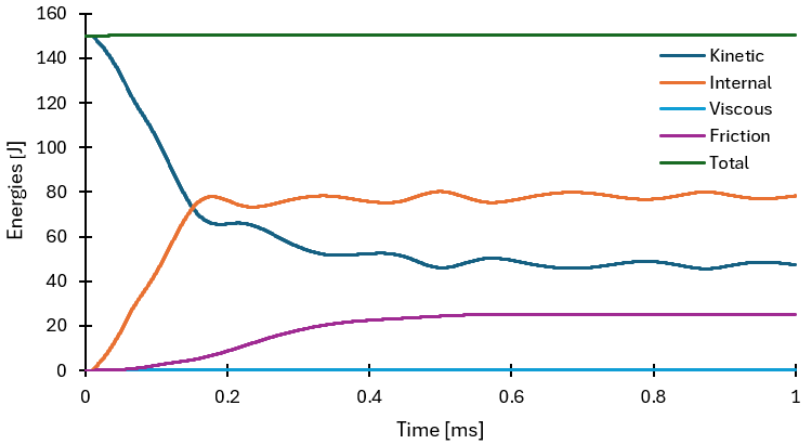


Figure 4.22: Energy contributions for the hemispherical projectile.

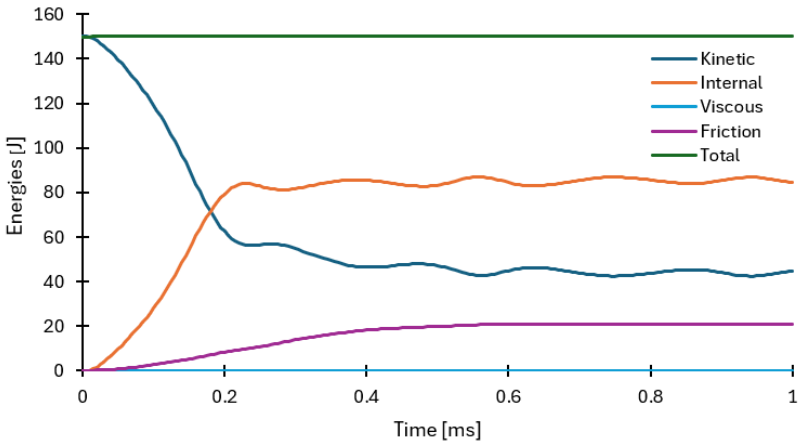


Figure 4.23: Energy contributions for the sharp projectile.

The energy contributions in Figures 4.21, 4.22 and 4.23 reveal distinct trends in viscous and frictional dissipation. The viscous dissipation energy, ALLVD, remains zero throughout the hemispherical and sharp simulations, whereas a non-zero contribution is recorded for the flat projectile. Conversely, the frictional dissipation energy, ALLFD, is lower for the flat projectile and higher for the hemispherical and sharp projectiles. In these latter two cases, frictional dissipation increases progressively until approximately 0.5 ms before approaching a plateau, while the flat projectile case does not exhibit the same sustained increase. These differences complement the kinetic and internal energy histories by showing that the contribution of each dissipation term varies with projectile geometry.

The viscous contribution requires a distinction between material behaviour and numerical damping. In Abaqus/Explicit, bulk viscosity introduces damping associated with volumetric strain rates to suppress high-frequency oscillations and regularise compressive wave fronts [106]. The abrupt loading of a wider region by the flat projectile may therefore contribute to its non-zero ALLVD, through the resulting transient volumetric deformation.

The higher frictional energy recorded for the hemispherical and sharp projectiles is consistent with continuous sliding of their lateral surfaces against the target material during penetration. For these geometries, the cross-sectional diameter increases progressively along the nose, from the tip towards the full-diameter cylindrical body. As the nose advances, the target therefore encounters progressively larger cross-sections, promoting lateral displacement of the surrounding material and sliding along the curved or inclined nose surfaces. Continued contact with the projectile sides can sustain this sliding as penetration proceeds, contributing to the progressive increase in ALLFD. By contrast, the flat projectile presents its full diameter at the leading face and maintains a constant diameter along its cylindrical body, without the gradual increase associated with the hemispherical and sharp noses. In the present simulation, its arrest before complete perforation further limits sliding through the target. The lower accumulated frictional energy is thus consistent with the combined influence of the nose profile and the restricted penetration path.

In all three cases, the total energy curve, labelled *Total*, remains constant at 150 J throughout the 1 ms simulation period. This behaviour indicates conservation of the system energy within the resolution of the plotted histories and supports the numerical stability of the simulations.

Having established the energy-accounting framework, the following comparison focuses on global kinetic energy and internal energy. From this point onwards, internal energy refers to ALLIE − ALLAE, rather than the complete `ALLIE` used in the preceding global balances. As discussed previously, `ALLAE` is an artificial energy contribution introduced by the numerical controls in Abaqus, rather than a direct measure of the physical material response. It is therefore excluded from the internal-energy comparison. Figures 4.24 and 4.25 groups the curves by energy type, allowing the three projectile geometries to be compared directly on the same axes and highlighting differences in the timing and magnitude of energy redistribution.

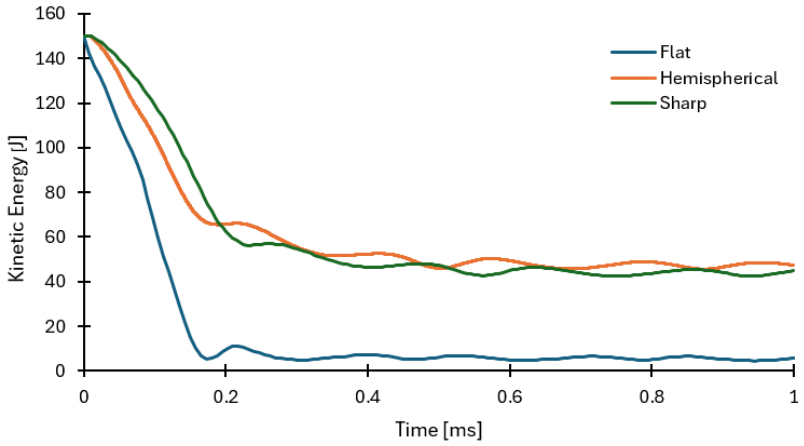


Figure 4.24: Global kinetic energy for the three projectile geometries at an initial velocity of 100 m/s.

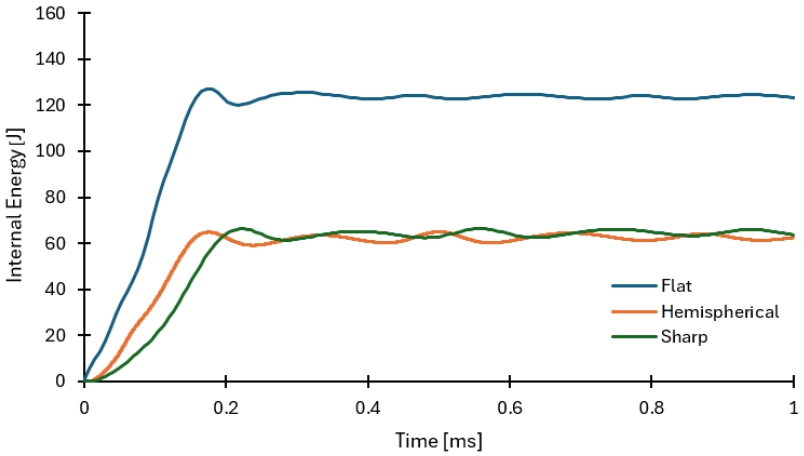


Figure 4.25: Internal energy excluding artificial strain energy for the three projectile geometries at an initial velocity of 100 m/s.

4.5.3.2 Kinetic Energy Evolution

Figure 4.24 shows a pronounced decrease in kinetic energy for all three projectile geometries during the initial interaction with the target. The flat projectile produces the most rapid and extensive reduction, with the global kinetic energy falling from approximately 150 J to a few joules within about 0.16–0.18 ms. A small subsequent recovery is followed by oscillations around a residual level of approximately 5 J. This response is consistent with projectile arrest in the numerical model, since the prescribed impact velocity is below the numerical ballistic limit of 103.928 m/s reported in Table 4.7. The low but non-zero residual energy indicates that motion persists within the system after the main impact interaction.

The hemispherical and sharp projectiles retain substantially higher kinetic energies. Following the initial decrease, their histories approach residual levels of approximately 40–50 J, with relatively small oscillations thereafter. This behaviour is consistent with the perforating responses at an impact velocity above their numerical ballistic limits of 80.756 and 73.495 m/s, respectively. The proximity of the two curves indicates similar remaining system kinetic energies at 100 m/s, without establishing identical projectile residual velocities or failure mechanisms.

4.5.3.3 Internal Energy Evolution

The internal energy histories in Figure 4.25 complement the kinetic energy trends by showing the evolution of the internal-energy contribution with artificial strain energy excluded. A clear distinction is again observed between the flat projectile and the other two geometries. For the flat projectile, the energy increases rapidly to a peak of approximately 127 J at around 0.17 ms, before decreasing slightly and oscillating around a later level of approximately 122–125 J. This corresponds to about 81–83% of the initial projectile kinetic energy. The decrease following the first peak, accompanied by a partial recovery of kinetic energy, is consistent with unloading and energy exchange within the deforming system. This percentage expresses the internal energy excluding artificial strain energy as a fraction of the initial kinetic energy; it is not a measure of irreversible dissipation alone.

The comparatively high internal energy level for the flat projectile is consistent with the more extensive composite damage identified previously and with the greater reduction in global kinetic energy. In the aluminium, however, the observed response remains predominantly associated with perimeter-controlled plugging rather than the more pronounced dishing identified for the hemispherical projectile. The energy histories and damage contours thus provide complementary evidence of different responses in the two constituents, without determining their individual contributions to the plotted internal energy.

The internal energies for the hemispherical and sharp projectiles are much closer to one another, generally oscillating within approximately 60–66 J after the initial transient. These levels represent about 40–44% of the initial kinetic energy. The hemispherical case exhibits an earlier initial rise, whereas the sharp case reaches its first maximum slightly later. Their subsequent curves remain close, with the sharp case showing marginally higher values during parts of the response.

This small difference does not support a strong separation of their energy absorption performance at the investigated velocity, despite their different numerical ballistic limits.

The lower internal energy levels of these two cases are compatible with the more localised penetration patterns discussed previously, including indentation, tearing and petal formation. They indicate a smaller internal energy contribution than in the arrested flat projectile case, but do not establish that the surrounding material remains undeformed. In particular, similar global energy levels can coexist with different spatial distributions of deformation and damage.

It is evident that when the kinetic and internal energy histories are considered collectively, a clear distinction emerges between the arrested flat projectile case and the perforating hemispherical and sharp cases at a velocity of 100 $\mathrm{m/s}$. The flat projectile produces the greatest reduction in global kinetic energy and the highest internal-energy level excluding artificial strain energy. The other two geometries retain substantially more kinetic energy and exhibit similar, lower internal-energy levels. These observations serve to complement the preceding damage analysis and provide support for a geometry-dependent penetration response under the investigated conditions. The global balances and the comparison of the individual histories serve complementary purposes: the former account for the initial energy and the numerical contributions, while the latter reveal how the energy partition differs between projectile geometries.

Chapter 5

Parametric Study

The present chapter conducts a parametric investigation, the findings of which are based on a numerical model that has been developed and validated in Chapter 4. The hemispherical projectile configuration is adopted as the reference case because it exhibited the closest agreement with the experimental ballistic limit. The present study evaluates the influence of material selection, geometrical parameters, boundary conditions and ply orientation on the ballistic response of the hybrid laminate. Unless stated otherwise, each parameter is varied independently while the remaining characteristics of the reference model are maintained constant, thus enabling the assessment of its individual influence.

The residual projectile velocity is utilised as the principal performance indicator, given that a reduced residual velocity is indicative of enhanced energy absorption by the target. In view of the superior results, a combination of the most effective factors is employed to calculate its ballistic limit, which is then compared with the CARALL2/1 performance calculated in the preceding chapter. In the process of comparison between different configurations, a number of complementary criteria are taken into consideration, including target mass, areal density, deformation and predicted damage mechanisms. This approach facilitates the identification of a lightweight material combination that provides improved ballistic resistance.

5.1 Influence of Material Selection

5.1.1 Aluminium Alloy

The influence of aluminium alloy selection on the ballistic response of the hybrid target was evaluated by replacing the 2024-T3 alloy adopted in the reference model. This approach enables the isolation of the contribution of the metallic layers, thus facilitating a direct comparison between alloys under identical impact conditions. The alternative materials selected for the study were aluminium 7075-T6, 5052-H32, AlSi10Mg and A356-T6, representing alloys with distinct combinations of density, stiffness, strength, strain hardening, strain-rate sensitivity and failure behaviour.

The parameters of elastic, J-C plasticity and damage for each alloy are outlined in Table 5.1. The properties of the reference 2024-T3 alloy are included to provide a consistent basis for comparison.

Table 5.1: Material properties and J-C parameters of the different aluminium alloys [107–110].

Property	**Unit**	**2024-T3**	**7075-T6**	**5052-H32**	**AlSi10Mg**	**A356-T6**
ρ	$\mathrm{kg/m^3}$	2750	2810	2680	2700	2680
E	GPa	72.2	71.7	70.3	75.0	72.0
ν	–	0.35	0.33	0.33	0.3	0.33
A	MPa	369	546	217	331	270
B	MPa	684	678	181	580	155
n	–	0.73	0.71	0.377	0.99	0.28
C	–	0.0083	0.024	0.135	0.032	0.018
m	–	1.7	1.56	1.561	0.945	1.43
$\dot{\varepsilon}_0$	$\mathrm{s^{-1}}$	1.00	1.00	1.00	1.00	1.00
T_r	K	293	293	293	293	293
T_m	K	775	893	878	843	830
D_1	–	0.112	−0.068	0.068	0.047	0.1
D_2	–	0.123	0.451	0.253	1.155	0.2
D_3	–	1.5	−0.952	−0.41	−0.841	1.3
D_4	–	0.007	0.036	0.015	−0.042	0.005
D_5	–	0.0	0.697	0.0	0.0	0.0

The evaluation of each alloy was conducted using the initial projectile velocity of 100 m/s adopted for the reference simulation. The resulting residual velocities are presented in Table 5.2. The relative variation was calculated with respect to the 2024-T3 reference case, with negative values indicating a reduction in residual velocity and, consequently, an improvement in ballistic resistance.

Table 5.2: Residual velocity response of the different aluminium alloys.

Aluminium alloy	v_r [m/s]	Δv_r [%]
2024-T3	54.085	–
7075-T6	−41.012	−175.83%
5052-H32	−25.855	−147.80%
AlSi10Mg	−27.926	−151.63%
A356-T6	64.894	19.99%

The residual-velocity results obtained at 100 m/s reveal two distinct responses: complete perforation for positive values of v_r and projectile rebound for negative values. Aluminium 7075-T6 demonstrated the highest ballistic resistance, exhibiting a projectile rebound velocity

of -41.012 m/s. This response is consistent with the material's high initial yield stress ($A = 546$ MPa) and strain-hardening coefficient ($B = 678$ MPa). In contrast, the A356-T6 specimen exhibited the highest positive residual velocity, measuring 64.894 m/s, due to its lower values of A (270 MPa) and B (155 MPa), which resulted in reduced resistance to continued penetration following yield.

The non-perforating responses of 5052-H32 and AlSi10Mg demonstrate that quasi-static strength alone does not determine ballistic performance. Despite exhibiting the lowest yield parameter ($A = 217$ MPa), 5052-H32 demonstrated a rebound velocity of -25.855 m/s, a phenomenon attributed to its high strain-rate sensitivity ($C = 0.135$) and the ensuing augmentation in dynamic flow stress. Furthermore, AlSi10Mg demonstrated its capacity to arrest the projectile, with a measured velocity of $v_r = -27.926$ m/s, as a consequence of the synergistic effect of strain hardening, strain-rate sensitivity, and damage evolution. The results therefore indicate that the complete constitutive and failure response must be considered when comparing candidate alloys.

The damage calibrations that were adopted further demonstrate that the perforated 2024-T3 and A356-T6 targets exhibited positive D_3 values, while the alloys that arrested the projectile demonstrated negative values. Despite the indication of a significant impact of stress triaxiality on fracture initiation, it is not possible to assess D_3 independently of the remaining damage parameters, strain rate and temperature. Overall, 7075-T6 provided the greatest direct stopping capability, while 5052-H32 achieved projectile arrest through a more deformation-driven energy-absorption mechanism. The effective design of lightweight armour must therefore achieve a balance between initial penetration resistance, governed principally by A and B, and the capacity to sustain dynamic plastic deformation without premature fracture, influenced by C and the complete J-C damage law.

5.1.2 Composite Material

The influence of composite material and reinforcement architecture on the ballistic response of the hybrid target was evaluated by replacing the reference UD T700S carbon-fibre composite. Initially, two alternative UD carbon-fibre systems, T1000G and AS4/PEEK, were investigated to assess the influence of different carbon fibres and matrix systems. The study was subsequently expanded to encompass Kevlar, S2-glass and UHMWPE, with each material undergoing evaluation in both UD and woven configurations. This methodological approach facilitated the assessment of the impact of material selection and reinforcement architecture under equivalent conditions. The properties that have been adopted for the UD and woven systems are summarised separately in Tables 5.3 and 5.4, respectively.

Table 5.3: Material properties of the UD composite systems [111–116].

Property	**Unit**	**T700S**	**T1000G**	**AS4/PEEK**	**Kevlar**	**S2-glass**	**UHMWPE**
ρ	kg/m^3	1570	1800	1560	1400	2000	980
E_{11}	GPa	135	177.84	122.7	15.43	50.0	153
$E_{22} = E_{33}$	GPa	10.3	9.0	10.1	5.4	9.0	11.3
$\nu_{12} = \nu_{13}$	–	0.25	0.272	0.25	0.37	0.33	0.3
ν_{23}	–	0.38	0.45	0.45	0.47	0.04	0.4
$G_{12} = G_{13}$	GPa	6.5	5.0	5.5	1.998	3.5	6.0
G_{23}	GPa	3.91	3.1	3.7	2.0	3.0	3.6
X_T	MPa	2550	3822	2070	405	2000	2537
X_C	MPa	1050	1450	1360	405	550	1580
Y_T	MPa	24	60	86	185	43	2537
Y_C	MPa	132	170	230	185	90	1580
$S_{12} = S_{13}$	MPa	53	85	186	66	93	575
S_{23}	MPa	89	65	86	40	50	120

Table 5.4: Material properties of the woven composite systems [114, 117, 118].

Property	**Unit**	**Kevlar**	**S2-glass**	**UHMWPE**
ρ	kg/m^3	1440	2750	970
$E_{11} = E_{22}$	GPa	10.44	27.5	25.0
E_{33}	GPa	6.88	11.8	8.0
ν_{12}	–	0.44	0.11	0.006
$\nu_{13} = \nu_{23}$	–	0.33	0.18	0.6
G_{12}	GPa	5.4	2.9	0.015
$G_{13} = G_{23}$	GPa	2.27	2.14	3.0
X_T	MPa	405	604	1250
X_C	MPa	405	291	1250
Y_T	MPa	405	604	1250
Y_C	MPa	405	291	1250
$S_{12} = S_{13}$	MPa	66	75	700
S_{23}	MPa	40	58	900

A significant modification of the UHMWPE laminates in relation to CFRP laminates involved the modelling of the interlaminar interfaces. In the CFRP model, individual plies were divided by a thin layer of epoxy, which was simulated numerically using cohesive contact formulations. This approach was necessary to accurately capture delamination, a primary failure mechanism in brittle carbon-epoxy composites. Conversely, UHMWPE laminates are typically manufactured through the process of hot pressing, whereby plies are consolidated under elevated pressures and

temperatures, obviating the necessity for the addition of adhesives [65]. Consequently, the bonding between layers is an inherent result of the production process itself, rather than relying on a distinct epoxy matrix. Accordingly, the cohesive interactions between adjacent UHMWPE plies were removed and replaced by tie constraints. The implementation of these constraints ensured full kinematic compatibility between the corresponding surfaces. The laminate was consequently modelled as a fully consolidated structure, in which interply separation and relative sliding were prevented. Consequently, ply-to-ply friction was excluded due to the absence of frictional sliding at tied interfaces. However, the frictional interaction between the projectile and the external laminate surface was retained in order to represent the normal and tangential contact mechanisms acting during impact.

With the exception of the UHMWPE configurations, replacing the composite material also necessitated the interlaminar properties assigned to the cohesive interactions between adjacent plies to be updated. The parameters in question govern the elastic response of the interface, the initiation of delamination, and its subsequent mixed-mode propagation. The interlaminar properties that have been adopted for the relevant composite systems are presented in Table 5.5.

Table 5.5: Interlaminar properties of the cohesive interfaces [64, 112, 115, 117, 119–122].

Composite	**Architecture**	t_n^{max} [MPa]	$t_s^{max} = t_t^{max}$ [MPa]	G_I^c [N/mm]	$G_{II}^c = G_{III}^c$ [N/mm]
T700S	UD	65	75	0.504	1.0
T1000G	UD	50	90	0.277	0.788
AS4/PEEK	UD	80	100	0.969	1.719
Kevlar	UD	30	45	0.4	1.2
Kevlar	Woven	40	55	0.6	2.0
S2-glass	UD	50	60	4	4
S2-glass	Woven	58	58	0.6	1.8

All composite configurations were subjected to an initial projectile velocity of 100 m/s. The resulting residual velocities were documented in Table 5.6, in which the UD T700S laminate is to be regarded as the reference configuration.

Table 5.6: Residual velocity response of the composite systems.

Composite material	**Architecture**	v_r [m/s]	Δv_r [%]
T700S	UD	54.085	–
T1000G	UD	60.902	12.60%
AS4/PEEK	UD	39.260	−27.41%
Kevlar	UD	51.067	−5.58%
Kevlar	Woven	46.130	−14.71%
S2-glass	UD	41.586	−23.11%
S2-glass	Woven	26.621	−50.78%
UHMWPE	UD	50.084	−7.40%
UHMWPE	Woven	−15.695	−129.02%

The results indicate that the ballistic performance of materials is governed by the combined influence of intralaminar strength, interlaminar toughness and reinforcement architecture, rather than by longitudinal strength alone. In the context of the UD carbon-fibre systems, the T1000G demonstrated the highest longitudinal tensile strength ($X_T = 3822$ MPa) and residual velocity (60.902 m/s). The comparatively low interlaminar fracture energies ($G_I^c = 0.277$ N/mm and $G_{II}^c = 0.788$ N/mm) may have promoted earlier delamination and reduced the ability of the plies to sustain load collectively. In contrast, AS4/PEEK exhibited the lowest residual velocity among the UD carbon-fibre systems (39.260 m/s), which is consistent with the enhanced interlaminar toughness provided by its thermoplastic matrix.

The comparison between the UD and woven architectures indicates a consistent advantage for the woven configurations. The residual velocity was found to have decreased from 51.067 to 46.130 m/s for Kevlar and from 41.586 to 26.621 m/s for S2-glass. The interlaced reinforcement has been demonstrated to promote load redistribution in multiple directions and to restrict crack propagation and fibre splitting along a single preferential direction. Consequently, a greater proportion of the laminate contributes to deformation and energy absorption during impact, even when the woven material exhibits a lower longitudinal strength than its UD counterpart.

The woven UHMWPE configuration demonstrated the most favourable response and was the sole system to arrest and rebound the projectile, producing a velocity of $v_r = -15.695$ m/s. In addition to its low density and high in-plane tensile strength, this response was influenced by the tied interply interfaces adopted to represent hot-pressed consolidation. These constraints suppressed ply separation and sliding, allowing the laminate to respond as a continuous structure and promoting membrane-dominated deformation. The resultant effect should therefore be interpreted as the combined effect of the material properties, woven architecture and interface modelling strategy. The findings emphasise that effective composite armour requires an appropriate balance between fibre strength, multidirectional load transfer and resistance to premature interlaminar failure.

5.2 Influence of Geometrical Parameters

5.2.1 Target Plate Diameter

In order to evaluate the influence of the target dimensions on the predicted ballistic response, two additional plate geometries were analysed and compared with the reference diameter of 100 mm. The target diameter was reduced to 80 mm in the first configuration and increased to 120 mm in the second, while all other material, geometrical and numerical parameters were maintained unchanged. This comparison enables the influence of plate size, boundary proximity and stress-wave reflections on the projectile residual velocity to be assessed independently.

All configurations were subjected to an initial projectile velocity of 100 m/s. The resulting residual velocities can be documented in Table 5.7, with the 100 mm target maintained as the reference configuration.

Table 5.7: Residual velocity response for the different target plate diameters.

Target diameter [mm]	v_r [m/s]	Δv_r [%]
80	57.217	5.79%
100	54.085	–
120	51.059	−5.59%

The results suggest a progressive decline in projectile residual velocity as the target diameter increases. It was demonstrated that a reduction in diameter from 100 to 80 mm resulted in an augmentation of v_r from 54.085 to 57.217 m/s, corresponding to a deterioration of 5.79% relative to the reference configuration. Conversely, an increase in diameter to 120 mm resulted in a reduction of the residual velocity to 51.059 m/s, representing an improvement of 5.59%. Within the investigated range, a larger target therefore provided a modest but consistent increase in ballistic resistance.

This trend suggests that increasing the plate diameter allows a wider region of the target to participate in deformation and energy absorption while delaying the interaction of the impact-generated stress waves with the constrained boundary. In the smaller plate, the reduced distance between the impact point and the supports promotes earlier boundary interaction and wave reflection. This may restrict the effective deformation area and decrease the energy dissipated before perforation. However, the limited variation in residual velocity suggests that target diameter exerts a secondary influence in comparison with the material parameters that were previously examined. It is evident that the 100 mm reference geometry therefore provides a reasonable compromise between limiting boundary effects and maintaining computational efficiency.

5.2.2 Projectile Diameter

The influence of projectile dimensions on the ballistic response was evaluated by analysing and comparing two additional hemispherical projectiles with diameters of 12 and 20 mm with the reference diameter of 16 mm. For each configuration, the projectile length was adjusted to maintain the reference mass of 30 g. The material, nose geometry, initial velocity and the remaining numerical parameters were kept constant. Maintaining a constant projectile mass also ensured the preservation of the initial kinetic energy, thereby enabling the assessment of the influence of projectile diameter, contact area and load concentration to be conducted independently of variations in impact energy.

The initial velocity of 100 m/s was assigned to all projectile configurations. The projectile diameters and the corresponding residual velocities were recorded in Table 5.8, with the 16 mm projectile retained as the reference configuration.

Table 5.8: Residual velocity response for the different projectile diameters.

Projectile diameter [mm]	v_r [m/s]	Δv_r [%]
12	69.742	28.95%
16	54.085	–
20	22.057	−59.22%

The results indicate a significant decrease in residual velocity as the projectile diameter increases. Reducing the diameter from 16 to 12 mm increased v_r from 54.085 to 69.742 m/s, corresponding to a deterioration of 28.95% relative to the reference case. Conversely, increasing the diameter to 20 mm reduced the residual velocity to 22.057 m/s, representing an improvement of 59.22%. Projectile diameter therefore exhibited a substantially greater influence on the predicted ballistic response than the target-diameter variations examined previously.

Given that projectile mass and initial kinetic energy were maintained constant, this behaviour can be primarily associated with the change in contact area and load distribution. The smaller projectile concentrates the impact force over a reduced area, generating higher local stresses and promoting localised penetration with limited engagement of the surrounding target material. Conversely, the larger projectile distributes the load over a more extensive region, mobilising a greater volume of the aluminium and composite layers and increasing the contribution of bending, membrane deformation and distributed damage to energy absorption.

5.2.3 Aluminium and Composite Layers Thickness

The influence of the aluminium- and composite-layer thicknesses was investigated through two complementary parametric campaigns. In the initial campaign, the total target thickness was maintained at 2.4 mm, thereby enabling the distribution of material through the thickness to be varied without altering the overall target thickness. The aluminium thickness was the first variable to be modified, with the composite contribution being adjusted accordingly. The procedure facilitated the examination of the effects of aluminium content, composite content and ply discretisation as discrete variables.

In the second campaign, the total target thickness was permitted to vary. The aluminium thickness was increased while retaining eight composite plies with an individual thickness of 0.1 mm. Conversely, an increase in composite thickness was observed when the number of 0.1 mm plies was altered, while maintaining the two aluminium layers at 0.8 mm each. All remaining material, geometrical and numerical parameters were kept unchanged. The complete set of configurations and the corresponding residual-velocity results are summarised in Table 5.9, with the original 2.4 mm laminate retained as the reference case.

Table 5.9: Layer-thickness configurations and corresponding residual-velocity response.

t_{total} [mm]	t_{Al} [mm]	t_{C} [mm]	Al layers [mm]	Composite plies [mm]	v_{r} [m/s]	Δv_{r} [%]
2.4	1.6	0.8	2×0.8	8×0.1	54.085	–
2.4	2.0	0.4	2×1.0	4×0.1	38.207	−29.36%
2.4	1.0	1.4	2×0.5	14×0.1	66.826	23.56%
3.8	3.0	0.8	2×1.5	8×0.1	−14.043	−125.96%
4.8	4.0	0.8	2×2.0	8×0.1	−32.316	−159.75%
3.2	1.6	1.6	2×0.8	16×0.1	37.084	−31.43%
3.8	1.6	2.2	2×0.8	22×0.1	29.509	−45.44%
4.8	1.6	3.2	2×0.8	32×0.1	−2.623	−104.85%

The results indicate that the ballistic response is influenced not solely by the total thickness of the target, but also by the relative proportions of aluminium and composite material. In the case of constant-thickness configurations ($t_{\text{total}} = 2.4$ mm), a reduction in the total aluminium thickness from 1.6 to 1.0 mm and an increase in the composite thickness from 0.8 to 1.4 mm was observed to result in an enhancement of the residual velocity from 54.085 to 66.826 m/s. This is indicative of a deterioration of 23.56% relative to the reference laminate. In contrast, an augmentation in the aluminium thickness to 2.0 mm, coupled with a diminution in the composite thickness to 0.4 mm, has been demonstrated to result in a reduction of the residual velocity to 38.207 m/s, representing an improvement of 29.36%. Therefore, for the material system and impact conditions under consideration, the redistribution of a constant total thickness in favour of aluminium resulted in a significantly increased resistance to continued penetration.

The configuration, which contained 3.0 mm of aluminium and 0.8 mm of composite, arrested and rebounded the projectile, thereby producing a velocity of $v_r = -14.043$ m/s. In contrast, the configuration containing 1.6 mm of aluminium and 2.2 mm of composite was perforated with a positive residual velocity of 29.509 m/s. A comparable discrepancy was observed at a total of $t_{\text{total}} = 4.8$ mm. It was observed that both targets were capable of preventing perforation. However, the aluminium-dominated laminate produced a rebound velocity of -32.316 m/s, whereas the composite-dominated laminate resulted in a considerably smaller rebound velocity of -2.623 m/s. Consequently, an augmentation in aluminium thickness proved to be a more efficacious strategy for enhancing the stopping response when compared with an equivalent increase in composite thickness.

This behaviour is consistent with the different deformation and failure mechanisms represented by the two materials. The dissipation of energy by the aluminium layers is attributable to extensive plastic deformation, strain hardening and ductile fracture. Increasing their thickness has been shown to strongly increase the bending stiffness of the metallic contribution and to enlarge the volume of material available for plastic energy dissipation. This, in turn, has been demonstrated to delay the initiation and propagation of local plugging, tearing and petalling. A thicker aluminium section can also distribute the contact load over a wider region of the laminate before severe local failure develops.

Increasing the composite thickness provides additional material for fibre-dominated load carrying, matrix deformation and membrane action. However, in the investigated configurations, this benefit was less pronounced than that obtained by increasing the aluminium thickness. The use of a greater number of 0.1 mm plies also introduces additional interfaces at which cohesive damage and delamination may develop. In cases where the aluminium layers are comparatively thin, the highly localised impact load is transferred to the composite before a sufficiently wide deformation field is established. The resultant matrix damage, fibre failure and progressive delamination can limit the proportion of the composite thickness that is effectively mobilised during the short impact event. This interpretation should be regarded as a mechanism-based explanation of the residual-velocity trend and should be confirmed through comparison of the corresponding damage and energy histories.

The results obtained demonstrate that the aluminium layers are the primary factor contributing to the penetration resistance of the laminate under investigation, and this is independent of the projectile geometry and impact velocity. The composite retains its significance as a secondary load-bearing and containment component. However, increasing its thickness alone does not yield the same enhancement in residual velocity as increasing the aluminium thickness. Consequently, a design intended to maximise stopping capability should retain sufficient metallic thickness to promote distributed plastic deformation before the composite is subjected to severe local loading. However, aluminium-dominated configurations also possess a greater Areal Weight Density (AWD), owing to the fact that aluminium possesses a higher density than the composite. Consequently, the apparent superiority of the former should be interpreted in terms of ballistic performance when comparing equivalent total thickness, and not as mass efficiency.

5.3 Influence of Ply Orientation

The influence of ply orientation on the ballistic response of the hybrid laminate was investigated by comparing several stacking sequences with the original $[0/90]$ configuration. The alternative arrangements considered were $[0/90]_{2s}$, $[45/-45]$, $[0/45/90/-45]$, $[0/0/90/90]$ and $[0/0/0/0/90/90/90/90]$. The selection of these configurations was made for the purpose of evaluating the impact of the distribution of fibre directions on the in-plane stiffness, the load redistribution, and the development of fibre and matrix damage during impact.

The $[0/0/90/90]$ and $[0/0/0/0/90/90/90/90]$ arrangements represent clustered stacking sequences, in which consecutive plies with the same orientation form directional blocks within the laminate. This phenomenon, commonly referred to as ply clustering, modifies the through-thickness distribution of stiffness and interlaminar stresses, as well as the number and position of interfaces at which the fibre orientation changes. In the present model, cohesive interactions remained defined between every pair of adjacent plies, including interfaces between plies with the same fibre orientation, allowing interlaminar damage to develop throughout the laminate. Consequently, the response of the clustered configurations reflects the combined influence of fibre-

orientation distribution and cohesive-interface arrangement on load transfer and damage propagation [123].

For each configuration, the material properties, total composite thickness, aluminium layers, target dimensions, boundary conditions and impact conditions were maintained unchanged. Consequently, any variation in projectile residual velocity can be attributed primarily to the modification of the composite stacking sequence. All configurations were subjected to an initial projectile velocity of 100 m/s, and the original $[0/90]$ arrangement was retained as the reference case. The resulting residual velocities can be recorded in Table 5.10.

Table 5.10: Residual velocity response for the different composite stacking sequences.

Stacking sequence	v_r **[m/s]**	Δv_r **[%]**
$[0/90]$ (reference)	54.085	–
$[0/90]_{2s}$	54.241	0.29%
$[45/-45]$	54.015	−0.13%
$[0/45/90/-45]$	54.657	1.06%
$[0/0/90/90]$	54.994	1.68%
$[0/0/0/0/90/90/90/90]$	56.322	4.14%

The results suggest that the composite stacking sequence and ply clustering exert only a limited influence on projectile residual velocity when compared with the effects of material selection and layer-thickness distribution previously examined. In relation to the reference $[0/90]$ configuration, the variations in v_r ranged from -0.13% to 4.14%. All configurations therefore produced equivalent outcomes of complete perforation and exhibited comparable ballistic responses under the investigated impact conditions.

The alteration of the orthogonal $[0/90]$ configuration to the angled $[45/-45]$ sequence yielded the lowest residual velocity, although this reduction was only 0.13%. This near-identical response was expected from the rotational symmetry of the target geometry, boundary conditions and central impact loading, since rotating all ply orientations by 45° produces an equivalent physical configuration. The agreement therefore supports the numerical consistency and soundness of the model. In addition, the symmetric $[0/90]_{2s}$ and multidirectional $[0/45/90/-45]$ arrangements increased the residual velocity by only 0.29% and 1.06%, respectively. These results indicate that, at an initial velocity of 100 m/s, the response is predominantly governed by localised contact, through-thickness damage and perforation mechanisms. This suggests that the influence of changes in global in-plane stiffness and directional load redistribution is limited.

A more noticeable, although still modest, reduction in ballistic performance was observed as plies with the same orientation were progressively clustered. The $[0/0/90/90]$ sequence resulted in an increase in the residual velocity of 1.68%, while the fully clustered $[0/0/0/0/90/90/90/90]$ configuration produced the highest value, 56.322 m/s, corresponding to an increase of 4.14%. In the latter configuration, the orientation change is concentrated at the central $0^\circ/90^\circ$ interface rather than being distributed through the laminate. This configuration has the potential to induce

elevated levels of interlaminar stresses and more localised delamination at the principal orientation transition, thereby diminishing the capacity of the plies to collectively redistribute the impact load. This interpretation is consistent with the reported influence of ply clustering on damage development in composite laminates [123].

Overall, the stacking-sequence study demonstrate that fibre orientation is a secondary parameter for the ballistic configuration under consideration. The selection of materials and the relative thicknesses of the metallic and composite constituents provide substantially greater changes in residual velocity. It is therefore recommended that these should remain the primary variables in the optimisation of stopping capability. Alternatively, the stacking sequence may be selected to satisfy additional structural requirements, including in-plane stiffness, coupling behaviour, fatigue resistance and damage tolerance, provided that excessive ply clustering is avoided.

5.4 Proposed Hybrid Configuration

Following the parametric investigations presented throughout this chapter, a new hybrid configuration was proposed by combining the materials that yielded the most favourable ballistic responses in Section 5.1. The most significant reductions in projectile residual velocity were observed when aluminium 7075-T6 and woven UHMWPE were independently introduced into the reference model. Consequently, the combination was selected as the most promising basis for enhancing the ballistic resistance of the target.

The material selection process also took into account the structural mass of the components. Aluminium 7075-T6 is characterised by a high strength-to-density ratio of approximately 2810 $\mathrm{kg/m^3}$, in contrast to the considerably lower density of approximately 970 $\mathrm{kg/m^3}$ exhibited by UHMWPE. The low density of UHMWPE can therefore partially compensate for the mass associated with the higher-strength aluminium alloy.

Although aluminium 7075-T6 and woven UHMWPE exhibited the most favourable individual responses, the mass-efficiency assessment was not restricted to this combination. The additional aluminium alloys and composite systems included in the comparison were selected because they also demonstrated comparatively good ballistic performance when evaluated independently in the material-selection study. Their inclusion enables alternative material combinations to be assessed and determines whether a more favourable balance between ballistic resistance and structural mass can be achieved without relying exclusively on the individually best-performing constituents.

In order to quantify the mass efficiency of each laminate independently of the target area, the AWD was calculated. This parameter is indicative of the mass per unit surface area of the laminate, thus providing a suitable foundation for the comparison of configurations composed of materials with varying densities and layer thicknesses. The AWD of a laminate comprising aluminium and composite layers is determined by the following equation,

$$AWD = \rho_{\mathrm{Al}} t_{\mathrm{Al}} + \rho_{\mathrm{comp}} t_{\mathrm{comp}} \tag{5.1}$$

where ρ_{Al} and ρ_{comp} are the aluminium and composite densities, respectively, and t_{Al} and t_{comp} are their corresponding total thicknesses through the laminate. All configurations included in this comparison were assigned a total aluminium thickness of 1.6 mm and a total composite thickness of 0.8 mm. These thicknesses correspond to the sum of the individual layers of each material and were converted to metres when calculating AWD in kg/m^2. The values obtained for the investigated configurations can be summarised in Table 5.11.

Table 5.11: AWD of the investigated hybrid configurations.

Configuration	ρ_{Al} $[kg/m^3]$	ρ_{comp} $[kg/m^3]$	AWD $[kg/m^2]$
Reference: 2024-T3/T700S	2750	1570	5.656
7075-T6/Kevlar	2810	1440	5.648
5052-H32/Kevlar	2680	1440	5.440
AlSi10Mg/Kevlar	2700	1440	5.472
7075-T6/UHMWPE	2810	970	5.272
5052-H32/UHMWPE	2680	970	5.064
AlSi10Mg/UHMWPE	2700	970	5.096

The comparison of the calculated AWD reveals that the 5052-H32/UHMWPE laminate is the lightest candidate, with an AWD of 5.064 kg/m^2. The 7075-T6/UHMWPE configuration presents a slightly higher value of 5.272 kg/m^2, corresponding to an increase of only 0.208 kg/m^2, or approximately 4.11%. In consideration of the negligible disparity between these values, the selection of the final configuration was not deemed to be adequately determined by real weight density alone. The two laminates were thus subjected to a simulation under conditions of identical impact velocity, with the initial velocity of the projectile set at 100 m/s. The residual velocities of the laminates were then compared in order to ascertain which configuration offered superior ballistic resistance. It was observed that both configurations arrested and rebounded the projectile. However, the 7075-T6/UHMWPE laminate exhibited a residual velocity of approximately -34 m/s, in comparison to approximately -23 m/s for the 5052-H32/UHMWPE laminate. Consequently, the magnitude of the rebound velocity increased by approximately 47.83% when 5052-H32 was substituted by 7075-T6. Although rebound velocity should not be interpreted as a standalone measure of ballistic resistance, the greater reversal of projectile motion indicates that the 7075-T6/UHMWPE laminate provides a higher stopping margin under the investigated impact conditions. In addition, the proposed laminate has an AWD approximately 6.79% lower than that of the reference laminate.

On this basis, the 7075-T6/UHMWPE laminate was selected as the proposed hybrid configuration. Its ballistic response was subsequently evaluated using the same modelling assumptions and impact conditions adopted for the reference CARALL2/1 configuration. Figure 5.1 presents the initial-residual velocity curve obtained for the proposed laminate.

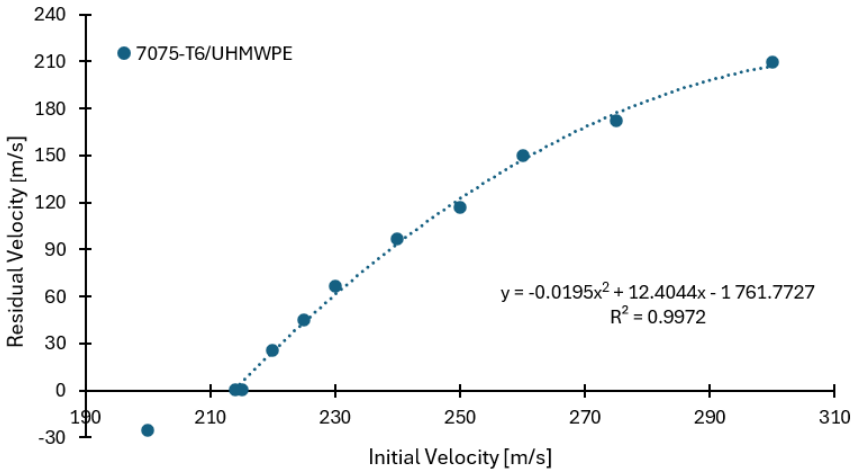


Figure 5.1: Initial-residual velocity curve for 7075-T6/UHMWPE configuration.

The ballistic-limit velocity of the proposed 7075-T6/UHMWPE laminate was estimated at approximately 214 m/s by applying the Lambert-Jonas correlation in Equation 4.7 to the numerical results presented in Figure 5.1. For a consistent comparison, this value is assessed against the numerical ballistic limit of the reference 2024-T3/T700S CARALL2/1 laminate subjected to hemispherical impact, which was 80.756 m/s in Chapter 4 (Table 4.7). The proposed configuration therefore increases the predicted ballistic limit by approximately 132.2 m/s, corresponding to a remarkable improvement of approximately 164% over the reference laminate.

This improvement is achieved without increasing the total panel thickness, which remains 2.4 mm, with 1.6 mm of aluminium and 0.8 mm of composite. Furthermore, the AWD decreases from 5.656 to 5.272 kg/m^2, representing a reduction of approximately 6.79% and an equivalent reduction in panel mass for the same target area. The proposed laminate thus combines a substantially higher predicted perforation threshold with a lower structural mass, providing a more favourable balance between ballistic resistance and weight than the original configuration. These results support the selection of 7075-T6 and woven UHMWPE as a promising material combination within the investigated numerical framework.

Chapter 6

Conclusions

This dissertation investigated the numerical modelling of hybrid aluminium/composite laminates subjected to ballistic impact, with the aim of supporting the conceptual development of protection systems. A three-dimensional modelling approach was developed in Abaqus/Explicit, combining the J-C plasticity for the metallic layers and damage models with a strain-rate-dependent Hashin formulation implemented in a VUMAT for the composite. In the latter, progressive stiffness degradation and cohesive interfaces enabled intralaminar and interlaminar damage to be modelled within a single numerical model.

An important aspect of the methodology was the independent calibration of the constituent material models before their application to the hybrid target using experimental results from the literature [99]. This approach separated the adjustment of selected aluminium and composite parameters from the assessment of the complete laminate. Calibration sought a near-zero final projectile velocity when the experimental ballistic limit was imposed as the initial velocity. In this context, selected parameters of the aluminium and composite material models were calibrated to obtain an approximately zero residual projectile velocity. The subsequent comparison of the hybrid model with published experimental results [65] revealed the model's overall good performance. Agreement was closer for the hemispherical and sharp projectiles than for the flat projectile. The examination of composite damage state-dependent variables and aluminium equivalent plastic strain complemented the assessment based on projectile velocity. The composite contours showed more spatially extensive damage under the flat projectile, whereas fibre damage was more concentrated around the penetration region for the hemispherical and sharp projectiles. The aluminium analysis distinguished perimeter-controlled plugging from more distributed stretching and local tearing with petal formation. These observations emphasise that the constituents can develop different deformation and failure mechanisms during the same impact event. They also demonstrate the importance of considering the spatial distribution of damage rather than relying exclusively on maximum values. Neither local damage nor equivalent plastic strain alone is sufficient to establish the energy absorbed by the target.

The parametric investigation broadened the study beyond the reference carbon-fibre/aluminium laminate by examining material selection, geometrical parameters and ply orientation. Within the

configurations considered, it was verified that material selection, projectile diameter, and the relative thicknesses of the constituents influenced the ballistic response more strongly than changes in stacking sequence and target diameter. This finding supports prioritising the combination and distribution of materials during conceptual design, while retaining fibre orientation as a variable relevant to other structural requirements. The numerical comparisons also highlighted that ballistic performance cannot be inferred from a single material property, such as longitudinal strength, without considering the complete constitutive response and the representation of the interfaces.

The best hybrid configuration combined aluminium 7075-T6 with woven UHMWPE, bringing together the constituents that exhibited the most favourable responses in the parametric study. The selection also considered alternative combinations of aluminium alloys and composite materials through an assessment of their areal density at constant layer thicknesses. This stage of the study translated the individual parametric comparisons into a specific protection concept, demonstrating the value of assessing material combinations in terms of both ballistic response and mass rather than selecting constituents solely on the basis of their individual performance. Although the 5052-H32/UHMWPE laminate was the lightest candidate, the 7075- T6/UHMWPE configuration was selected based on both areal density and material properties. The low density of the UHMWPE allowed the proposed laminate to achieve a lower areal density than the reference CARALL2/1 target.

Overall, the main contribution of this dissertation is a structured numerical methodology linking constituent calibration, hybrid-target assessment and parametric comparison. The work provides a basis for investigating the relationship between projectile geometry, material behaviour and damage development in hybrid laminates. Its application is most appropriate to the screening of protection concepts, with further experimental evidence and model refinement required before detailed design or aircraft integration.

6.1 Future Work

Future work could build on the present investigation by addressing the following aspects:

- Improve the agreement between numerical predictions and experimental results for the flat projectile configuration. Particular attention should be given to the influence of friction effects and their representation in the numerical model, given their relevance to this impact case;
- Assess the applicability of the adopted intralaminar formulation to woven reinforcements through a dedicated investigation. This assessment should establish whether the formulation adequately represents their response, rather than relying on direct extrapolation from the unidirectional reference composite;
- Conduct an experimental assessment of the proposed hybrid configuration to compare its measured ballistic response with the numerical predictions. This comparison would help confirm the suitability of the proposed model for the selected combination of materials;

- Investigate the possibility of combining unidirectional UHMWPE with woven reinforcement within the composite component of the hybrid panel. This would extend the material configuration study to assess the ballistic response of a laminate incorporating both reinforcement architectures;
- Develop a numerical model capable of evaluating the residual stiffness and strength of panels after impact damage. The resulting assessment of their remaining load-bearing capacity would support the definition of damage tolerance requirements and inform preventive maintenance interventions;
- Extend the study to include oblique and multiple impacts, deformable projectiles, and alternative environmental conditions. Considering these additional conditions would broaden the scope of the simulations and bring the numerical assessment closer to operational loading scenarios.

References

[1] United Nations. *The 17 Goals: Sustainable Development*. United Nations Department of Economic and Social Affairs. 2015. URL: https://sdgs.un.org/goals (visited on 08/18/2025).

[2] Aerospace Technology Institute. *Composite Material Applications in Aerospace*. Insight Report 09. Aerospace Technology Institute, 2018, pp. 1–12. URL: https://www.ati.org.uk/wp-content/uploads/2021/08/insight_9-composites_amended-2018-09-20.pdf.

[3] Charles E. Harris, Jr. James H. Starnes, and Mark J. Shuart. "Design and Manufacturing of Aerospace Composite Structures: State-of-the-Art Assessment". In: *Journal of Aircraft* 39.4 (July 2002), pp. 545–560. DOI: 10.2514/2.2992.

[4] Muhammad Bilal Afzal. "Modeling of Damage Evolution of Fiber-Reinforced Composite Structure". In: *Safety and Risk Assessment of Civil Aircraft during Operation*. Ed. by Longbiao Li. London, UK: IntechOpen, Dec. 23, 2020. ISBN: 978-1-78984-792-5. DOI: 10.5772/intechopen.93323. URL: https://www.intechopen.com/chapters/73524.

[5] Kanchan Biswas. "Military Airworthiness and Certification Procedures: Global Scenario". In: *Proceedings of the International Conference on Modern Research in Aerospace Engineering*. Ed. by Sanjay Singh, Pushkar Raj, and Samir Tambe. Lecture Notes in Mechanical Engineering. Singapore: Springer, 2018, pp. 315–331. DOI: 10.1007/978-981-10-5849-3_31.

[6] United States Air Force. *A-10C Thunderbolt II*. United States Air Force. 2024. URL: https://www.af.mil/About-Us/Fact-Sheets/Display/Article/104490/a-10c-thunderbolt-ii/.

[7] Zhiyong Li et al. "Ballistic Penetration Damage for Hybrid Carbon/Kevlar/UHMWPE Fiber Laminated Composites: Experimental and Numerical Techniques". In: *Composite Structures* 316 (2023), p. 117037. ISSN: 0263-8223. DOI: 10.1016/j.compstruct.2023.117037.

[8] L. Peng et al. "Investigations of the Ballistic Response of Hybrid Composite Laminated Structures". In: *Composite Structures* 282 (2022), p. 115019. ISSN: 0263-8223. DOI: 10.1016/j.compstruct.2021.115019.

[9] K. Bilisik et al. "Advances in Ballistic Protection". In: *Functional and Technical Textiles*. Ed. by S. Maity, K. Singha, and P. Pandit. The Textile Institute Book Series. Woodhead Publishing, 2023. Chap. 3, pp. 71–139. ISBN: 978-0-323-91593-9. DOI: 10.1016/B978-0-323-91593-9.00023-7. URL: https://www.sciencedirect.com/science/article/pii/B9780323915939000237.

[10] Yusif Tanriverdiyev. “Classification and properties of composites based on matrix material”. In: *World Journal of Advanced Research and Reviews* 24.2 (2024), pp. 2278–2282. DOI: 10.30574/wjarr.2024.24.2.3608.

[11] Deborah D. L. Chung. *Composite Materials: Functional Materials for Modern Technologies*. Engineering Materials and Processes. London: Springer, 2003. ISBN: 978-1-4471-3734-4. DOI: 10.1007/978-1-4471-3732-0.

[12] Theodore J. Reinhart. “Overview of Composite Materials”. In: *Handbook of Composites*. Ed. by S. T. Peters. 2nd ed. Boston, MA: Springer, 1998, pp. 21–33. ISBN: 978-1-4615-6389-1. DOI: 10.1007/978-1-4615-6389-1_2.

[13] Krishan Kumar Chawla. “Strength, Fracture, Fatigue, and Design”. In: *Composite Materials: Science and Engineering*. Materials Research and Engineering. New York, NY: Springer, 1987, pp. 229–258. DOI: 10.1007/978-1-4757-3912-1_12.

[14] Veis Šerifi et al. “Historical Development of Composite Materials”. In: *The Annals of the University of Oradea, Fascicle of Management and Technological Engineering* 27.3 (2018), pp. 1–8. DOI: 10.15660/AUOFMTE.2018-3.3392.

[15] Sina AhmadvashAghbash et al. “Methods and Models for Fibre–Matrix Interface Characterisation in Fibre-Reinforced Polymers: A Review”. In: *International Materials Reviews* 68.8 (2023), pp. 1245–1319. DOI: 10.1080/09506608.2023.2265701.

[16] P. K. Mallick. *Fiber-Reinforced Composites: Materials, Manufacturing, and Design*. 3rd ed. Boca Raton, FL: CRC Press, 2007. ISBN: 978-0-8493-4205-9. DOI: 10.1201/9781420005981.

[17] Derek Hull and T. W. Clyne. “Preface to Second Edition”. In: *An Introduction to Composite Materials*. 2nd ed. Cambridge Solid State Science Series. Cambridge: Cambridge University Press, 1996, pp. xiv–xvi. DOI: 10.1017/CBO9781139170130.

[18] U.S. Congress, Office of Technology Assessment. “Polymer Matrix Composites”. In: *Advanced Materials by Design*. Report No. OTA-E-351. 1988, pp. 71–95. URL: https://www.princeton.edu/~ota/disk2/1988/8801/880106.PDF.

[19] F. C. Campbell. “Thermoset Resins: The Glue That Holds the Strings Together”. In: *Manufacturing Processes for Advanced Composites*. Ed. by F. C. Campbell. Amsterdam: Elsevier Science, 2004, pp. 63–101. ISBN: 978-1-85617-415-2. DOI: 10.1016/B978-185617415-2/50004-6. URL: https://www.sciencedirect.com/science/article/pii/B9781856174152500046.

[20] Hari Madhav, Neetika Singh, and Gautam Jaiswar. “Thermoset, Bioactive, Metal–Polymer Composites for Medical Applications”. In: *Materials for Biomedical Engineering: Thermoset and Thermoplastic Polymers*. Ed. by Valentina Grumezescu and Alexandru Mihai Grumezescu. Elsevier, 2019. Chap. 4, pp. 105–143. ISBN: 978-0-12-816874-5. DOI: 10.1016/B978-0-12-816874-5.00004-9.

[21] Arun Kumar Sharma et al. “Matrix Materials Used in Composites: A Comprehensive Study”. In: *Materials Today: Proceedings* 21 (2020), pp. 1559–1562. DOI: 10.1016/j.matpr.2019.11.086.

[22] Deepak Verma et al. “Coir Fibre Reinforcement and Application in Polymer Composites: A Review”. In: *Journal of Materials and Environmental Science* 4.2 (2013). Received 13 September 2012; revised 15 October 2012; accepted 15 October 2012, pp. 263–276.

[23] Saira Taj, Munawar Ali Munawar, and Shafi Ullah Khan. "Natural Fiber-Reinforced Polymer Composites". In: *Proceedings of the Pakistan Academy of Sciences* 44.2 (2007), pp. 129–144.

[24] Krishan K. Chawla. "Carbon Fiber/Carbon Matrix Composites". In: *Composite Materials: Science and Engineering*. 4th ed. Cham: Springer International Publishing, 2019, pp. 297–311. ISBN: 978-3-030-28983-6. DOI: 10.1007/978-3-030-28983-6_8.

[25] Przemyslaw D. Pastuszak and Aleksander Muc. "Application of Composite Materials in Modern Constructions". In: *Key Engineering Materials* 542 (2013), pp. 119–129. DOI: 10.4028/www.scientific.net/KEM.542.119.

[26] Horse Construction. *Benefits of Carbon Fiber for Structural Reinforcement*. 2025. URL: https://www.horseen.com/solution/benefits-carbon-fiber-structural-reinforcement (visited on 08/24/2026).

[27] Hamid Khayyam et al. "PAN Precursor Fabrication, Applications and Thermal Stabilization Process in Carbon Fiber Production: Experimental and Mathematical Modelling". In: *Progress in Materials Science* 107 (2020), p. 100575. DOI: 10.1016/j.pmatsci.2019.100575.

[28] Sayed Abolfazl Mirdehghan. "Fibrous Polymeric Composites". In: *Engineered Polymeric Fibrous Materials*. Ed. by Masoud Latifi. The Textile Institute Book Series. Woodhead Publishing, 2021, pp. 1–58. ISBN: 978-0-12-824381-7. DOI: 10.1016/B978-0-12-824381-7.00012-3.

[29] R. D. S. G. Campilho. *Natural Fiber Composites*. Boca Raton, FL: CRC Press, 2015. ISBN: 978-1-4822-3900-5. DOI: 10.1201/b19062.

[30] A. Abbadi et al. "Modelling the Fatigue Behaviour of Composites Honeycomb Materials (Aluminium/Aramide Fibre Core) Using Four-Point Bending Tests". In: *International Journal of Fatigue* 32.11 (2010), pp. 1739–1747. DOI: 10.1016/j.ijfatigue.2010.01.005.

[31] S. Bourbigot and X. Flambard. "Heat Resistance and Flammability of High Performance Fibres: A Review". In: *Fire and Materials* 26.4-5 (2002), pp. 155–168. DOI: 10.1002/fam.799.

[32] C. Y. Yue, G. X. Sui, and H. C. Looi. "Effects of Heat Treatment on the Mechanical Properties of Kevlar-29 Fibre". In: *Composites Science and Technology* 60.3 (2000), pp. 421–427. DOI: 10.1016/S0266-3538(99)00137-2.

[33] A. Abbadi et al. "Experimental Study on the Fatigue Behaviour of Honeycomb Sandwich Panels with Artificial Defects". In: *Composite Structures* 120 (2015), pp. 394–405. DOI: 10.1016/j.compstruct.2014.10.020.

[34] P. J. Lemstra and B. J. Lommerts. "Polyethylene vs. Para-Aramid Fibers". In: *Chemical Fibers International* 71.4 (2021), p. 160.

[35] I. G. Crouch, J. Sandlin, and S. Thomas. "Polymers and Fibre-Reinforced Plastics". In: *The Science of Armour Materials*. Ed. by I. G. Crouch. Cambridge, UK: Woodhead Publishing, 2016. Chap. 5, pp. 203–268. ISBN: 978-0-08-100704-4. DOI: 10.1016/B978-0-08-100704-4.00005-0.

[36] A. K. Rana, A. Mandal, and S. Bandyopadhyay. "Short Jute Fiber Reinforced Polypropylene Composites: Effect of Compatibiliser, Impact Modifier and Fiber Loading". In: *Composites Science and Technology* 63.6 (2003), pp. 801–806. DOI: 10.1016/S0266-3538(02)00267-1.

[37] T. Gurunathan, S. Mohanty, and S. K. Nayak. “A Review of the Recent Developments in Biocomposites Based on Natural Fibres and Their Application Perspectives”. In: *Composites Part A: Applied Science and Manufacturing* 77 (2015), pp. 1–25. DOI: 10.1016/j.compositesa.2015.06.007.

[38] Krishan K. Chawla. *Composite Materials: Science and Engineering*. 4th ed. Cham: Springer, 2021. ISBN: 978-3-030-51592-4. DOI: 10.1007/978-3-030-51593-1.

[39] Roberta Paye Bara. *Processos, Materiais Compósitos e Meio Ambiente*. Seleção de Materiais Mecânicos, Unidade 4. Ead.br. 2020. URL: https://catalogcdns3.ulife.com.br/content-cli/ENG_SEMECA_20/unidade_4/ebook/index.html.

[40] Ian G. Crouch, ed. *The Science of Armour Materials*. 1st ed. Woodhead Publishing in Materials. Cambridge, UK: Woodhead Publishing, 2016. ISBN: 978-0-08-100704-4.

[41] Hamza El Etri et al. “A State-of-the-Art Review on Mechanical Characteristics of Different Fiber Metal Laminates for Aerospace and Structural Applications”. In: *The International Journal of Advanced Manufacturing Technology* 123.9-10 (2022), pp. 2965–2991. DOI: 10.1007/s00170-022-10277-1.

[42] Robert M. Jones. *Mechanics of Composite Materials*. 2nd ed. Taylor & Francis, 1999. DOI: 10.1201/9781498711067.

[43] Louis F. Vosteen and Richard N. Hadcock. *Composite Chronicles: A Study of the Lessons Learned in the Development, Production, and Service of Composite Structures*. NASA Contractor Report NASA-CR-4620. National Aeronautics and Space Administration, Nov. 1994. URL: https://ntrs.nasa.gov/citations/19950010444.

[44] Embraer. *Defesa & Segurança: C-390 Millennium*. Embraer. 2024. URL: https://defense.embraer.com/pt/air/c-390/.

[45] Aernnova. *Embraer Programs*. Aernnova Aerospace. 2024. URL: https://www.aernnova.com/en/programs-and-products/embraer-programs/.

[46] Mehmet Burak Şenol. “Evaluation and Prioritization of Technical and Operational Airworthiness Factors for Flight Safety”. In: *Aircraft Engineering and Aerospace Technology* 92.7 (2020), pp. 1049–1061. DOI: 10.1108/AEAT-03-2020-0058.

[47] Leon Purton and Kyriakos Kourousis. “Military Airworthiness Management Frameworks: A Critical Review”. In: *Proceedings of the 3rd International Symposium on Aircraft Airworthiness*. 3rd International Symposium on Aircraft Airworthiness. Sir Lawrence Wackett Aerospace Research Centre, RMIT University and Airworthiness Technologies Research Center, Beihang University/NLAA. Melbourne, Australia, 2013.

[48] European Defence Agency. *European Military Airworthiness Requirement EMAR M: Continuing Airworthiness Management*. Military Airworthiness Authorities Forum. 2018. URL: https://eda.europa.eu/experts/airworthiness/mawa-documents.

[49] European Defence Agency. *European Military Airworthiness*. European Defence Agency. 2013. URL: https://eda.europa.eu/experts/airworthiness.

[50] European Defence Agency. *European Military Airworthiness Document–Recognition (EMAD R)*. Official Publication. European Defence Agency, 2013. URL: https://eda.europa.eu/experts/airworthiness/mawa-documents.

[51] European Defence Agency. *Introduction to the Military Airworthiness Framework*. Official Publication. European Defence Agency, 2017. URL: https://eda.europa.eu/experts/airworthiness/mawa-documents.

[52] European Defence Agency. *EMAR 21: Certification of Military Aircraft and Related Products, Parts and Appliances, and Design and Production Organisation Approval*. European Military Airworthiness Requirement. European Defence Agency, 2018. URL: https://eda.europa.eu/experts/airworthiness/mawa-documents.

[53] UK Ministry of Defence. *RA 1010: Head of Establishment Aviation Responsibilities and Aviation Duty Holder/Accountable Manager (Military Flying) Establishment Responsibilities*. Regulatory Article RA 1010. Military Aviation Authority, Nov. 30, 2020. URL: https://www.gov.uk/government/publications/regulatory-article-ra-1010-head-of-establishment-aviation-responsibilities.

[54] Jilian Guo, Kangming Bai, and Lintong Jia. "Research on Airworthiness Management System about Military Aircraft Development". In: *Procedia Engineering* 17 (2011), pp. 375–381. DOI: 10.1016/j.proeng.2011.10.043.

[55] U.S. Department of Defense. *DoD Airworthiness Policy*. DoD Instruction DoDI 5030.61. U.S. Department of Defense, Dec. 3, 2024. URL: https://www.esd.whs.mil/Portals/54/Documents/DD/issuances/dodi/503061p.PDF.

[56] Jeffrey C. King. "Utilizing Model Based Systems Engineering to Identify Safety Critical Functions in Airworthiness Certification". AFIT-ENV-MS-21-M-241. MA thesis. Wright-Patterson Air Force Base, OH: Air Force Institute of Technology, Mar. 2021. URL: https://scholar.afit.edu/etd/4949/.

[57] Federal Aviation Administration. *Airworthiness Certification of Aircraft and Related Products*. FAA Order 8130.2G. U.S. Department of Transportation, Federal Aviation Administration, Aug. 31, 2010. URL: https://www.faa.gov/documentLibrary/media/Order/8130.2G.pdf.

[58] Department of the Air Force. *Department of the Air Force Guidance Memorandum to Department of the Air Force Instruction 62-601, Airworthiness*. Guidance Memorandum. Department of the Air Force, Apr. 2025. URL: https://www.e-publishing.af.mil/.

[59] U.S. Department of Defense. *MIL-STD-662F: V_{50} Ballistic Test for Armor*. Test Method Standard MIL-STD-662F. Supersedes MIL-STD-662E, dated 22 January 1987. U.S. Department of Defense, Dec. 18, 1997. URL: https://quicksearch.dla.mil/qsSearch.aspx.

[60] Lijing Wang et al. "Recent Trends in Ballistic Protection". In: *Textiles and Light Industrial Science and Technology* 3 (2014), pp. 37–47. DOI: 10.14355/tlist.2014.03.007. URL: https://research-repository.rmit.edu.au/articles/journal_contribution/Recent_trends_in_ballistic_protection/27466683.

[61] Özlenen Erdem İşmal and Roshan Paul. "Composite Textiles in High-Performance Apparel". In: *High Performance Apparel: Materials, Development, and Applications*. Ed. by John McLoughlin and Tasneem Sabir. Cambridge, UK: Woodhead Publishing, 2018. Chap. 17, pp. 377–420. DOI: 10.1016/B978-0-08-100904-8.00019-5.

[62] N. K. Naik. "Ballistic Impact Behaviour of Composites: Analytical Formulation". In: *Composites Part B: Engineering* 31.8 (2000), pp. 763–771. DOI: 10.1016/S1359-8368(00)00046-7.

[63] M. J. N. Jacobs and J. L. J. Van Dingenen. "Ballistic Protection Mechanisms in Personal Armour". In: *Journal of Materials Science* 36.13 (2001), pp. 3137–3142. DOI: 10.1023/A:1017922000090.

[64] Aswani Kumar Bandaru et al. “Ballistic Impact Performance of Kevlar/UHMWPE Hybrid Composite Panels with a Liquid Thermoplastic Resin, Elium”. In: *Materials & Design* 252 (2025), p. 113706. DOI: 10.1016/j.matdes.2025.113706.

[65] T. S. Reddy, P. R. S. Reddy, and V. Madhu. “Dynamic Behaviour of Carbon/Ultra High Molecular Weight Polyethylene (UHMWPE) Hybrid Composite Laminates under Ballistic Impact”. In: *Journal of Dynamic Behavior of Materials* 7 (2021), pp. 403–413. DOI: 10.1007/s40870-020-00275-3.

[66] Xiaogang Chen, Yi Zhou, and Garry Wells. “Numerical and Experimental Investigations into Ballistic Performance of Hybrid Fabric Panels”. In: *Composites Part B: Engineering* 58 (2014), pp. 35–42. DOI: 10.1016/j.compositesb.2013.10.019.

[67] Fritz Klocke et al. “Examples of FEM Application in Manufacturing Technology”. In: *Journal of Materials Processing Technology* 120.1-3 (2002), pp. 450–457. DOI: 10.1016/S0924-0136(01)01210-9.

[68] Martec S.p.A. *Ballistic Protection for Aircraft and Helicopters*. Martec S.p.A. 2024. URL: https://www.martec.it/?page_id=618.

[69] AMEFO. *Ballistic Protection Solutions for Planes and Helicopters*. AMEFO. 2024. URL: https://amefo.fr/en/defense-en/aircrafts-en/.

[70] Muhammad F. Ismail et al. “Low Velocity Impact Behaviour and Post-Impact Characteristics of Kenaf/Glass Hybrid Composites with Various Weight Ratios”. In: *Journal of Materials Research and Technology* 8.3 (2019), pp. 2662–2673. DOI: 10.1016/j.jmrt.2019.04.005.

[71] S. N. A. Safri et al. “Low Velocity and High Velocity Impact Test on Composite Materials: A Review”. In: *The International Journal of Engineering and Science* 3.9 (2014), pp. 50–60. ISSN: 2319-1813. URL: https://www.theijes.com/Vol%2C3%2CIssue%2C9.html.

[72] Shen R. Wu and Lei Gu. *Introduction to the Explicit Finite Element Method for Nonlinear Transient Dynamics*. John Wiley & Sons, 2012. ISBN: 978-0-470-57237-5. DOI: 10.1002/9781118382011.

[73] Renzo Shamey and Xiaoming Zhao. “Solving Dynamic Equations in Dye Transport”. In: *Modelling, Simulation and Control of the Dyeing Process*. Ed. by Renzo Shamey and Xiaoming Zhao. Woodhead Publishing Series in Textiles. Woodhead Publishing, 2014. Chap. 5, pp. 100–113. ISBN: 978-0-85709-133-8. DOI: 10.1533/9780857097583.100. URL: https://www.sciencedirect.com/science/article/pii/B9780857091338500050.

[74] ABAQUS, Inc. *Abaqus User’s Manual*. Version 6.6. ABAQUS, Inc. 2006.

[75] FEA Solutions (UK) Ltd. *Implicit vs Explicit*. FEA Solutions (UK) Ltd. Dec. 11, 2020. URL: https://fea-solutions.co.uk/implicit-vs-explicit/ (visited on 08/26/2026).

[76] ABAQUS, Inc. *Getting Started with Abaqus: Interactive Edition*. Version 6.5. ABAQUS, Inc. 2005.

[77] Federico Paris and Karen E. Jackson. *A Study of Failure Criteria of Fibrous Composite Materials*. Tech. rep. NASA/CR-2001-210661. Hampton, Virginia: NASA Langley Research Center, 2001.

[78] Pedro P. Camanho. *Failure Criteria for Fibre-Reinforced Polymer Composites*. Tech. rep. Porto, Portugal: Departamento de Engenharia Mecânica e Gestão Industrial, Faculdade de Engenharia da Universidade do Porto, 2002.

[79] Zvi Hashin and A. Rotem. "A Fatigue Failure Criterion for Fiber Reinforced Materials". In: *Journal of Composite Materials* 7.4 (1973), pp. 448–464. DOI: 10.1177/002199837300700404.

[80] Zvi Hashin. "Failure Criteria for Unidirectional Fiber Composites". In: *Journal of Applied Mechanics* 47.2 (1980), pp. 329–334. DOI: 10.1115/1.3153664.

[81] I. Lapczyk and J. A. Hurtado. "Progressive Damage Modeling in Fiber-Reinforced Materials". In: *Composites Part A: Applied Science and Manufacturing* 38.11 (2007). CompTest 2006, pp. 2333–2341. ISSN: 1359-835X. DOI: 10.1016/j.compositesa.2007.01.017.

[82] A. Forghani et al. "An Overview of Continuum Damage Models Used to Simulate Intralaminar Failure Mechanisms in Advanced Composite Materials". In: *Numerical Modelling of Failure in Advanced Composite Materials*. Ed. by P. P. Camanho and S. R. Hallett. Woodhead Publishing Series in Composites Science and Engineering. Woodhead Publishing, 2015, pp. 151–173. ISBN: 978-0-08-100332-9. DOI: 10.1016/B978-0-08-100332-9.00006-2.

[83] Ruizhi Wang, Xunjie Yu, and Yanhang Zhang. "Mechanical and structural contributions of elastin and collagen fibers to interlamellar bonding in the arterial wall". In: *Biomechanics and Modeling in Mechanobiology* 20.1 (2021), pp. 93–106. DOI: 10.1007/s10237-020-01370-z. URL: https://doi.org/10.1007/s10237-020-01370-z.

[84] S. L. J. Millen et al. "Coupled Thermal–Mechanical Progressive Damage Model with Strain and Heating Rate Effects for Lightning Strike Damage Assessment". In: *Applied Composite Materials* 26 (2019), pp. 1437–1459. DOI: 10.1007/s10443-019-09789-z.

[85] Gordon R. Johnson and William H. Cook. "A Constitutive Model and Data for Metals Subjected to Large Strains, High Strain Rates and High Temperatures". In: *Proceedings of the 7th International Symposium on Ballistics*. 1983, pp. 541–547.

[86] Gordon R. Johnson and William H. Cook. "Fracture Characteristics of Three Metals Subjected to Various Strains, Strain Rates, Temperatures and Pressures". In: *Engineering Fracture Mechanics* 21.1 (1985), pp. 31–48. DOI: 10.1016/0013-7944(85)90052-9.

[87] Vasu Kumar Reddy Sirigiri et al. "A Review on Johnson–Cook Material Model". In: *Materials Today: Proceedings* 62 (2022), pp. 3450–3456. DOI: 10.1016/j.matpr.2022.04.279.

[88] P. P. Camanho and C. G. Dávila. *Mixed-Mode Decohesion Finite Elements for the Simulation of Delamination in Composite Materials*. Tech. rep. NASA/TM-2002-211737. NASA, 2002.

[89] D. F. Adams, L. A. Carlsson, and R. B. Pipes. *Experimental Characterization of Advanced Composite Materials*. 3rd ed. CRC Press, 2003. ISBN: 9780849315923.

[90] Dassault Systèmes. *Abaqus*. 2024. URL: https://www.3ds.com/products/simulia/abaqus.

[91] Mário Miranda et al. "Crashworthiness assessment of a composite fuselage stanchion employing a strain rate dependent damage model". In: *Composite Structures* 352 (2025), p. 118674. DOI: 10.1016/j.compstruct.2024.118674.

[92] Mário Rui Dias Miranda. "Assessment of composite fuselage crashworthiness: A virtual testing methodology". Supervisor: Volnei Tita. Master's dissertation in Mechanical Engineering – Aeronautical and Vehicle Structures. Faculdade de Engenharia da Universidade do Porto, 2023.

[93] André Rocha. "Development of Ballistic Protection for Military Aircraft: An investigation on material models with strain rate effects". Supervisor: Volnei Tita. Master's dissertation in Mechanical Engineering – Aeronautical and Vehicle Structures. Faculdade de Engenharia da Universidade do Porto, 2024.

[94] Catarina Gonçalves Rodrigues da Silva. "Design and analysis of hybrid composite shields for military aircraft". Supervisor: Volnei Tita. Master's dissertation in Mechanical Engineering – Aeronautical and Vehicle Structures. Faculdade de Engenharia da Universidade do Porto, 2025.

[95] G. Guo, S. Alam, and L. D. Peel. "Numerical analysis of ballistic impact performance of two ceramic-based armor structures". In: *Composites Part C: Open Access* 3 (2020), p. 100061. ISSN: 2666-6820. DOI: 10.1016/j.jcomc.2020.100061. URL: https://www.sciencedirect.com/science/article/pii/S266668202030061X.

[96] A. Ramadhan et al. "High velocity impact response of Kevlar-29/epoxy and 6061-T6 aluminum laminated panels". In: *Materials & Design* 43 (2013), pp. 307–321. ISSN: 0261-3069. DOI: 10.1016/j.matdes.2012.06.034. URL: https://www.sciencedirect.com/science/article/pii/S0261306912004074.

[97] L. Peng et al. "Numerical modelling of the ballistic impact response of hybrid composite structures". In: *Composites Part C: Open Access* 14 (2024), p. 100474. ISSN: 2666-6820. DOI: 10.1016/j.jcomc.2024.100474. URL: https://www.sciencedirect.com/science/article/pii/S2666682024000446.

[98] S. Xin and H. Wen. "A progressive damage model for fiber reinforced plastic composites subjected to impact loading". In: *International Journal of Impact Engineering* 75 (2015), pp. 40–52. ISSN: 0734-743X. DOI: 10.1016/j.ijimpeng.2014.07.014. URL: https://www.sciencedirect.com/science/article/pii/S0734743X14001742.

[99] Ming-ming Xu et al. "An Experimental Investigation into the High Velocity Penetration Resistance of CFRP and CFRP/Aluminium Laminates". In: *Composite Structures* 188 (2018), pp. 450–460. DOI: 10.1016/j.compstruct.2018.01.020.

[100] Qian Zhu et al. "Finite Element Simulation of Damage in Fiber Metal Laminates under High Velocity Impact by Projectiles with Different Shapes". In: *Composite Structures* 214 (2019), pp. 73–82. DOI: 10.1016/j.compstruct.2019.02.009.

[101] G. Kay. *Failure Modeling of Titanium 6Al-4V and Aluminum 2024-T3 with the Johnson-Cook Material Model*. Tech. rep. DOT/FAA/AR-03/57. U.S. Department of Transportation, Federal Aviation Administration, 2003.

[102] Brian G. Falzon et al. "An Investigation of Mode I and Mode II Fracture Toughness Enhancement Using Aligned Carbon Nanotube Forests at the Crack Interface". In: *Composite Structures* 106 (2013), pp. 65–73. DOI: 10.1016/j.compstruct.2013.05.051.

[103] P. J. de Groot, P. A. M. Wijnen, and R. B. F. Janssen. "Real-Time Frequency Determination of Acoustic Emission for Different Fracture Mechanisms in Carbon/Epoxy Composites". In: *Composites Science and Technology* 55.4 (1995), pp. 405–412. DOI: 10.1016/0266-3538(95)00121-2.

[104] Dassault Systèmes. *Output of the energy balance*. Abaqus Documentation. 2025. URL: https://docs.software.vt.edu/abaqusv2025/English/SIMACAEGSARefMap/simagsa-c-ovwoutput.htm (visited on 09/07/2026).

[105] Dassault Systèmes. *Whole Element Variables*. Abaqus Documentation. 2025. URL: https://docs.software.vt.edu/abaqusv2025/English/SIMACAEOUTRefMap/simaout-c-exp-wholeelementvariables.htm (visited on 09/10/2026).

[106] Dassault Systèmes. *Bulk viscosity*. Abaqus Documentation. 2025. URL: https://docs.software.vt.edu/abaqusv2025/English/SIMACAEGSARefMap/simagsa-c-ovwbulkvisc.htm (visited on 09/10/2026).

[107] N. S. Brar, V. S. Joshi, and B. W. Harris. "Constitutive Model Constants for Al7075-T651 and Al7075-T6". In: *Shock Compression of Condensed Matter – 2009*. Vol. 1195. AIP Conference Proceedings. American Institute of Physics, 2009, pp. 945–948. DOI: 10.1063/1.3295300.

[108] Yuanpeng Liu et al. "Process Analysis and Multi-Parameter Optimization of 5052 Aluminum Alloy FSW Based on Thermo-Mechanical Coupling and Taguchi Method". In: *Scientific Reports* 15 (2025), p. 335. DOI: 10.1038/s41598-024-82923-5.

[109] Xuanming Cai et al. "Damage Modes and Response Mechanisms of AlSi10Mg Porous Structures under Different Loading Strain Rates". In: *Acta Metallurgica Sinica* 60.7 (2024), pp. 857–868. DOI: 10.11900/0412.1961.2023.00440.

[110] Sachin Gupta, Sandeep Abotula, and Arun Shukla. "Determination of Johnson–Cook Parameters for Cast Aluminum Alloys". In: *Journal of Engineering Materials and Technology* 136.3 (2014), p. 034502. DOI: 10.1115/1.4027793.

[111] Michael A. Conteh and Emmanuel C. Nsofor. "Composite Flywheel Material Design for High-Speed Energy Storage". In: *Journal of Applied Research and Technology* 14.3 (2016), pp. 184–190. DOI: 10.1016/j.jart.2016.04.005.

[112] P. P. Camanho, C. G. Dávila, and M. F. de Moura. "Numerical Simulation of Mixed-Mode Progressive Delamination in Composite Materials". In: *Journal of Composite Materials* 37.16 (2003), pp. 1415–1438. DOI: 10.1177/0021998303034505.

[113] Mohammad Naderi and Mohammad M. Khonsari. "Stochastic analysis of inter- and intralaminar damage in notched PEEK laminates". In: *Express Polymer Letters* 7.7 (2013), pp. 584–598. DOI: 10.3144/expresspolymlett.2013.56.

[114] R. Farajyar, S. M. Marashi, and M. R. Ayatollahi. "Finite Element Analysis of Ballistic Impact on Kevlar-29/Epoxy Composites with Varying Layer Configurations". In: *International Journal of Impact Engineering* 210 (2026), p. 105572. DOI: 10.1016/j.ijimpeng.2025.105572.

[115] A. S. Al-Azzawi et al. "Impact characteristics of S2-glass fibre/FM94-epoxy composites under high and cryogenic temperatures: Experimental and numerical investigation". In: *Composites Part B: Engineering* 286 (2024), p. 111773. DOI: 10.1016/j.compositesb.2024.111773.

[116] J. Tai et al. "Study on ballistic penetration behavior of unidirectional UHMWPE/carbon fiber composites: Experiments and numerical modeling". In: *Polymer Composites* 46.18 (2024), pp. 16722–16734. DOI: 10.1002/pc.29433.

[117] B. A. Gama and J. W. Gillespie. "Finite Element Modeling of Impact, Damage Evolution and Penetration of Thick-Section Composites". In: *International Journal of Impact Engineering* 38.4 (2011), pp. 181–197. DOI: 10.1016/j.ijimpeng.2010.11.001.

[118] Rui Yuan et al. “Dynamic Response of Armor-Piercing Bullets to Blunt and Penetration with Protective Gelatin Coating”. In: *Defence Technology* (2024). URL: https://www.sciencedirect.com/science/article/pii/S209503492400059X.

[119] Yuequan Wang et al. “Experimental and Numerical Study on the Compressive Failure of Composite Laminates with Fiber Waviness Defects”. In: *Polymers* 13.19 (2021), p. 3204. DOI: 10.3390/polym13193204.

[120] Pawan Sharma, H. S. Mali, and Anurag Dixit. “Mode-II Interlaminar Fracture Toughness Characterization of Woven Carbon–Kevlar Fiber-Reinforced Interyarn Hybrid Textile Composites”. In: *Iranian Polymer Journal* 34 (2025), pp. 1119–1133. DOI: 10.1007/s13726-025-01485-z.

[121] Mingjie Wang et al. “Characterization on Mode-I/II Interlaminar Strength and Fracture Toughness of Co-Cured Fiber-Metal Laminates Based on Carbon-, Glass-, and Aramid-Fiber-Reinforced Epoxy”. In: *Polymers* 17.21 (2025), p. 2937. DOI: 10.3390/polym17212937.

[122] M. Hojo et al. “Modes I and II Interlaminar Fracture Toughness and Fatigue Delamination of CF/Epoxy Laminates with Self-Same Epoxy Interleaf”. In: *International Journal of Fatigue* 28.10 (2006), pp. 1154–1165. DOI: 10.1016/j.ijfatigue.2006.02.004.

[123] E. V. González et al. “Effects of Ply Clustering in Laminated Composite Plates under Low-Velocity Impact Loading”. In: *Composites Science and Technology* 71.6 (2011), pp. 805–817. DOI: 10.1016/j.compscitech.2010.12.018.

Appendix A

VUMAT Subroutine

The following VUMAT subroutine, developed by Mário Miranda, was used to implement a user-defined material model for simulating the ballistic behaviour of hybrid laminates in *Abaqus/Explicit*. The full Fortran source code is presented below.

```
      subroutine vumat(
C Read only (unmodifiable)variables -
     1  nblock, ndir, nshr, nstatev, nfieldv, nprops, lanneal,
     2  stepTime, totalTime, dt, cmname, coordMp, charLength,
     3  props, density, strainInc, relSpinInc,
     4  tempOld, stretchOld, defgradOld, fieldOld,
     5  stressOld, stateOld, enerInternOld, enerInelasOld,
     6  tempNew, stretchNew, defgradNew, fieldNew,
C Write only (modifiable) variables -
     7  stressNew, stateNew, enerInternNew, enerInelasNew )
C
    include 'vaba_param.inc'
************************************************************************
**        3D Orthotropic material with Hashin 3D failure criterion           **
**                                                                           **
**            Mario Miranda, University Charles III Madrid                   **
**                                                                           **
**Adapted from the Dr.-Ing. Ronald Wagner HashinVumat.for open access script **
************************************************************************
C
C State variables stored as
C   state(*,1) = material point status
C     state(*,2:7) = damping stresses
C User defined material properties
C props(1) Young's Modulus E1
C props(2) Young's Modulus E2
C props(3) Poisson's ratio nu12
C props(4) Poisson's ratio nu23
C props(5) Shear modulus G12
C props(6) Shear modulus G23
C props(7) Fibre tensile stress Xt
C props(8) Fibre compressesive stress Xc
C props(9) Tranverse tensile stress mt
C propos(10) Tranverse compressive stress
C props(11) Matrix shear stress 12 S12
C props(12) Matrix shear sress 23 S23
```

```
C props(13) Fracture toughness E fibre tension Gft
C props(14) Fracture toughness E fibre compression Gfc
C props(15) Fracture toughness E matrix tension Gmt
C props(16) Fracture toughness E matrix compression Gmc

C
      dimension props(nprops), density(nblock), coordMp(nblock,*),
     1  charLength(nblock), strainInc(nblock,ndir+nshr),
     2  relSpinInc(nblock,nshr), tempOld(nblock),
     3  stretchOld(nblock,ndir+nshr),
     4  defgradOld(nblock,ndir+nshr+nshr),
     5  fieldOld(nblock,nfieldv), stressOld(nblock,ndir+nshr),
     6  stateOld(nblock,nstatev), enerInternOld(nblock),
     7  enerInelasOld(nblock), tempNew(nblock),
     8  stretchNew(nblock,ndir+nshr),
     8  defgradNew(nblock,ndir+nshr+nshr),
     9  fieldNew(nblock,nfieldv),
     1  stressNew(nblock,ndir+nshr), stateNew(nblock,nstatev),
     2  enerInternNew(nblock), enerInelasNew(nblock)
C
      character*80 cmname
*
    parameter (zero = 0.d0, one = 1.d0, two= 2.d0, half=.5d0)

    parameter(
     *     i_svd_dmgfT   = 1,
     *     i_svd_dmgfC   = 2,
     *     i_svd_dmgmT  = 3,
     *     i_svd_dmgmC  = 4,
     *     i_svd_Stress = 5,
c     *    i_svd_StressXx = 5,
c     *    i_svd_StressYy = 6,
c     *    i_svd_StressZz = 7,
c     *    i_svd_StressXy = 8,
c     *    i_svd_StressYz = 9,
c     *    i_svd_StressZx = 10,
     *     i_svd_Strain   = 11,
c     *    i_svd_StrainXx = 11,
c     *    i_svd_StrainYy = 12,
c     *    i_svd_StrainZz = 13,
c     *    i_svd_StrainXy = 14,
c     *    i_svd_StrainYz = 15,
c     *    i_svd_StrainZx = 16,
     &     i_svd_deq0     = 17,
     &     i_svd_dfeq     = 18,
     &     i_svd_deqm0    = 19,
     &     i_svd_dfeqm    = 20,
     &     i_svd_ftrigger = 21,
     &     i_svd_ttrigger = 22,
     &     i_svd_beta2    = 23,
     &     i_svd_beta3    = 24,
     &     i_svd_status_el   = 25,
     *     n_svd_required = 25)


* Read material properties
*
```

```
94        E1 = props(1)
95       E2 = props(2)
96       E3 = E2
97       xnu12 = props(3)
98       xnu13 = xnu12
99       xnu23 = props(4)
100      G12 = props(5)
101      G13 = G12
102      G23 = props(6)
103      xnu21 = xnu12 * E2 / E1
104      xnu31 = xnu13 * E3 / E1
105      xnu32 = xnu23 * E3 / E2
106
107   * Coupon test values
108      ft = props(7)
109      fc = props(8)
110      tt = props(9)
111      tc = props(10)
112        f12 = props(11)
113      f23 = props(12)
114   * Fracture toughness values
115      Gft = props(13)
116      Gfc = props(14)
117      Gmt = props(15)
118      Gmc = props(16)
119
120   * Elastic step at the beginning of the analysis
121          a= zero
122           if (totalTime .eq. zero) then
123             if (nstatev .lt. n_svd_required) then
124              call xplb_abqerr(-2,'Subroutine VUMAT requires the ' //
125       &           'specification of %I state variables. Check the '  //
126       &          'definition of *DEPVAR in the input file.',
127       &           n_svd_required,zero,' ')
128                call xplb_exit
129             end if
130             call Ortelas (nblock,
131       &          stateOld(1,i_svd_dmgfT),
132       &          stateOld(1,i_svd_dmgfC),
133       &          stateOld(1,i_svd_dmgmT),
134       &          stateOld(1,i_svd_dmgmC),
135       &          E1,E2,E3,xnu12,
136       &          xnu21, xnu13, xnu31,xnu23,xnu32,
137       &          G12, G23, G13,stateOld(1,i_svd_Strain), strainInc,dt,
138       &          stressNew,stateOld(1,i_svd_ttrigger),
139       &          stateNew(1,i_svd_beta2),
140       &          stateNew(1,i_svd_beta3),stateOld(1,i_svd_beta2),
141       &          stateOld(1,i_svd_beta3))
142           return
143        end if
144
145   * Update strain
146             call strainUpdate (nblock, strainInc,
147       &     stateOld(1,i_svd_Strain), stateNew(1,i_svd_Strain))
148
149   * Stress Update
150             call Ortelas (nblock,
```

```
151       &         stateOld(1,i_svd_dmgfT),
152       &         stateOld(1,i_svd_dmgfC),
153       &         stateOld(1,i_svd_dmgmT),
154       &         stateOld(1,i_svd_dmgmC),
155       &         E1,E2,E3,xnu12,
156       &         xnu21, xnu13, xnu31,xnu23,xnu32,
157       &         G12, G23, G13,stateOld(1,i_svd_Strain),
158       &         stateNew(1,i_svd_Strain),dt, stressNew,
159       &         stateOld(1,i_svd_ttrigger),stateNew(1,i_svd_beta2),
160       &         stateNew(1,i_svd_beta3),stateOld(1,i_svd_beta2),
161       &         stateOld(1,i_svd_beta3))
162
163
164   * Failure evaluation
165         call copyr ( nblock,
166        *     stateOld(1,i_svd_dmgfT),stateNew(1,i_svd_dmgfT))
167         call copyr ( nblock,
168        *     stateOld(1,i_svd_dmgfC),stateNew(1,i_svd_dmgfC))
169         call copyr ( nblock,
170        *     stateOld(1,i_svd_dmgmT),stateNew(1,i_svd_dmgmT))
171         call copyr ( nblock,
172        *     stateOld(1,i_svd_dmgmC),stateNew(1,i_svd_dmgmC))
173         call copyr ( nblock,
174        *     stateOld(1,i_svd_deq0),stateNew(1,i_svd_deq0))
175         call copyr ( nblock,
176        *     stateOld(1,i_svd_dfeq),stateNew(1,i_svd_dfeq))
177         call copyr ( nblock,
178        *     stateOld(1,i_svd_deqm0),stateNew(1,i_svd_deqm0))
179         call copyr ( nblock,
180        *     stateOld(1,i_svd_dfeqm),stateNew(1,i_svd_dfeqm))
181         call copyr ( nblock,
182        *     stateOld(1,i_svd_ftrigger),stateNew(1,i_svd_ftrigger))
183         call copyr ( nblock,
184        *     stateOld(1,i_svd_ttrigger),stateNew(1,i_svd_ttrigger))
185
186         nDmg = zero
187        a=zero
188   c      OPEN (unit=1,file='C:\Users\mario\Desktop\Tese\ABAQUS_FILES\H.txt'
189   c     & ,STATUS='UNKNOWN',ACCESS='APPEND')
190   c      WRITE (1,'(F12.6,2X,F12.6,2X,F12.6,2X,F12.6,2X,F12.6)')
191   c       * ft
192   c      CLOSE(1)
193         call hashin3d  (nblock, nDmg,
194        *     ft, fc, f12, f23, tt, tc,
195        *     stateNew(1,i_svd_dmgfT),
196        *     stateNew(1,i_svd_dmgfC),
197        *     stateNew(1,i_svd_dmgmT),
198        *     stateNew(1,i_svd_dmgmC),Gft,Gfc,Gmt,Gmc,
199        *     stressNew,stateOld(1,i_svd_Strain),stateNew(1,i_svd_Strain),
200        *     dt,charLength,
201        *     stateNew(1,i_svd_deq0),stateNew(1,i_svd_dfeq),
202        *     stateNew(1,i_svd_deqm0),stateNew(1,i_svd_dfeqm),
203        *     stateNew(1,i_svd_ftrigger),stateNew(1,i_svd_ttrigger),
       stateNew(1,i_svd_status_el))
204   *     -- Recompute stresses if new Damage is occurring
205         if ( nDmg .gt. zero ) then
206            a=one
```

```
207            call Ortelas ( nblock,
208      &          stateOld(1,i_svd_dmgfT),
209      &          stateOld(1,i_svd_dmgfC),
210      &          stateOld(1,i_svd_dmgmT),
211      &          stateOld(1,i_svd_dmgmC),
212      &          E1,E2,E3,xnu12,
213      &          xnu21, xnu13, xnu31,xnu23,xnu32,
214      &          G12, G23, G13,stateOld(1,i_svd_Strain),
215      &          stateNew(1,i_svd_Strain),dt, stressNew,
216      &          stateNew(1,i_svd_ttrigger),stateNew(1,i_svd_beta2),
217      &          stateNew(1,i_svd_beta3),stateOld(1,i_svd_beta2),
218      &          stateOld(1,i_svd_beta3))
219
220         end if
221
222
223
224  * Integrate the internal specific energy (per unit mass)
225  *
226       call EnergyInternal3d ( nblock, stressOld, stressNew,
227      *   strainInc, density, enerInternOld, enerInternNew )
228  *
229       return
230      end
231
232  **********************************
233  * Ortelas: Orthotropic elasticity   *
234  **********************************
235      subroutine Ortelas(nblock, dmgfT, dmgfC, dmgmT, dmgmC, E1,E2,E3,xnu12,
236       & xnu21, xnu13, xnu31,xnu23,xnu32,
237       &  G12, G23, G13,strainold, strain,dt, stress,ttrigger,beta2,beta3,
238       & beta2old,beta3old)
239
240           include 'vaba_param.inc'
241
242       parameter( zero = 0.d0, one = 1.d0, two = 2.d0, dec=.1d0,
243       & hundred=100.d0, fac=1.29d0)
244
245       dimension strain(nblock,6), dmgfT(nblock), dmgfC(nblock),
246       &  dmgmT(nblock), dmgmC(nblock), stress(nblock,6),
247       &  strainold(nblock,6),beta2(nblock), beta3(nblock),
248       &  beta2old(nblock), beta3old(nblock),ttrigger(nblock)
249
250         parameter ( smt = 0.3d0, smc = 0.3d0 )
251        do k = 1, nblock
252  *        Damage variables
253         dft = dmgfT(k)
254         dfc = dmgfC(k)
255         dmt = dmgmT(k)
256         dmc = dmgmC(k)
257           df = ( one - dft ) * ( one - dfc )
258           dm = (one - smt*dmt) * (one - smc*dmc)
259           gg=one-df*dm*xnu12*xnu21-dm*xnu23*xnu32-df*xnu31*xnu13-
260       &   two*df*dm*xnu21*xnu32*xnu13
261           gginv= one / gg
262
263  *     Strain rate effect
```

```
264           beta2(k)=one
265           beta3(k)=one
266           if (ttrigger(k) .lt. one) then
267             if (dt .gt. zero) then
268              srate2= abs(strain (k,2)-strainold (k,2))/dt
269              srate3= abs(strain (k,3)-strainold (k,3))/dt
270
271               if ( srate2 .gt. dec) then
272               beta2(k)=(srate2-dec)*(fac-one)/(hundred-dec)+one
273               end if
274               if ( srate2 .ge. hundred) then
275               beta2(k)=fac
276              end if
277
278              if ( srate3 .gt. dec) then
279              beta3(k)=(srate3-dec)*(fac-one)/(hundred-dec)+one
280               end if
281               if ( srate3 .ge. hundred) then
282               beta3(k)=fac
283               end if
284             end if
285
286             else if (ttrigger(k) .ge. one) then
287                 beta2(k) =beta2old(k)
288                 beta3(k)=beta3old(k)
289         end if
290   c      OPEN (unit=1,file='C:\Users\mario\Desktop\Tese\ABAQUS_FILES\H.txt'
291   c     & ,STATUS='UNKNOWN',ACCESS='APPEND')
292   c      WRITE (1,'(F12.6,2X,F12.6,2X,F12.6,2X,F12.6,2X,F12.6)')
293   c     * beta2,srate2, beta3,srate3
294   c      CLOSE(1)
295   * Damaged stiffness matrix
296           dC11 = gginv*df*E1*(one-dm*xnu23*xnu32)
297           dC22 = gginv*dm*beta2(k)*E2*(one-df*xnu13*xnu31)
298           dC33 = gginv*beta2(k)*E3*(one-df*dm*xnu12*xnu21)
299           dC12 = gginv*df*dm*E1*(xnu21+xnu23*xnu31)
300           dC23 = gginv*dm*beta2(k)*E2*(xnu32+df*xnu12*xnu31)
301           dC13 = gginv*df*E1*(xnu31+dm*xnu21*xnu32)
302           dG12 = df*dm*G12
303           dG23 = df*dm*G23
304           dG13 = df*dm*G13
305   c      OPEN (unit=1,file='C:\Users\mario\Desktop\Tese\ABAQUS_FILES\H.txt'
306   c     & ,STATUS='UNKNOWN',ACCESS='APPEND')
307   c      WRITE (1,'(F12.1,2X,F12.6,2X,F12.6,2X,F12.6,2X,F12.6)')
308   c     * dC11,df,dC22,dm,dC33
309   c      CLOSE(1)
310   *       Updated stress calculation
311           stress(k,1) = dC11 * strain(k,1) + dC12 * strain (k,2) +
312        &      dC13 * strain(k,3)
313
314           stress(k,2) = dC12 * strain(k,1) + dC22 * strain(k,2) +
315        &       dC23 * strain(k,3)
316
317           stress(k,3) = dC13 * strain(k,1) + dC23 * strain(k,2) +
318        &  dC33 * strain(k,3)
319
320           stress(k,4) = two* dG12 * strain(k,4)
```

```
321
322         stress(k,5) =two* dG23 * strain(k,5)
323
324         stress(k,6) =two* dG13 * strain(k,6)
325   c      OPEN (unit=1,file='C:\Users\mario\Desktop\Tese\ABAQUS_FILES\H.txt'
326   c     & ,STATUS='UNKNOWN',ACCESS='APPEND')
327   c      WRITE (1,'(F12.6,2X,F12.5,2X,F12.5,2X,F12.6,2X,F12.6,2X,F12.6)')
328   c     * beta2, beta3
329   c      CLOSE(1)
330
331         end do
332
333   *
334       return
335
336
337       end
338
339   ******************************
340   * strainUpdate: Update strain *
341   ******************************
342         subroutine strainUpdate (nblock, strainInc, strainOld, strainNew)
343   *
344           include 'vaba_param.inc'
345   *
346           dimension strainInc(nblock,6), strainOld(nblock,6),
347        &  strainNew(nblock,6)
348   *
349           do k = 1, nblock
350            strainNew(k,1)= strainOld(k,1)
351        &                      + strainInc(k,1)
352              strainNew(k,2)= strainOld(k,2)
353        &                      + strainInc(k,2)
354              strainNew(k,3)= strainOld(k,3)
355        &                      + strainInc(k,3)
356              strainNew(k,4)= strainOld(k,4)
357        &                     + strainInc(k,4)
358              strainNew(k,5)= strainOld(k,5)
359        &                      + strainInc(k,5)
360              strainNew(k,6)= strainOld(k,6)
361        &                      + strainInc(k,6)
362
363           end do
364   *
365           return
366       end
367
368
369
370   *************************************
371   * hashin3d: Hashin 3D failure criteria*
372   *************************************
373       subroutine hashin3d (nblock, nDmg,
374        &  ft, fc, f12, f23, tt, tc,
375        &  dmgfT, dmgfC, dmgmT, dmgmC,Gft,Gfc,Gmt,Gmc, stress, strainold,
376        &  strain,dt,charLength,deq0,dfeq,deqm0,dfeqm,ftrigger,ttrigger,status_el)
377
```

```
      include 'vaba_param.inc'

     parameter( zero = 0.d0, one = 1.d0, two = 2.d0,half=.5d0)

     dimension dmgfT(nblock), dmgfC(nblock), dmgmT(nblock), dmgmC(nblock),
     &     dmgfTold(nblock), dmgfCold(nblock),
     &     dmgmTold(nblock), dmgmCold(nblock),
     &   stress(nblock,6), strain(nblock,6), charLength(nblock),
     &     ftrigger(nblock), ttrigger(nblock), strainold(nblock,6),
     & status_el(nblock)

     do k = 1, nblock

         e11=strain(k,1)
         e22=strain(k,2)
         e33=strain(k,3)
         e12=strain(k,4)
         e23=strain(k,5)
         e13=strain(k,6)

         s11= stress(k,1)
         s22= stress(k,2)
         s33= stress(k,3)
         s12= stress(k,4)
         s23= stress(k,5)
           s13= stress(k,6)
*  Effect of strain rate
           sratef=abs((strain (k,1)-strainold (k,1))/dt)
           sratem2=abs((strain (k,2)-strainold (k,2))/dt)
           sratem3=abs((strain (k,3)-strainold (k,3))/dt)

           srf=(sratef-.1d0)/(100.d0-.1d0)
           srmax=MAX(sratem2,sratem3)
           srm=(srmax-.1d0)/(100.d0-.1d0)
* Fibre direction strain rate
           fti=ft
           fci=fc
           if ( sratef .gt. .1d0) then
             fti=(srf*.38d0+one)*ft
             fci=(srf*.39d0+one)*fc
             end if
         if ( sratef .ge. 100d0) then
             fti=1.38d0*ft
             fci=1.39d0*fc
         end if
* Matrix direction strain rate
         tti=tt
         tci=tc
         Gmti=Gmt
         Gmci=Gmc
          if ( srmax .gt. .1d0) then
             tti=(srm*.38d0+one)*tt
             tci=(srm*.37d0+one)*tc
             Gmti=(srm*.42d0+one)*Gmt
             Gmci=(srm*.63d0+one)*Gmc
          end if
           if (srmax .ge. 100d0) then
```

```
435               tti=1.38d0*tt
436               tci=1.37d0*tc
437               Gmti=1.42d0*Gmt
438               Gmci=1.63d0*Gmc
439            end if
440
441   * Turn inv values into double precision
442              ftinv=one/fti
443              fcinv=one/fci
444              ttinv=one/tti
445              tcinv=one/tci
446              f12inv=one/f12
447            f23inv= one/f23
448   * Store previous iteration damage values
449              dmgfTold(k)=dmgfT(k)
450            dmgfCold(k)=dmgfC(k)
451              dmgmTold(k)=dmgmT(k)
452              dmgmCold(k)=dmgmC(k)
453   * Fibre modes
454          if ( s11 .gt. zero) then
455   *          Fibre tension
456            ftf = (s11*ftinv)**2 +(s12*f12inv)**2 +(s13*f12inv)**2
457           if (ftrigger(k) .le. zero) then
458              if (ftf .ge. one) then
459                  ftrigger(k) = one
460                  dmg = 1
461   C  Macauley operator
462                  if (e11 .lt. zero) then
463                           e11=zero
464                  end if
465                  if (s11 .lt. zero) then
466                         s11=zero
467                  end if
468   C Equivalent measures
469                deq=charLength(k)*sqrt(e11**2+e12**2+e13**2)
470                  deqinv=one/deq
471                seq=charLength(k)*(s11*e11+s12*e12+s13*e13)*deqinv
472                seq0=seq/sqrt(ftf)
473                deq0=deq/sqrt(ftf)
474                seq0inv=one/seq0
475                dfeq=two*Gft*seq0inv
476                dmgfT(k)=(dfeq * (deq-deq0))/(deq * (dfeq-deq0))
477   c      OPEN (unit=1,file='C:\Users\mario\Desktop\Tese\ABAQUS_FILES\H.txt'
478   c     & ,STATUS='UNKNOWN',ACCESS='APPEND')
479   c     WRITE (1,'(F12.6,2X,F12.6,2X,F12.6,2X,F12.6,2X,F12.6)')
480   c     * s12,f12inv
481   c      CLOSE(1)
482               end if
483            else if (ftrigger(k) .ge. one) then
484                 if (e11 .lt. zero) then
485                           e11=zero
486                  end if
487                  if (s11 .lt. zero) then
488                         s11=zero
489                      end if
490                  dmg = 1
491                deq=charLength(k)*sqrt(e11**2+e12**2+e13**2)
```

```
492               dmgfT(k)=(dfeq * (deq-deq0))/(deq * (dfeq-deq0))
493
494             dmgfT(K) = MIN(dmgfT(K),one)
495             dmgfT(K) = MAX(dmgfT(K),zero)
496             dmgfT(K) = MAX(dmgfT(K),dmgfTold(K))
497 c       OPEN (unit=1,file='C:\Users\mario\Desktop\Tese\ABAQUS_FILES\H.txt'
498 c      & ,STATUS='UNKNOWN',ACCESS='APPEND')
499 c       WRITE (1,'(F12.6,2X,F12.6,2X,F12.6,2X,F12.6,2X,F12.6)')
500 c      * ft,dmgfT(k)
501 c       CLOSE(1)
502               end if
503
504            else if (s11 .lt. zero) then
505 *                Fibre compression
506
507                fcf= abs(s11)*fcinv
508              if (ftrigger(k) .le. zero) then
509                if (fcf .ge. one) then
510                    ftrigger(k) = one
511                  dmg = 1
512                      if (-e11 .lt. zero) then
513                          e11=zero
514                     end if
515                       if (-s11 .lt. zero) then
516                         s11=zero
517                      end if
518                  deq=charLength(k)*abs(e11)
519                  deqinv= one/deq
520
521                 seq=charLength(k)*s11*e11*deqinv
522               seq0=seq/sqrt(fcf)
523               deq0=deq/sqrt(fcf)
524               seq0inv=one/seq0
525               dfeq=two*Gfc*seq0inv
526               dmgfC(k)=(dfeq * (deq-deq0))/(deq * (dfeq-deq0))
527                   end if
528              else if (ftrigger(k) .ge. one) then
529                  if (-e11 .lt. zero) then
530                          e11=zero
531                 end if
532                 if (-s11 .lt. zero) then
533                        s11=zero
534                    end if
535                   dmg = 1
536                  deq=charLength(k)*abs(e11)
537                dmgfC(k)=(dfeq * (deq-deq0))/(deq * (dfeq-deq0))
538              dmgfC(K) = MIN(dmgfC(K),one)
539              dmgfC(K) = MAX(dmgfC(K),zero)
540              dmgfC(K) = MAX(dmgfC(K),dmgfCold(K))
541             end if
542           end if
543
544
545 * Matrix modes
546       if ( (s22+s33) .ge. zero ) then
547 *           Matrix tension
548           ttf=((s22+s33)*ttinv)**2 + (s23**2 - s22*s33)*(f23inv**2)+
```

```
549       &   (s12**2+s13**2)*(f12inv**2)
550          if (ttrigger(k) .le. zero) then
551
552              if (ttf .ge. one) then
553              dmg=1
554                ttrigger(k) = one
555             if (e22 .lt. zero) then
556                           e22=zero
557             end if
558             if (s22 .lt. zero) then
559                         s22=zero
560             end if
561             if (e33 .lt. zero) then
562                           e33=zero
563             end if
564             if (s33 .lt. zero) then
565                         s33=zero
566             end if
567
568              deqm=charLength(k)*sqrt((e22)**2+(e33)**2+e12**2+e23**2+
569       &          e13**2)
570              deqminv=one/deqm
571               seqm=charLength(k)*((s22)*(e22)+(s33)*(e33)+
572       &           s12*e12+s23*e23+s13*e13)*deqminv
573
574               seqm0=seqm/sqrt(ttf)
575               deqm0=deqm/sqrt(ttf)
576                 seqm0inv=one/seqm0
577               dfeqm=two*Gmti*seqm0inv+deqm0
578               dmgmT(k)=dfeqm*(deqm-deqm0)/(deqm*(dfeqm-deqm0))
579 c      OPEN (unit=1,file='C:\Users\mario\Desktop\Tese\ABAQUS_FILES\H.txt'
580 c     & ,STATUS='UNKNOWN',ACCESS='APPEND')
581 c      WRITE (1,'(F12.6,2X,F12.6,2X,F12.6,2X,F12.6,2X,F12.6)')
582 c     * seqm0,deqm0,dfeqm
583 c      CLOSE(1)
584             end if
585          else if (ttrigger(k) .ge. one) then
586                  dmg=1
587               if (e22 .lt. zero) then
588                           e22=zero
589             end if
590             if (s22 .lt. zero) then
591                         s22=zero
592             end if
593             if (e33 .lt. zero) then
594                           e33=zero
595             end if
596             if (s33 .lt. zero) then
597                         s33=zero
598             end if
599              deqm=charLength(k)*sqrt((e22)**2+(e33)**2+e12**2+e23**2+
600       &          e13**2)
601               dmgmT(k)=dfeqm*(deqm-deqm0)/(deqm*(dfeqm-deqm0))
602 c      OPEN (unit=1,file='C:\Users\mario\Desktop\Tese\ABAQUS_FILES\H.txt'
603 c     & ,STATUS='UNKNOWN',ACCESS='APPEND')
604 c      WRITE (1,'(F12.6,2X,F12.6,2X,F12.6,2X,F12.6,2X,F12.6)')
605 c     * seqm0,deqm0,dfeqm
```

```
c      CLOSE(1)
           dmgmT(k) = MIN(dmgmT(k),one)
           dmgmT(k) = MAX(dmgmT(k),zero)
           dmgmT(k) = MAX(dmgmT(k),dmgmTold(k))
       end if

       else if ( (s22+s33) .lt. zero ) then
*          Matrix compression

            tcf = tcinv *(s22+s33)*((tci/(two*f23))**2 - one) +
     &    ((s22+s33)/(two*f23))**2+ (s23**2-s22*s33)*(f23inv**2)+
     &         (s12*f12inv)**2 + (s13*f12inv)**2
          if (ttrigger(K) .le. zero) then
           if (tcf .ge. one) then

            dmg=1
              ttrigger(k) = one
               if (-e22 .lt. zero) then
                        e22=zero
           end if
           if (-s22 .lt. zero) then
                     s22=zero
           end if
           if (-e33 .lt. zero) then
                       e33=zero
           end if
           if (-s33 .lt. zero) then
                     s33=zero
           end if
           deqm=charLength(k)*sqrt((-e22)**2+(-e33)**2+e12**2+e23**2+
     &        e13**2)
              deqminv=one/deqm
             seqm=charLength(k)*((-s22)*(-e22)+(-s33)*(-e33)+
     &           s12*e12+s23*e23+s13*e13)*deqminv
             seqm0=seqm / sqrt(tcf)
             deqm0=deqm / sqrt(tcf)
               seqm0inv=one/seqm0
             dfeqm=two*Gmci*seqm0inv+deqm0
             dmgmC(k)=dfeqm*(deqm-deqm0)/(deqm*(dfeqm-deqm0))

             end if
          else if (ttrigger(k) .ge. one) then
              dmg=1
           if (-e22 .lt. zero) then
                       e22=zero
           end if

           if (-s22 .lt. zero) then
                     s22=zero
           end if
           if (-e33 .lt. zero) then
                       e33=zero
           end if
           if (-s33 .lt. zero) then
                     s33=zero
           end if
              deqm=charLength(k)*sqrt((-e22)**2+(-e33)**2+e12**2+e23**2+
```

```
663       &         e13**2)
664                 dmgmC(k)=dfeqm*(deqm-deqm0)/(deqm*(dfeqm-deqm0))
665               dmgmC(k) = MIN(dmgmC(k),one)
666               dmgmC(k) = MAX(dmgmC(k),zero)
667               dmgmC(k) = MAX(dmgmC(k),dmgmCold(k))
668
669                end if
670             end if
671
672             if ((dmgfT(k) .ge. 0.99) .or. (dmgfC(k) .ge. 0.99)
673       &        .or. (dmgmT(k) .ge. 0.99) .or. (dmgmC(k).ge. 0.99)) then
674               status_el(k) = 0.0
675             else
676               status_el(k) = 1.0
677             end if
678
679                nDmg = nDmg + dmg
680
681       end do
682       return
683       end
684
685 ************************************************************
686 *   CopyR: Copy from one array to another                  *
687 ************************************************************
688       subroutine CopyR(nCopy, from, tom )
689 *
690       include 'vaba_param.inc'
691 *
692       dimension from(nCopy), tom(nCopy)
693 *
694       do k = 1, nCopy
695          tom(k) = from(k)
696       end do
697 *
698       return
699       end
700
701 ************************************************************
702 *   EnergyInternal3d: Compute internal energy for 3d case  *
703 ************************************************************
704
705       subroutine EnergyInternal3d(nblock, sigOld, sigNew ,
706        *   strainInc, curDensity, enerInternOld, enerInternNew)
707 *
708         include 'vaba_param.inc'
709 *
710
711       parameter( two = 2.d0, half = .5d0 )
712 *
713       dimension sigOld (nblock,6), sigNew (nblock,6),
714      *     strainInc (nblock,6), curDensity (nblock),
715      *     enerInternOld(nblock), enerInternNew(nblock)
716 *
717       do k = 1, nblock
718          stressPower  = half * (
719      *        ( sigOld(k,1) + sigNew(k,1) )
```

```
720       *         * ( strainInc(k,1) )
721       *         +       ( sigOld(k,2) + sigNew(k,2) )
722       *         * ( strainInc(k,2))
723       *         +       ( sigOld(k,3) + sigNew(k,3) )
724       *         * ( strainInc(k,3))
725       *         + two*( sigOld(k,4) + sigNew(k,4) )
726       *         * strainInc(k,4)
727       *         + two*( sigOld(k,5) + sigNew(k,5) )
728       *         * strainInc(k,5)
729       *         +  two*( sigOld(k,6) + sigNew(k,6) )
730       *         * strainInc(k,6) )
731   *
732             enerInternNew(k) = enerInternOld(k) + stressPower/curDensity(k)
733         end do
734   *
735         return
736          end
```

The user = flag was used in the Abaqus command line to compile and link this subroutine to the simulation.